

**COMPUTATIONAL MODELING OF CELL
SIGNALING DYNAMICS: HYPOTHESIS
MANAGEMENT AND PARAMETER ESTIMATION
METHODS APPLIED TO THE AKT PATHWAY**

NIM TRI HIEU

(B.Eng., NTU)

**A THESIS SUBMITTED
FOR THE DEGREE OF DOCTOR OF PHILOSOPHY
IN COMPUTATION AND SYSTEMS BIOLOGY
(CSB)**

**SINGAPORE-MIT ALLIANCE
NATIONAL UNIVERSITY OF SINGAPORE**

2012

DECLARATION

I hereby declare that this thesis is my original work and it has been written by me in its entirety. I have duly acknowledged all the sources of information which have been used in the thesis.

This thesis has also not been submitted for any degree in any university previously.

Nim Tri Hieu

Nim Tri Hieu

17 April 2013

ACKNOWLEDGMENTS

I find myself among the most fortunate students of the world to have Dr. Lisa Tucker-Kellogg as a PhD advisor. I am grateful to my co-advisor Prof. Jacob White, whose teaching passion and intellectual capacity define the person I wish to become. I am indebted to my co-advisor Prof. Marie-Véronique Clément for her kind guidance and facilitation throughout my PhD study. I would like to express my deepest appreciation to my collaborator Dr. Felix Margadant for his generosity in time and resource in the microscopy simulation project.

I would also like to thank the wonderful people who have made my work and life so immensely better that I can never express enough gratitude:

Dr. Luo Le, my collaborator from the MVC Lab for generously giving her time, data, and training;

My teachers: Co Nguyen Thi Quy, Thay Le Thanh Xuan, Thay Nguyen Thanh Dung, Prof. Vivekanand Gopalkrishnan, Prof. Kwoh Chee Keong, Prof. Ho Hwee Long, and Ms. Helen Low, for making me a better person in so many different ways;

My lab mates from the Tucker-Kellogg Groups: Shi Yuan, Li Huipeng, Wang Junjie, Neha Bahl, Akila Surendran, Huang Lu, and Lakshmi Venkatraman;

My lab mates from the Mechanobiology Institute, NUS: Xu Xiaochun, Liu Chengcheng, Zhang Wenwei, Liu Sihan, Zhang Bo, and Zhao Chen;

My lab mates from the Computational Biology Laboratory, NUS School of Computing: Ngo Thanh Son, Chiang Tsung-Han, and Wang Yue;

My lab mates from the Computational Prototyping Group, MIT Research Laboratory of Electronics: Bo Kim, Lei Zhang, and Yu-Chung Hsiao;

Nanyang Technological University, my *alma mater*, for giving me the generous financial support for my undergraduate study and oversea exchange programs;

The Singapore-MIT Alliance, the Mechanobiology Institute, and National University of Singapore, for the financial support;

Ms Hong Yanling, Ms Juliana Chai, Ms Carol Cheng, for the patient support in the tedious paperwork involved in my study and research;

My mother Pham Thi Nguyen Luu and my father Nim Phic Chong, for their steadfast love in good or bad times;

My three teenage younger brothers, for unintentionally providing me with endless motivation to work harder;

And my wife Tran Thi Thanh Quy, the most important person in my life.

TABLE OF CONTENTS

DECLARATION	II
ACKNOWLEDGMENTS	III
TABLE OF CONTENTS	V
SUMMARY	IX
LIST OF TABLES AND BOXES	XII
LIST OF FIGURES	XIII
LIST OF ABBREVIATIONS	XV
CHAPTER ONE: INTRODUCTION	1
1.1 SIGNAL TRANSDUCTION NETWORKS	1
1.2 SYSTEMS BIOLOGY	2
1.3 SOME ONGOING CHALLENGES IN SYSTEMS BIOLOGY	3
Constructing predictive kinetic models of signaling pathways	4
Estimating kinetic model parameter based on time-series protein concentrations.....	5
1.4 THESIS RESEARCH OBJECTIVES AND ORGANIZATION	6
Research objectives	6
The CHEGS research approaches.....	7
Thesis organization.....	10
Author contributions.....	10
CHAPTER TWO: MATERIALS AND METHODS	12
2.1 MODELING-DRIVEN PATHWAY ANALYSIS	12
2.2 ODE MODEL	12
2.3 LINEAR SPLINE FOR REVERSE FITTING	13
2.4 MODEL COMPLEXITY REDUCTION	14
2.5 PARAMETER ESTIMATION (NON-SPEDRE)	15
2.6 ANALYSIS OF MODEL FAMILIES/ENSEMBLES	16
2.7 COMPUTATIONAL RESOURCES AND MODELING TOOLS	16

2.7	EXPERIMENTAL METHODS	18
	Cell culture.....	18
	Treatment conditions	19
	Time course measurements assay	19
	Lucigenin assay	19
	Measurement of PIP3 by Immunofluorescence and Confocal Microscopy	20
2.8	DATA NORMALIZATION.....	22

CHAPTER THREE: DATA-RICH PARAMETER ESTIMATION METHOD (SPEDRE)

.....		23
3.1	INTRODUCTION	23
3.2	PRELIMINARIES.....	26
	Ordinary differential equation (ODE) for mass action kinetics (MAK).....	26
	Rate constant estimation objective	27
3.3	ALTERNATIVE OBJECTIVE FUNCTION	28
	Error terms of dual objective function	29
	Product of functions.....	30
3.4	LOOPY BELIEF PROPAGATION (LBP).....	31
	Factor graph	32
	Discretization and Joint Probability Tables.....	33
	Loopy Belief Propagation.....	34
	Asymptotic Analysis of the Modified LBP (SPEDRE-base) Algorithm.....	36
3.5	WEB SERVER IMPLEMENTATION	38
	Input.....	38
	Processing method	40
	Ouput	42
3.6	BENCHMARK EXPERIMENT SETUP	45
3.7	RESULTS	46
	Scalability with artificial networks	47
	Web service performance	55

3.8	DISCUSSION	56
	Contribution.....	56
	Data mountain: challenges and opportunities.....	58
CHAPTER FOUR: REDOX-REGULATED AKT ACTIVATION – BIOLOGICAL		
TEST CASE FOR SPEDRE AND OPPORTUNITY FOR MODELING..... 60		
4.1	ODE MODELING OF CELL SIGNALING PATHWAYS	61
	Model construction	62
	Model calibration (parameter estimation)	63
	Model simulation.....	64
	Model analysis	64
4.2	AKT ACTIVATION PATHWAY	66
4.3	MOTIVATIONS FOR MODELING DYNAMICS OF AKT PHOSPHORYLATION UPON ACTIVATION BY GROWTH FACTORS.....	67
4.4	REDOX REGULATION OF AKT ACTIVATION PATHWAY	68
4.5	REGULATION OF INTRACELLULAR SUPEROXIDE.....	69
4.6	MODELING REDOX-REGULATED AKT ACTIVATION	71
4.7	PERFORMANCE OF SPEDRE IN COMPARISON WITH OTHER STANDALONE AND HYBRID METHODS ON THE AKT MODEL.....	74
4.8	PUZZLING REDOX REGULATION PHENOMENON IN SERUM-INDUCED AKT ACTIVATION ..	77
4.9	CONCLUSION	77
CHAPTER FIVE: NON-CANONICAL ACTIVATION OF AKT IN SERUM-		
STIMULATED FIBROBLASTS, REVEALED BY COMPARATIVE MODELING OF		
PATHWAY MECHANISMS 79		
5.1	INTRODUCTION	79
5.2	CANONICAL PIP3/AKT CASCADE.....	83
	The delay between peak PIP3 activation and peak Akt phosphorylation.....	83
	The null hypothesis model.....	84
	Rejection of the null hypothesis	87
5.3	NON-CANONICAL MECHANISMS FOR AKT ACTIVATION	88

Non-canonical causes of altered Akt localization	88
Non-canonical causes of altered Akt phosphorylation dynamics.....	89
Systematic generation of alternative scenarios.....	90
5.4 MEMBRANE FRACTIONATION DYNAMICS.....	94
Model predicts non-trivial dynamics of membrane fractions.....	94
Membrane fractions time-series	95
5.5 MODEL ANALYSIS WITH ADDITIONAL MEMBRANE FRACTION TIME-SERIES	96
Model re-calibration using additional membrane fraction time-series.....	96
Model prediction of PIP3 inhibition experiments	101
5.6 MODEL ENSEMBLE ANALYSIS	103
5.7 ROBUSTNESS ANALYSIS OF PIP3-DEPENDENT RECRUITMENT MODEL.....	106
5.8 DISCUSSION	108
Scope of study: PIP3-Aktp ³⁰⁸	108
Timeline of hypothesis exclusions.....	110
Biology contributions	110
Modeling-driven methods contribution	112
Importance of studying Akt membrane localization	113
Importance of studying the timings of Akt activity.....	114
Caveats and future work	115
Conclusions.....	118
CHAPTER SIX: CONCLUSIONS AND FUTURE WORK.....	120
6.1 SUMMARY OF METHODOLOGIES.....	120
6.2 SUMMARY OF CONTRIBUTIONS.....	122
6.3 FUTURE WORK	123
APPENDICES.....	125
PAPERS AND PRESENTATIONS	129
REFERENCES	130

SUMMARY

The complexity of cell signal transduction creates challenges for linking the observed effects to the underlying signaling pathways. Mathematical modeling of cell signaling can provide insights into the systems-level effects of the pathways being studied, by simulating how protein levels changes with time (*i.e.* pathway dynamics). An important problem in building dynamic models of signaling pathways is parameter estimation, which is to estimate the reaction rate constants given the measured concentrations over time of the pathway species. Proteomics technology is starting to provide complete datasets (Mann, et al., 2013), and it is reasonable that a growing category of future parameter estimation problems would have time-series abundance of all species in the network. A class of parameter estimation methods called spline-based collocation methods can exploit the data abundance to avoid the bottleneck of numerical integration, but such methods have not achieved competitive runtime nor been widely adopted in user-friendly tools. Employing systematic search and curve shape agreement, we converted the parameter estimation problem into an instance of an inferencing technique called belief propagation to develop an efficient spline-based collocation method. We developed computational tools for systematic parameter estimation of data-rich experiments (SPEDRE). SPEDRE has unique asymptotic behavior with runtime polynomial in the number of molecules and timepoints, but exponential in the degree of the biochemical network. SPEDRE thus can exploit large data sets, which are aligned to recent

developments towards complete proteomics. In comprehensive comparisons with state-of-the-art parameter estimation methods, SPEDRE showed superior or comparable performance in large-scale test cases using artificially constructed networks.

After testing SPEDRE on a series of artificially constructed networks, we next applied the SPEDRE method on a real-life pathway which describes the serum-induced activation of the kinase Akt. Unexpectedly, the constructed model revealed puzzling Akt pathway dynamics that motivated further modeling study. Akt activity in mouse embryonic fibroblasts shows an overshoot and decline after serum stimulation, but this dynamic signaling behavior has not yet been fully investigated by the current literature. We compared the measured dynamics of phosphatidylinositol(3,4,5)-trisphosphate (PIP3) and Akt-phospho^{Thr308} (Aktp³⁰⁸) with computational models of pathway mechanisms, aiming to explain the overshoot of Akt activation after serum stimulation. ODE models were constructed based on literature evidence and measured time-series concentrations for model calibration. Time-course simulation showed inconsistency between the peak times of PIP3 (2min) and Aktp³⁰⁸ (30min). By systematically simulating non-canonical mechanisms for resolving this timing difference, we identified four potential hypotheses and constructed ensembles of ODE models to evaluate each hypothesis. Motivated by model predictions, experiments were performed to investigate the dynamics of membrane total Akt and membrane Aktp³⁰⁸ in cells treated with serum. These measurements yielded the following insights: Akt is sequestered at the

membrane for a prolonged period of time after PIP3 recruitment; and the delayed activation of Aktp³⁰⁸ in total cell lysate is caused by the delayed activation of membrane Aktp³⁰⁸. A hypothesis management analysis of five potential non-canonical mechanisms of augmented Akt phosphorylation supported the following hypotheses: augmented Akt recruitment to the membrane and Aktp³⁰⁸ sequestration at the membrane.

LIST OF TABLES AND BOXES

Table 2.1 – A list of tools for analysis and simulation of physico-chemical models that have been adopted in this thesis research.....	18
Box 3.1 – SPEDRE-base algorithm for computing the MAP estimates on a factor graph.	36
Table 3.1 - Comparison of standalone and hybrid methods on artificial networks of size N=30 to 150.	52
Table 3.2 – SPEDRE’s performance on synthetic networks (circular network, tree network with random branch) and biological networks (PI3K/Akt cascade, MAPK cascade and Actin Filament Assembly / Disassembly pathway).	55
Table 4.1 – Rate constant and nominal values in the Akt model.	73
Table 4.2 – Comparison of rate parameter estimation methods applied to the Akt model.	76
Table 5.1 – Reactions and rate constants used in the H0 model.	85
Table 5.2 – Initial concentrations of the species used in the H0 model.	86
Table 5.3 – Summary of model evaluation for null hypothesis and four alternative hypotheses, based on three tests performed in this study.	110

LIST OF FIGURES

Figure 1.1 –Computational models corresponding to levels of abstraction of links (from abstract to specific) in biochemical networks (reproduced from (Palsson, 2011)).3	
Figure 2.1 – Diagram illustration of the computational modeling approach for hypothesis construction and evaluation.12	12
Figure 2.2 – Exponential growth of year-over-year in terms of Billion Floating-Point Operations per Second (GFLOP/s) for the CPU and GPU (Kirk and Hwu, 2010).17	17
Figure 3.1 – Illustration of computing the approximate derivative using clamped spline interpolation.....30	30
Figure 3.2 – A partial factor graph of the example 2-species system, shown for one timepoint t_j and one experiment e33	33
Figure 3.3 – Illustration of a joint probability table of 3 dimensions, corresponding to rate constants k_1 , k_2 and k_334	34
Figure 3.4 – Processing pipeline for SPEDRE41	41
Figure 3.5 – SPEDRE execution results using MAPK sample derived from (Huang and Ferrell, 1996).....44	44
Figure 3.6 – Performance of SPEDRE on a series of ring networks.47	47
Figure 3.7 – Network diagram for a random artificial low-degreed network of size $N=30$, with 30 species and 30 reaction rates.....49	49
Figure 3.8 – Comparison of standalone and hybrid methods on artificial network containing 130 species and 130 reaction rates.50	50
Figure 4.1 – Lucigenin measurements of superoxide time-series in MEF.69	69
Figure 4.2 - Regulation of superoxide production by NOX family (Brandes, 2003) ...70	70
Figure 4.3 – Network diagram of the Akt model, including redox-regulation of PTEN.72	72

Figure 4.4 – Comparison of parameter estimation algorithms applied to the Akt network, with noise levels 0, 1% and 20%.	74
Figure 4.5 – Time series data from MEF ^{PTEN^{-/-}} cells treated with 10%FBS with or without DPI pre-incubation for 2 hours. Data obtained from Dr. Sharon Lim and quantified by the author.	77
Figure 5.1 – Quantified time-series of PIP3 (dotted line) and Aktp308 (4 solid lines for 4 experimental replicates) in arbitrary units.	84
Figure 5.2 – The canonical model of Akt activation.	88
Figure 5.3 – Five alternative hypotheses, each with one non-canonical effect (in red).	92
Figure 5.4 – Flowchart describing the reverse-fitting method used in this study.	93
Figure 5.5 – Time course simulations of the five alternative models.	94
Figure 5.6 – Time-series western blot fractionation experiments.	95
Figure 5.7 – Comparison between experimental time-series and simulated time courses.	97
Figure 5.8 – Time course simulation of three candidate alternative models.	103
Figure 5.9 – Model ensemble analysis of three candidate alternative models.	104
Figure 5.10 – Model robustness analysis.	108
Figure A1 – Two replicates (A) and (B) of PIP3 immunofluorescence confocal imaging time series measurement in serum-stimulated wild type mouse embryonic fibroblasts (MEF).	127
Figure A2 – Quantified time-series data of membrane total Akt fractions under LY290004 treatment compared with the simulated time course from three alternative models.	128

LIST OF ABBREVIATIONS

4OHT	4-Hydroxytamoxifen
A.u.	Arbitrary unit
Akt	Protein kinase B
API	Application programming interface
CSV	Comma-separated values
DDC	Diethyldithiocarbamate
DEP	Deprived
DMSO	Dimethylsulfoxide
DPI	Diphenyleneiodonium chloride
FBS	Fetal bovine serum
GA	Genetic algorithm
KO	Knock-out
LBP	Loopy belief propagation
LY29	LY290004, a PI3Kinase inhibitor
MAK	Mass action kinetics
MAP	Maximum a posteriori
MAPK	Mitogen-activated protein kinase
MEF	Mouse embryonic fibroblast
MRE	Maximum relative error
$O_2^{\cdot-}$	Superoxide
ODE	Ordinary differential equation
PDK1	Phosphoinositide-dependent kinase-1

PI3K	Phosphatidylinositol 3-kinases
PIP2	Phosphatidylinositol(4,5)-bisphosphate
PIP3	Phosphatidylinositol(3,4,5)-trisphosphate
POF	Product of factors
PSO	Particle swarm optimization
PTEN	Phosphatase and tensin homolog
ROS	Reactive oxygen species
SD	Steepest descent
SILAC	Stable isotope labeling by amino acids in cell culture
SOD	Superoxide dismutase
SPEDRE	Systematic Parameter Estimation in Data-Rich Environments
SRES	Stochastic ranking for evolution strategy
SSE	Sum-of-square error
XML	Extensible Markup Language

CHAPTER ONE: INTRODUCTION

1.1 Signal transduction networks

All living organisms rely on complex biochemical processes to maintain homeostasis and adapt to environmental changes. These mechanisms form highly dynamic and interconnected molecular networks that drive biological behaviors, including cellular decisions, signal transduction, feedback regulation and inter-cellular communication. Intricate systems-level behaviors, such as input–output behaviors and feedback, may arise from the interplay of simple biochemical reactions (Chen, *et al.*, 2009). Three categories of biological networks are mainly studied: gene regulatory network, metabolic pathway and signal-transduction network. These three pathway categories are not mutually exclusive and complex communications between different network types are often involved in any phenotype of the organism. The structure and functions of these networks are among the most active topics currently being studied around the world.

Cell signaling describes critical processes regulating basic cellular mechanisms and homeostasis (Alberts, *et al.*, 2007; Hancock, 2005; Weinberg, 2006). Signal-transduction networks (or signaling pathways) transmit signals from outside the cell to its intracellular response mechanisms through biochemical events (binding without covalent modifications, phosphorylation, nitrosylation, ubiquitination, *etc.*) which trigger specific cellular responses or decisions (Gough and Yaffe, 2011; Scott and Pawson, 2009). With the rapid acceleration of new biological discovery in signaling pathways, many publicly available sources are currently available to share information about signaling pathways, including Science Signaling’s Database of Cell Signaling (AAAS and Stanford, 2012), KEGG PATHWAY database (Kanehisa, *et al.*, 2012), SignaLink (Farkas, *et al.*, 2011), and BioModels database (Li, *et al.*, 2010).

Through signaling pathways, stimuli on the cellular surface such as growth factors are transmitted to molecules that are capable of carrying out certain responses, such as cell fate decisions, gene expression changes, and protein synthesis. Such behaviors resemble a molecular circuit with different responses (outputs) to different cues (inputs). This translation of environmental cues to cellular behaviors inevitably involves such complexity that makes studying signaling networks a major challenge to biologists without the aid of computational simulation. Mathematical modeling of signal-transduction networks has contributed to several exciting biological discoveries in recent years (Hughey, *et al.*, 2010; Janes and Yaffe, 2006).

1.2 Systems biology

A chief aim of systems biology is to determine how multiple individual components together produce a complex behavior (Kholodenko, *et al.*, 2005). For example, Akt activity is determined by dynamic competition between many simultaneous individual reactions including protein phosphorylation, translocation, and dephosphorylation, not to mention lipid phosphorylation and dephosphorylation. Under the systems biology paradigm (Fall, *et al.*, 2002; Palsson, 2006), studying the interactions between the signaling species may lead to the discovery of systems-level properties. Different types of model may apply to the biochemical network depending on the levels of knowledge about the reactions, ranging from abstract to specific (Figure 1.1).

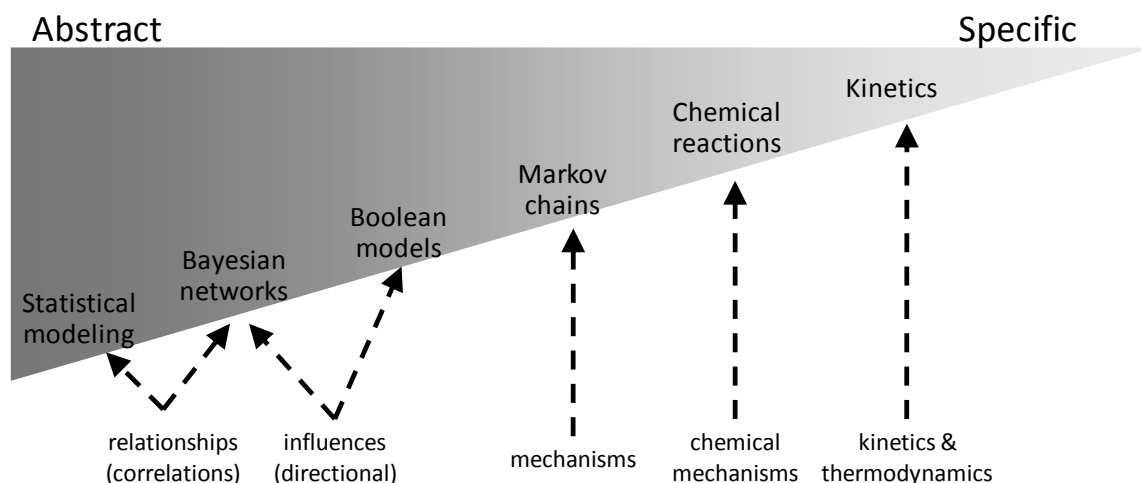


Figure 1.1 –Computational models corresponding to levels of abstraction of links (from abstract to specific) in biochemical networks (reproduced from (Palsson, 2011)).

Statistical modeling and Bayesian networks are modeling techniques that describe non-directional relationships (statistical correlation) between biological entities. Boolean modeling and Bayesian networks describe the causal or statistically determined relationships between network components. Markov chains deal with the general mechanisms of the network. Chemical reactions and kinetics modeling describe the specific biochemical reactions occurring within the biological networks.

A recurring theme in systems biology which manifests in this thesis work is integration: between computational technologies and biological questions, of different model abstraction levels, and of different disciplines of science. First, biologist collaborators were often unfamiliar with the use of computational modeling in experiment design and required intensive interactions to elucidate how the models could meet their needs. Second, biological modeling could integrate cellular localization information into the kinetics models, which we found to be effective in designing biological experiments that could lead to biological discovery. Finally, various disciplines are involved in systems biology studies as an integrated effort to unravel complex behaviors at the system level. As clear evidence to this, the author has had an opportunity to interact with collaborators from different fields of study, including computer science, biochemistry and physics.

1.3 Some ongoing challenges in systems biology

Systems biology faces a range of technical and organizational challenges (Aderem, 2005), and this dissertation addresses two specific challenges: (1) constructing

predictive models, and (2) estimating parameters of kinetic models. Inferring biologically relevant hypotheses for experimental validation involves large amount of information and automation of the process is not yet well developed. Many state-of-the-art modeling studies still rely heavily on human intuition for model and experiment design (Albeck, *et al.*, 2008; Basak, *et al.*, 2007; Purvis, *et al.*, 2008). In addition, even when models have been constructed, inferring kinetic reaction rates from time-series concentration measurements is known to be a nonlinear high-dimensional problem which is difficult to solve satisfactorily (Kleinstein, *et al.*, 2006).

Constructing predictive kinetic models of signaling pathways

Kinetic modeling requires to a certain extent the knowledge of the concentration of signaling proteins, and the kinetic parameters for each biochemical reaction. It is commonly observed that the cellular processes that are being modeled often contain poorly understood aspects. Further, the temporal dynamics of cell signaling pathway is complex and unintuitive, as the dynamics of proteins in the pathways are often interdependent.

Time- and resource-consuming biochemical experiments typically generate limited and often inconsistent data, which present a major challenge in modeling biological networks (Eungdamrong and Iyengar, 2004). Further, most large datasets inherently contain technical and biological noise, or various types of systematic and human error. Typically only a small number of species are measured for a batch of samples, whereas the desired results are the simultaneous measurements of different parameters in the same sample. Recently there have been more advanced quantitative proteomics technologies such as SILAC (Stable Isotope Labeling by Amino acids in Cell culture) that have increased the amount of data at an exponential rate (Reeves, *et al.*, 2009; Tasaki, *et al.*, 2010). However the published data are often on different cell lines,

under different treatment conditions and prone to different levels of data error. This makes comparing model against available datasets a serious challenge.

As quantitative experiment data are scarce and many kinetics parameters are unknown, models often become underdetermined and have poor predictive power. Additional experiments are often required to better calibrate models, but experiments are time- and resource-consuming. Prioritizing experiments to minimize cost and maximize information gain is an important goal in pathway modeling studies. A concrete example of how this goal is achieved can be found in this thesis work: ODE models are constructed to study dynamic behaviors of a signaling pathway, and modeling efforts points out which experiments are more likely to yield fruitful results.

Estimating kinetic model parameter based on time-series protein concentrations

In addition to building predictive network models, our next goal is to obtain the model parameters. Kinetic rate parameters are often unknown in many biochemical reactions and are technically difficult to determine experimentally (Eungdamrong and Iyengar, 2004). Further, many enzyme assays to measure the rate constants are usually conducted *in vitro* with purified components while the interaction may have vastly different kinetics *in vivo* due to scaffolding, local concentrations of the reactants, or molecular crowding.

While it is possible in theory to estimate reaction rate parameters based on the time-series measurements given a biochemical network, the computation in practice is often intractable. Even tractable problems are often overwhelmed by suboptimal solutions, or obscured by noise. Using ODEs to represent the production and consumption rates of the biochemical systems, the estimation of the kinetic rate constants can be formulated as a nonlinear optimization task, which is known to be a difficult problem. As the number of unknown rate constants increases with larger pathways, the parameter

space becomes astronomical and the estimation is often too computationally costly to be practical or too inaccurate to give useful prediction. A highly desirable goal is therefore to computationally estimate unknown rate constants in a signaling pathway model accurately and efficiently. Indeed, the estimation of parameters for ODE models has been posted as a challenge for the Dialogue for Reverse Engineering Assessments and Methods project (DREAM6, 2011, available at <http://www.the-dream-project.org>), a yearly competition for worldwide researchers to address the fundamental questions about systems biology (Stolovitzky, *et al.*, 2007).

In addition, a crucial computational challenge is to design software packages that are easily accessible to the broad community. With the availability of faster and more reliable web-based resources, a fast developing trend is to deploy applications as web services that can be run on any platform with internet connectivity. In this study, we developed such a web service for a parameter estimation tool (available at <http://webbppe.nus.edu.sg:8080/opal2/SPEDRE>) which performed efficiently on a niche of problems with sparse connectivity and abundant species concentration measurements.

1.4 Thesis research objectives and organization

Research objectives

This thesis research focused on two specific topics, each dealing with a different scale and possessing a different set of characteristics within the context of systems biology. The first topic was “data-rich parameter estimation”, which aims to develop a method for estimating the reaction rates in a signaling pathway. As data-rich environments are increasingly feasible due to new proteomic technologies, our novel parameter estimation method (called SPEDRE) exploits this opportunity to achieve efficiency. SPEDRE makes a set of tradeoffs for improving efficiency in data-rich contexts, making it successful in low-degreed but not all types of networks. SPEDRE

exploits the data richness to avoid solving the system of ordinary differential equations (ODEs) numerically. Instead of computing the “ $d[\text{concentration}]/dt$ ” values (slow), but it instead interpolates the $d[\text{concentration}]/dt$ values from data (fast). A low-degree model of Akt activation is used for comparing SPEDRE with current state-of-the-art methods. This research topic will be covered in Chapters Three and Four.

Further work with the Akt model eventually revealed a previously unknown mismatch between the canonical pathway and the observed behavior. Although PIP3 is close to Akt in the pathway, the time of peak PIP3 after serum stimulation was dramatically different from the time of peak Akt activation. This motivates the second topic of this thesis study, “modeling of Akt phosphorylation upon activation by growth factors”, where we seek to elucidate the mechanisms causing the large time delay between PIP3 and Aktp³⁰⁸ in mouse embryonic fibroblasts (MEF) upon serum-induction. The mismatch between the canonical model and data was confirmed quantitatively based on model simulations, suggesting the presence of non-canonical species. We propose novel modeling-driven methodology, “hypothesis management”, for building alternative models for reconciling the peak time mismatch. Hypothesis management results in extensive interfacing between computational modeling and wet-lab experiments, and several novel biological insights are discovered during this process. This specific modeling approach with alternative hypotheses about the Akt pathway carries constraints that make SPEDRE not applicable, and we instead employed state-of-the-art methods for the important task of parameter estimation. This topic is the heart of the thesis, and will be covered in Chapters Four and Five.

The CHEGS research approaches

In this thesis, we develop a common set of modeling-driven approaches applicable to both research topics. While some techniques were directly applied to the research

problem, others were more implicit and abstract. These commonalities can be described as follow: application of *Computational* methodologies to biological questions, *Heuristics*-based evaluation of alternatives, evaluation of maximum *a posteriori* (MAP) *Estimates*, sacrificing complexity in favor of *Generalizability*, and *Systematic* evaluation of alternatives (or CHEGS).

The first common approach is to interface between the *Computational* methodologies and the biological application. Many computation tools were traditionally developed in other fields such as engineering and applied mathematics, and recently many studies have started to adopt these technologies to biology. Machine learning tools, such as clustering and classification, allow biologists to discover knowledge from the large and noisy datasets. Visualization tools help display complex data into forms that agree with human perception. Tools belonging to the “systems biology” categories, such as mathematical modeling, can help integrate different data sources into a unified conceptual framework surrounding the biological question of interest. High-performance computing tools, such as parallel and cluster computing, enable other computational methods to perform at high efficiency, to provide biological discovery with higher throughput and lower latency. These are typical ways that computational improvements can be applied to biological needs, and analogous applications can be found throughout this thesis.

The second research technique is to use *Heuristics* based on biological practicality. The *American Heritage Dictionary* definition of heuristics is “a usually speculative formulation serving as a guide in the investigation or solution of a problem”. Heuristics serve our goals well because our biological questions are often not well-formulated and the literature evolves rapidly with a constant stream of new evidence and findings. Thus for practical purposes, models were constructed based on current

biological evidence and understanding of the literature consensus, to carry out some useful functions. This research adopts heuristics to construct models that are useful for answering biological questions rather than making complex models. The common research technique is applied in Section 3.4 and 5.4 of the thesis.

The third research technique seeks to evaluate the maximum *a posteriori* (MAP) Estimates of the alternative outcomes. MAP estimation is a mathematically principled, well-developed, and widely used method in the field of Bayesian statistics (Degroot, 1970). This technique has the advantage of being less prone to human bias in hypothesis evaluation. This method was applied the parameter estimation work (Section 3.3) and a more indirect use of the method was applied to the Akt modeling study (Section 5.3).

The fourth research approach deals with sacrificing complexity to gain Generalizability. This serves to avoid the problem of overfitting, described by Tetko *et al.* as when a model describes random error or noise instead of the underlying relationship (Tetko, *et al.*, 1995). Typically, more complex models with a larger number of parameters are very successful at fitting training data (data used in model fitting), and yet often fail to extrapolate to test data (data not used in model fitting). On the other hand, models with fewer parameters may produce poorer match with training data but can be more generalizable when fitting with test data. As making useful prediction is the main goal of modeling, all projects in this thesis prefer simpler models whenever possible, to avoid the overfitting problem. The selection of simpler models allowed us to gain computational performance or conceptual simplicity, but at the cost of accuracy or precision. This common approach appears in Section 3.4 and 5.4 of the thesis.

Finally, the last research approach employs systematic investigation of alternatives, with complete coverage at low resolution, and with explicit evaluation for the merits of each alternative. There are different ways to achieve the goal of systematic

evaluation of alternatives. The “data-rich parameter estimation” work presents an example of systematic evaluation of alternatives computational during the program execution. At the conceptual level, the “modeling of Akt phosphorylation upon activation by growth factors” work achieves systematicity by enumerating the finite number reactions and construction hypothesis for modifying each of the reactions. Further, systematicity is also achieved by the use of spline to represent any dynamic of perturbation, not just some simple pseudo-species driven by a first-order effect downstream of serum stimulation. This common approach appears in Section 3.4 and 5.4 of the thesis.

Thesis organization

Chapter Two describes the materials and methods employed in this thesis. Chapter Three of the thesis describes the novel parameter estimation methodology for data-rich biochemical pathways. Chapter Four presents a biological test case to benchmark the novel method with the current state-of-the-art parameter estimation techniques. Chapter Four has a special role in bridging the topic of “data-rich parameter estimation” in Chapter Three to the topic of “modeling of Akt phosphorylation upon activation by growth factors”, as presented in Chapter Five. Finally, Chapter Six concludes the dissertation with a summary and a description of future work. Chapter Three to Chapter Five are partially adapted from jointly co-authored manuscripts, and the contributions from the author of this thesis can be found in the following “Author contributions” subsection.

Author contributions

Efforts from multiple parties are involved to make the collaborative research possible. The author has done the best attempts to give credit to the contributing authors,

at the relevant text in the thesis (*e.g.* figure legends, protocol descriptions). In addition, below is a summary of the author contributions (ideas, data) to this thesis work:

- Experimental data for Akt modeling work: Luo Le, Sharon Lim
- Experimental protocol description: Luo Le (Section 3.7 quoted text)
- Experimental design (Akt modeling, SPEDRE): Lisa Tucker-Kellogg, Jacob K. White, Marie-Véronique Clément
- All manuscripts were maintained by Tri Hieu Nim
- First draft of the Akt modeling manuscript: Tri Hieu Nim
- First draft of the SPEDRE manuscript: Tri Hieu Nim (Methods and Results), Lisa Tucker-Kellogg (Introduction and Discussion)
- Manuscript revision: Tri Hieu Nim, Lisa Tucker-Kellogg, Marie-Véronique Clément
- Concept of product of functions (POF) alternative cost function: Lisa Tucker-Kellogg
- Preliminary source code for parameter estimation using belief propagation on biochemical networks: Lisa Tucker-Kellogg
- Concept of maximum relative error (MRE): Jacob K. White
- Clamped spline in SPEDRE: Tri Hieu Nim
- Revised source code for SPEDRE, web server implementation, test cases implementation and benchmarking comparison: Tri Hieu Nim
- Source code of automating benchmarking comparison source code with COPASI (Hoops *et al.*, 2006) for standalone and hybrid methods for parameter estimation: Tri Hieu Nim

CHAPTER TWO: MATERIALS AND METHODS

2.1 Modeling-driven pathway analysis

This thesis study extensively employs computer models for hypothesis construction and evaluation (Figure 2.1). This approach is particularly powerful in studying pathways where many signaling species participate in highly intertwined and sometimes non-intuitive networks.

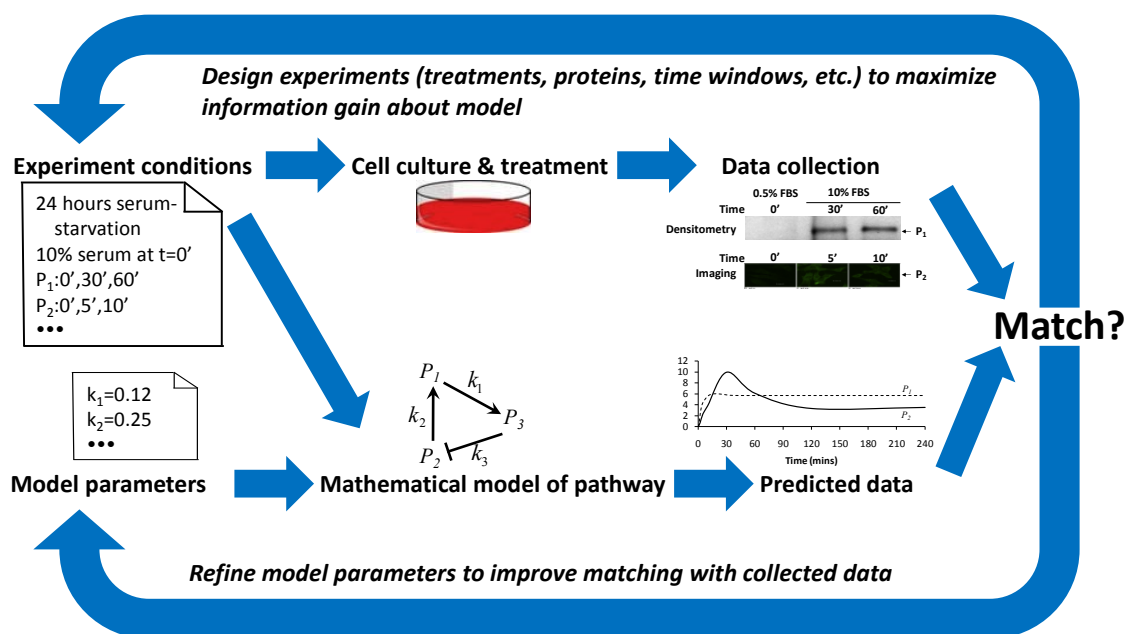


Figure 2.1 – Diagram illustration of the computational modeling approach for hypothesis construction and evaluation.

Mathematical models of pathways evolves side-by-side with benchwork experiments. Comparison between model simulation and measurements provides information for refinement of model parameters and for designing experimental conditions.

2.2 ODE model

To model the biochemical behavior of the system, we used a system of ODEs to describe the time-evolution of the species concentrations in the pathway system. The model describes the dynamics of the inputs and observables which vary according to experimental conditions.

Letting s denote species name and e denote experiment index, the change of the transient concentration $x_{s,e}$ over time can be represented in ODE form as

$$\frac{d}{dt} x_{s,e}(t, \mathbf{k}) = f_{s,e}(\mathbf{x}(t, \mathbf{k}), \mathbf{i}(t), \mathbf{v}(t, \mathbf{k}), \mathbf{k}) \quad (2.1)$$

where t is the transient time point, \mathbf{k} is a set of every parameter in the system, $\mathbf{x}(t, \mathbf{k})$ is a set of every experiment-dependent species $x_{s,e}(t, \mathbf{k})$ in the system, $\mathbf{i}(t)$ is a set of every experiment-dependent input $i_{s,e}(t)$ to the system represented by a predefined time-evolution function, $\mathbf{v}(t, \mathbf{k})$ is a set of every variable curve $v_{s,e}(t, \mathbf{k})$ represented by linear spline curves whose knots are defined by the parameters in \mathbf{k} , and $f_{s,e}$ is a function derivable from the biochemical reactions in the system which may involve a combination of species, inputs, variables and parameters in the system.

The process of model calibration can be expressed as an optimization problem as

$$\min_{\mathbf{k}} \{\text{SSE}\} \equiv \min_{\mathbf{k}} \left\{ \sum_s \sum_e \sum_t w_{s,e} \cdot \left(x_{s,e}^{data}(t) - x_{s,e}(t, \mathbf{k}) \right)^2 \right\} \quad (2.2)$$

where $x_{s,e}^{data}(t)$ is the measured data point, $w_{s,e} = \frac{n_t}{\sum_t \left(x_{s,e}^{data}(t) \right)^2}$ is a time-independent

inverted mean-square weight calculated based on the observed data, and n_t is the number of time points. By performing the optimization task described in Equation 2.2, we obtained \mathbf{k}^* , a set of optimized parameters in the system.

Models were implemented and simulated using Matlab (v.7.6, The MathWorks, MA) with SBToolbox2 toolkit (Schmidt and Jirstrand, 2006) to perform *in silico* simulation. Models were available in TextBC format, which contains model states, model variables and model reactions information. Standard configuration was used for ODE simulation in SBToolbox2 and its SBPD extension package (Schmidt and Jirstrand, 2006).

2.3 Linear spline for reverse fitting

In the Akt modeling study (Chapter Five), we constructed a null-hypothesis model (H0) which describes the canonical pathway for Akt activation. From this H0 model, the

alternative hypotheses were constructed, each having a hypothesized input species. As the dynamics of the input species may be unknown, this leads to a reverse-fitting problem that has been previously addressed (Apgar, *et al.*, 2008; Chu and Hahn, 2008; Thomaseth, *et al.*, 1996).

We used a novel approach in which the unknown input species is represented by a linear spline curve whose knots become parameters of the system. The model for each alternative hypothesis (*e.g.* recruitment, retention hypothesis) contains a newly introduced variable (*e.g.* “recruitment effect”, “retention effect”) whose concentrations are obtained from a linear spline. The spline is constructed by linearly interpolating between every consecutive pair of spline knots, whose value are subjected to optimization in the parameter estimation process.

2.4 Model complexity reduction

As a more complex model is more likely to agree with data after parameter optimization (due to overfitting), assumptions and constraints were imposed on model construction (as seen in Figure 5.2, Table 5.1-5.2 of Chapter Five) and model optimization. The direct conversion reactions (#2 and #5) were represented using mass action kinetics. The enzymatic reactions (#4 and #6) were represented using Michaelis-Menten equations. To treat PIP3 a system input whose concentrations do not depend on the ODEs, the reactions involving PIP3 recruitment (#1 and #3) treat PIP3 as a simple multiplier. The knots for the linear spline were introduced sparingly to avoid the problem of overfitting. As a general rule, the rate constants are assumed to be the same for all experiments while initial concentrations while input and variables may be experiment-specific. Identifiability analysis was performed during model construction, and the parameters which were strongly correlated to other parameters were removed. These steps resulted in a smaller subset of \mathbf{k} , which were used in subsequent simulations.

2.5 Parameter estimation (non-SPEDRE)

As we developed a parameter estimation method called SPEDRE as a part of this thesis study, more background and mathematical description for parameter estimation process will be covered in greater detail in Chapter Three. However it should be noted that the SPEDRE method developed in Chapter Three is not applicable to the models described in Chapter Five, as the low-degreed network requirement is not met. As a result, SBToolbox2 and its SBPD extension package (Schmidt and Jirstrand, 2006) were used for parameter estimation. In this section, we will describe the parameter estimation procedures used in the modeling study of Akt phosphorylation upon activation by growth factors, in non-mathematical language and in the context of the toolboxes used.

Whenever applicable, published data and kinetic rate constants (Hatakeyama, *et al.*, 2003) were adopted to ensure that the model does not violate biological knowledge (See Table 5.1 and 5.2). The remaining parameters were fitted to observed data (see Figure 5.1 and 5.6) in the process of model calibration. Parameter estimation was performed in multiple steps using the global search Particle Swarm Optimization (PSO) algorithm (Kennedy and Eberhart, 1992), the local search Nelder-Mead (NM) algorithm (Nelder and Mead, 1965) and manual tuning. For any combination of these steps, the final step always used the Nelder-Mead algorithm.

When performing parameter estimation using a standard algorithm (PSO, NM), multiple-fit strategy was used. Each fit iteration applied an exponential noise ($\alpha=0.5$) to the initial guess of all parameters before performing parameter estimation. Note that as the model changes its parameters after each round of parameter estimation, the initial guess for each run of parameter estimation changes every time. After 100 iterations, the parameter result with lowest sum-of-squared error (SSE) was retained for the subsequent steps of the parameter estimation pipeline.

Manual tuning refers to the process of manually adjusting each parameter to guide the simulation to match the observed data. The procedure was applied when multiple-fit parameter optimization was trapped in a local minimum and failed to return reasonable match with data, judged by the features of interest such as peak time and peak width. This approach can be effective in cases where even a hybrid method (global search followed by local search) fails to give reasonable match.

In constructing the alternative scenarios to the canonical model, we introduced a new variable (*e.g.* “recruitment factor”, “retention factor”, etc.) and we represented its concentration over time using a linear spline. The spline knots were a part of the system parameters, and would be optimized during parameter estimation. The model calibration process might also modify the rate constants and initial concentrations used in the canonical model, in addition to the spline knot parameters.

2.6 Analysis of model families/ensembles

The parameter estimation process generated a “nominal” model for each hypothesis. Subsequently, we constructed families of models for each alternative hypothesis based the “nominal” model, where each nominal parameter was multiplied by a factor between 0.1 and 10. This is similar to performing a local parameter sensitivity analysis. Based on the set of simulated time courses of each model, we abstracted the information into a peak vector, consisting of peak time, peak amplitude and peak width (distance between 90%-peak values before and after the peak) of four observables.

2.7 Computational resources and modeling tools

This research takes place in an era when emerging powerful technologies have enabled the handling of previously infeasible tasks. Massively parallel processing, provided by GPUs, has led to impressive growth (Figure 2.2). Advances in cloud technology have also enabled the execution of computationally costly tasks from lower-

end client machines. This research has made use of these technologies to speed up the process of solving challenging biological problems *in silico*. Cheaper computing has also enabled this study to perform systematic evaluations of all alternatives (see Section 1.5), which has the advantages of covering search spaces more completely and avoiding bias.

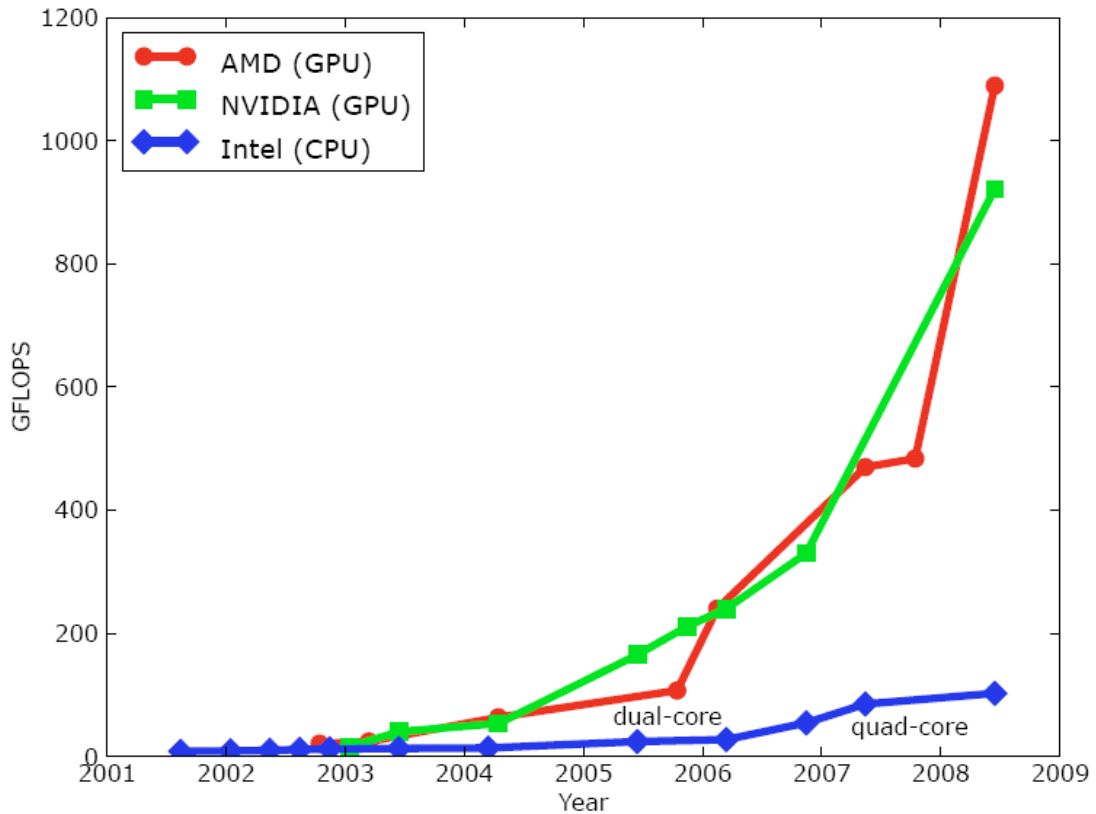


Figure 2.2 – Exponential growth of year-over-year in terms of Billion Floating-Point Operations per Second (GFLOP/s) for the CPU and GPU (Kirk and Hwu, 2010).
 Three of the most popular manufacturers are described: AMD, NVIDIA and Intel.

Computer modeling and web-based resources have been progressively facilitating studies of biochemical networks such as signaling pathways (Klipp and Krause, 2011). Various computational tasks (in computational biology applications) are increasingly being aided and facilitated by the availability of specialized and general-purpose modeling tools (enumerated in Table 2.1) to perform model coding, model analysis and parameter estimation.

Tool	Functionality	References
COPASI	Notation, analysis, and simulation of biochemical models. Represented in ODE format. Supports stochastic simulations.	(Hoops, et al., 2006)
CellDesigner	Graphical representation and formatting of biochemical networks; supports ODE model implementation and simulation.	(Funahashi, et al., 2003)
SBML Toolbox	A toolbox of multiple functionalities for SBML models (MATLAB-based); supports reading, writing, graphical presentation, and simulation	(Keating et al. 2006)
SB Toolbox	A toolbox (MATLAB-based) for simulation of ODE models; supports parameter estimation, bifurcation analysis, steady state analysis, and model reduction.	(Schmidt and Jirstrand 2006)
SBW	A common framework to facilitate communication and combined use of heterogeneous applications; support models in SBML format	(Hucka, et al., 2002)

Table 2.1 – A list of tools for analysis and simulation of physico-chemical models that have been adopted in this thesis research.
Details and availability of each tool can be found in the corresponding reference. The tool names were last verified in 2012 by the author.

2.7 Experimental methods

All experiments in this study were either carried out by Dr. Luo Le (Department of Biochemistry, NUS) or by the author under the supervision Dr. Luo Le (“supervised experiments”). This section describes the protocols for the experiments involved, including quotations from the original text description in Dr. Luo Le’s thesis (available at <http://scholarbank.nus.edu.sg/handle/10635/27948>). The quoted text has been formatted and highlighted to avoid any confusion.

Cell culture

MEF cells were maintained in Dulbecco’s modified Eagle’s medium/high glucose (DMEM) supplemented with 2mM L-glutamine and 1mM gentamicin. Cells were incubated in a 5% CO₂ incubator at 37°C. Cells were grown in DMEM containing 10% fetal bovine serum (FBS). Under serum starved condition, cells were starved in DEMD containing 0.5% FBS.

Treatment conditions

In wtFBS experiments, MEF cells were kept in serum starvation for 24 hours prior to measurement. Cells were treated with 10% FBS at the time of measurement ($t=0$).

Time course measurements assay

Time-series concentrations were measured based on for PIP3 fluorescence (used as model input) and Aktp³⁰⁸ (used as model observable). Immunoblotting experiments to measure total Akt and Aktp³⁰⁸ were performed according to (Lim and Clément, 2007). Immunodetection of PIP3 level and confocal laser scanning microscopy was performed as described in (Lim and Clément, 2007).

Lucigenin assay

Cells were seeded and serum-deprived in 0.5%FBS/DMEM or maintained in 10%FBS/DMEM before various drug treatments. In supervised experiments, cell culture was prepared by Dr. Luo Le and the subsequent steps of the assay were performed by the author, as described below. At different time points, cells were washed once with 1xPBS, trypsinized and harvested. Cell pellet was collected after centrifugation at 2000rpm at room temperature for 1 minute. The pellet was then resuspended and permeabilized in 430 μ l 1x somatic cell ATP-releasing reagent, 400 μ l of which was used for measurement. Proton emission was recorded for 30 seconds with the Sirius luminometer (Berthold Technologies, Germany) after 100 μ l of 850 μ M lucigenin solution was injected automatically before reading. A blank control containing only 400 μ l 1x somatic cell ATP-releasing reagent was used to monitor the signal from auto oxidation of lucigenin if there was any. The intracellular O₂⁻ level was expressed as the luminescence unit after being normalized with the protein concentration (determined with the 30ul suspension left from the assay). The changes in O₂⁻ level under different treatments were reported as the percentage relative to the respective control cells.

Measurement of PIP3 by Immunofluorescence and Confocal Microscopy

In supervised experiments, cell culture was prepared by Luo Le and subsequent steps were carried out by the author. Cells grown on cover slips were washed once with 1x PBS and fixed in 4% paraformaldehyde for 20 minutes. After quenching with 100 mM NH₄Cl and washing with PBS, the cells were permeabilized with 0.25% saponin for 10 minutes at room temperature. The cells were blocked in 2% BSA, 5% FBS in 1 x PBS and incubated with FITC conjugated anti – PIP3 antibody (Echelon, Salt Lake City, UT) at a dilution of 1:50 for 1 hour at room temperature. The cells were washed three times before the cover slip was mounted for confocal analysis using a Carl Zeiss Lsm510 META microscope with identical acquisition parameters for the same imagesession.

The experiments listed in the subsections below were performed by Dr. Luo Le. These experiments, however, played a critical role in the outcome of the author's thesis research. The following text was quoted from Dr. Luo Le's thesis (Section 2.2), with the sole intention of aiding the interpretation of the biological data described in this thesis.

"Western blot analysis

SDS-PAGE and Western blot analysis were used to detect the phosphorylation level of Akt, total level of Akt, and total level of PDK1. Cells were washed once with cold 1x PBS and collected in PBS. The cell pellet was then lysed in the lysis buffer (50mM Tris-HCl pH7.4, 150mM NaCl, 1mM EGTA, 1mM EDTA, 0.5% (v/v) Triton X-100) containing 1mM PMSE, 5µg/ml leupeptin, 5µg/ml pepstatin A, 1µg/ml aprotinin and 1mM of sodium orthovanadate. Before measurement of protein concentration, the lysate was centrifuged at 14,000rpm for 10 minutes to remove the debris. Protein quantification was performed using the Coomassie Plus™ Protein assay reagent (PIERCE, Thermo Fisher Scientific Inc, Rockford, IL, USA). SDS-PAGE was performed using the Bio-Rad Mini-PROTEAN® 3 Cell (CA, USA). The stacking gels used were 4% and the resolving gels used were 6.5%, 8% or 12% depending on the size of the target proteins. Protein samples were mixed with the 5x loading dye (0.313M Tris HCl (pH 6.8), 10% SDS (w/v), 0.05% bromophenol blue, 50% glycerol and 0.5M DTT) and heated at 95°C for 5

minutes before loading. Gel electrophoresis was conducted in the 1xSDS/Glycine buffer at 100V for 12% gel or at 120V for 6.5% and 8% gel. The resolved proteins were transferred onto a nitrocellulose membrane by the wet transfer method using the Bio-Rad Mini Trans-Blot® Cell (CA, USA). The transfer was conducted at 350mA for 1 hour at 4°C. The membrane was blocked in 5% (w/v) milk diluted in 1xTBST (20mM Tris – HCl (pH 7.6), 137mM NaCl, and 0.1% Tween 20) for 1hour at room temperature. The membrane was washed with TBST to remove excess milk before blotted with respective primary antibodies (diluted in 5% (w/v) BSA) overnight at 4°C. After washing off the unbound primary antibody with TBST, the membrane was subsequently incubated with the respective horse radish peroxidase conjugated secondary antibodies (diluted in 5% (w/v) milk) for 1 hour at room temperature. The detection was then performed with the Enhanced Chemiluminescence (ECL) using the Supersignal west Pico chemiluminescent substrate (PIERCE, Thermo Fisher Scientific Inc, Rockford, IL, USA). For re-probing the same membrane for different proteins, the membrane was stripped in the Restore Western Blot Stripping Buffer by 5 minutes incubation at room temperature plus 10 minutes incubation at 37°C. The membrane was then blotted with primary antibodies and respective secondary antibodies. For densitometric analysis, the blots were scanned with EPSON Perfection 1250 and analysed by FujiFilm Multigauge V3.0.

Membrane fractionation

Membrane fractionation was performed as described previously (Taylor, *et al.*, 2000). Cells were washed once and collected in ice-cold PBS. The cell pellet was resuspended in fractionation buffer (20mM HEPES (pH7.4), 5mM NaCl, 10mM MgCl₂, 1mM EDTA) supplemented with 1mM phenylmethylsulfonyl fluoride (PMSF), 1µg/ml leupeptin, 1µg/ml pepstatin A, 1µg/ml aprotinin and 1mM sodium orthovanadate. Cells were lysed by 20 strokes with a dounce homogenizer at 4°C. The debris was removed by centrifugation at 700g for 10 minutes at 4°C. The P100 and S100 fractions were further separated by high speed centrifugation (100,000g for 30 minutes at 4°C). The P100 fraction was then lysed in fractionation buffer containing 0.5% (v/v) Triton X-100. S100 and P100 fractions were then analyzed by SDS-PAGE and Western blot. For membrane fractionation, cadherin and SOD1 were used as membrane and cytosolic markers respectively. Absence of each marker in the opposite fraction showed the purity

of the fractionation process. Moreover, they served as loading controls for the corresponding fractions. "

2.8 Data normalization.

Raw data were normalized before model fitting, partly because experimental data were acquired by different assays (western blotting, confocal imaging), and partly to bring the data to the same scale as described by earlier model (Hatakeyama, *et al.*, 2003). Time series data (Akt total, Akt^{p308}, PIP3, and PDK1) were rescaled using the same normalization scheme (defined by the scale and offset values) for all experiments. Total cell lysate data were offset and normalized to have a highest value of 10. Membrane fractionation data were offset and normalized such that the concentration of a membrane fraction is never greater than that of total cell lysate. The quantification and normalization processes are available at the supporting website (<http://webbppe.nus.edu.sg:8080/Akt>).

CHAPTER THREE: DATA-RICH PARAMETER ESTIMATION METHOD (SPEDRE)

3.1 Introduction

Dynamic behaviors of biochemical networks can be captured by ordinary differential equation (ODE) models that compute the change of molecular concentrations with respect to time (Bentele, *et al.*, 2004; Chen, *et al.*, 2009; Fall, *et al.*, 2002; Palsson, 2006). For most biochemical pathways with known topology, most reaction rate constants (*i.e.*, the coefficients of the differential equations) are not available from direct experiments. Rate parameters are typically estimated by regression, or fitting the global behavior of the simulated model to the experimentally observed concentrations. This is a difficult high-dimensional non-linear problem, and search strategies often experience poor convergence and local optima (Kleinstein, *et al.*, 2006). The rate parameter estimation problem can naturally be formulated as minimizing a sum of squared errors (SSE), where each error is a difference between simulated concentration and observed concentration, and the summation is over time points and/or experimental treatments.

The task of optimizing the SSE objective function can be attacked using a variety of “traditional” global and local search methods: LM (Levenberg-Marquardt, local), SD (steepest descent, local), SRES (stochastic ranking evolution strategy, global), PSO (particle swarm optimization, global) and GA (genetic algorithm, global) (Fogel, *et al.*, 1991; Kennedy and Eberhart, 1992 ; Levenberg, 1944; Marquardt, 1963; Michalewicz, 1994; Runarsson and Yao, 2000). Local searches typically use nonlinear least squares optimization, and run very quickly, but they only explore the parameter space around a given start value. Therefore, local methods depend on a good initial guess, meaning an initial guess within the basin of convergence of the global optimum. If the objective function is rugged with many local optima, the chance of initializing in the optimal basin diminishes rapidly. Global methods (Moles, *et al.*, 2003) typically use heuristics and

random sampling to explore the entire domain of parameters, and the runtime depends on the level of sampling performed. Despite the “global” terminology, the results produced by such methods carry no guarantee of global optimality, except as a theoretical limit as the sampling time goes to infinity. Many local and global optimization methods have a subclass of problems (number of parameters, amount of data, amount of noise, etc.) for which a particular method performs best. In other scientific areas where optimization is required, hybrid global-local methods have performed well and hybrid methods have recently become popular for rate parameter estimation (Fomekong-Nanfack, *et al.*, 2007; Katare, 2004; Rodriguez-Fernandez, *et al.*, 2006; Zwolak, *et al.*, 2005). Hybrid methods offer the promise of selecting a good region by global sampling, and then quickly selecting the optimal point in that region by local optimization.

Traditional search methods generate a full vector of rate parameters, simulate the model with this full set of parameters, and then accept, reject, or adjust the parameters based on how well the simulation agrees with experimental measurements. For networks with few unknown parameters, these “simulate-and-match” methods have been very successful at finding good values. The search space for parameter vectors is exponential, and the inevitable trend with any type of exponential growth is that there will eventually be a large enough number of unknown parameters, such that reasonable sampling will not explore very many of the “basins of convergence,” and the results will deteriorate. Indeed many high-impact models of biological pathways continue to be built without automating the parameter estimation process (Albeck, *et al.*, 2008; Basak, *et al.*, 2007; Purvis, *et al.*, 2008).

In contrast to standard “simulate-and-match” methods of parameter estimation, spline-based collocation methods have recently been developed that use experimental observations of a protein over time to interpolate the time derivative of the concentration,

rather than computing the derivatives based on simulating the ODEs. Traditional methods minimize the violation of experimental observations, subject to obeying the ODE trajectories, while the spline-based collocation methods can be seen as solving the *dual* optimization problem because they minimize the violation of the ODE trajectories, subject to obeying the experimental observations. Several spline-based collocation methods have been published recently. A spline-based collocation scheme for parameter fitting problems using a modified data smoothing method and a generalization of profiled estimation was proposed by (Ramsay, *et al.*, 2007). A collocation scheme, particularly suited for problems with high noise and short time-course, was introduced by Brewer and colleagues (Brewer, *et al.*, 2008). Zhan *et al.* used non-linear programming (NLP) to optimize the dual objective (Zhan and Yeung, 2011). Note that these spline-based collocation methods require an extensive input dataset with observations for many or all of the proteins. In the past, few large networks had such comprehensive measurements available, but recent trends in proteomic technology (Zhang and Neubert, 2009) suggest that data-rich cases may be increasingly common in the future. Many spline-based collocation methods have been published with claims of good accuracy, but to the best of our knowledge, efficiency and runtime have not yet been compared with state-of-the-art non-spline parameter estimation methods. The asymptotic runtime of spline-based collocation approaches has also been neglected.

Scalability with network size is a major remaining challenge in the parameter estimation field, regardless of the objective function or optimization approach. A common strategy for large systems is to decompose the problem. However, the objective functions of parameter estimation are not generally decomposable. Some decomposition approaches exploit specific situations, such as having derivatives available at all timepoints (Chou, *et al.*, 2006), or having small sub-networks connected by species with

observed concentrations (Koh, *et al.*, 2006). The dual objective functions of spline-based collocation methods are not readily decomposable, but they do exhibit the important property of sparse interdependence (“locality”) between the variables. This locality can be a basis for conditional decomposition.

Belief propagation (see (Meltzer, *et al.*, 2009) review and (Pearl, 1988) textbook) is an inference method for probabilistic graphical networks with sparse interdependence or locality. It can compute the maximum *a posteriori* (MAP) values for variable parameters in a factor graph, given joint probability distributions that describe the dependencies between adjacent variables. For acyclic graphs, belief propagation guarantees exact optima, and for general graphs, a variant called “loopy belief propagation” (LBP) has had empirical success at approximating the MAP (McEliece, *et al.*, 1998; Murphy, *et al.*, 1999).

Our method of Systematic Parameter Estimation in Data Rich Environments (SPEDRE) optimizes the dual objective approximately, via loopy belief propagation. The innovation is conditional decomposition of the problem into local sub-problems, with pre-computed look-up tables for the discretized solutions to the local terms of the dual objective function. SPEDRE provides dramatic improvement in empirical efficiency, and in effect brings the spline-based collocation (dual objective) methods to the same level of efficiency as the state-of-the-art (primal objective) methods. Asymptotic runtime is polynomial with respect to the number of species, parameters and timepoints in the biological networks, while it is exponential only in the degree of the network.

3.2 Preliminaries

Ordinary differential equation (ODE) for mass action kinetics (MAK)

Mass action kinetics (MAK) describes the behavior of solutions as a sum of elementary reactions weighted by coefficients called the reaction rates or the kinetic

constants. The production and consumption of each species can thus be described using ODEs. For example consider a 2-species artificial pathway $A \rightleftharpoons B$. Using k_1 (and k_2) to denote the forward (and reverse) reaction rates, we can model the system as follows:

$$\begin{cases} \frac{d}{dt} A(t, \mathbf{k}) = -k_1 A(t, \mathbf{k}) + k_2 B(t, \mathbf{k}) \\ \frac{d}{dt} B(t, \mathbf{k}) = k_1 A(t, \mathbf{k}) - k_2 B(t, \mathbf{k}) \end{cases} \quad (3.1)$$

Solving Equations 3.1 provides the time evolution of the species, dependent on rate parameter vector \mathbf{k} . The inverse problem, estimating the rate parameters from observed levels of the species, is a deceptively difficult nonlinear optimization problem (Kleinstein, *et al.*, 2006). We define the *degree* of each ODE to be the number of terms in its right hand side, analogous to the node degree in a biochemical network diagram.

Rate constant estimation objective

To estimate the rate constants, the most standard (“primal”) approach is to use a nonlinear least squares technique to minimize the weighted sum of squared error (SSE) objective function

$$\min_{\mathbf{k}} \sum_{e \in \text{Experiments}} \sum_{i \in \text{Species}} \frac{N_t}{\sum_{j \in \text{Timepoints}} (x_{e,i}^{data}(t_j))^2} \sum_{j \in \text{Timepoints}} (x_{e,i}^{data}(t_j) - x_{e,i}^{sim}(t_j, \mathbf{k}))^2 \quad (3.2)$$

where N_t is the number of observed timepoints per experiment, $x_{e,i}^{data}(t_j)$ is the observed concentration of species i in experiment e , and $x_{e,i}^{sim}(t_j, \mathbf{k})$ is the simulated level of species i in experiment e as a function of time and rate constants \mathbf{k} . SSE is the most widely-used objective for evaluating the success of parameter estimation, but size of the SSE error (which is expected to grow with the number of things being summed) grows with the size of the network. Therefore we also employ the species maximum relative error (MRE), and parameter percentage error (PPE), defined as follows:

$$\text{Species MRE} = \max_{i,j} \left(\frac{N_t}{\sum_m (x_i^{data}(t_m))^2} \cdot (x_i^{data}(t_j) - x_i^{sim}(t_j, \mathbf{k}))^2 \right) \cdot 100\% \quad (3.3)$$

$$\text{Median PPE} = \text{median}_i \left(\frac{|k_i^{\text{estimated}} - k_i^{\text{nominal}}|}{k_i^{\text{nominal}}} \times 100\% \right) \quad (3.4)$$

$$\text{Maximum PPE} = \max_i \left(\frac{|k_i^{\text{estimated}} - k_i^{\text{nominal}}|}{k_i^{\text{nominal}}} \times 100\% \right) \quad (3.5)$$

Besides conventional SSE values, we also assessed the parameter estimation quality using the species maximum relative error (species MRE), a dimensionless metric. Species MRE is an improvement over SSE in this case because MRE does not depend on size of the system, and therefore can evaluate the ability to match data over a range of

network sizes. The weight $\frac{N_i}{\sum_m (x_{e,i}^{\text{data}}(t_m))^2}$, the inverted mean squared of the data for all

timepoints, makes the measure equivalently sensitive to relative errors in any species regardless of whether the species has high or low concentration. Species MRE is a preferred choice in this work, as it specifies the maximum distance between the simulated and observed trajectories for all species.

If the SSE objective function has multiple minima, different sets of parameters may match the same set of data equally well. Thus we also used maximum and median PPE (parameter percentage error) as additional metrics to assess a parameter estimation method, evaluating whether the underlying parameters were indeed recovered. This is only feasible for simulated test cases, where the parameter values are known.

3.3 Alternative objective function

Inspired by primal-dual transformations from the field of linear programming, we construct an alternative parameter estimation problem that resembles a “dual” of the conventional problem. The standard “primal” formulation of the problem is to optimize

the agreement between model concentrations and experimental concentrations, subject to the constraint that the model concentrations satisfy the ODEs (*i.e.*, that the model concentrations are taken from a time-evolved trajectory of the ODEs). For the “dual” problem, we instead seek to minimize the violation of the ODEs (*i.e.*, the amount by which the right hand side differs from the left hand side of the ODE), subject to the constraint that the model concentrations exactly match the experimentally observed concentrations. In the dual approach, rather than solving the ODEs, we construct piecewise lookup-tables of model behavior, that violate the ODEs but match the observed concentrations; then we minimize the disagreement between the piecewise (interpolated) derivatives and the ODE reactions of production and consumption. We propose no analogous duality theorem for this primal-dual transformation, but we merely observe that a correct solution to the dual problem would also solve the primal problem.

Error terms of dual objective function

The error terms of our dual objective function, $\varepsilon_{e,i,j}$, minimize the disagreement between the right hand sides of the ODEs (which we denote f_i^{ODE} , see Equation 3.1) and the species derivatives (computed using the species derivatives interpolated from the observed data):

$$\varepsilon_{e,i,j} = \left| f_i^{ODE} \left(\frac{\mathbf{r}}{\mathbf{k}} \right) - \left(\frac{\hat{d}}{dt} x_{e,i}^{data} \right) \Bigg|_{t=t_j}^{spline}, \quad (3.6)$$

indexed over experiments e , species i , and timepoints t_j . $x_{e,i}^{data}$ are the time-series observations of species i in experiment e . The $\varepsilon_{e,i,j}$ terms are similar to the terms of other spline-based collocation methods, but we remark that each $\varepsilon_{e,i,j}$ is defined in terms of a small subset of the parameters $\frac{\mathbf{r}}{\mathbf{k}}$, while each term of a “primal” SSE objective utilizes all parameters via simulation.

The interpolated derivative $\hat{\frac{d}{dt}}$ in Equation 3.6 is computed using clamped cubic splines. Clamped spline interpolation approximates the first derivatives using three data points and two endpoint derivatives (Tewarson, 1980). End-point derivatives make the computation of the spline unique. Figure 3.1 illustrates the derivative for species x_i at timepoint t_j , approximated (dashed arrow) using a clamped cubic spline based on observed data for t_{j-1} , t_j and t_{j+1} ; and endpoint derivatives from the ODEs at timepoints t_{j-1} and t_{j+1} . We estimated the endpoint derivatives by computing $f_i^{ODE}(\mathbf{r}^k)|_{t=t_{j-1}}^e$ and $f_i^{ODE}(\mathbf{r}^k)|_{t=t_{j+1}}^e$, the right hand side of the ODE for species i , experiment e at timepoint t_{j-1} and t_{j+1} , respectively. Other spline methods could also be used to compute the approximate derivatives.

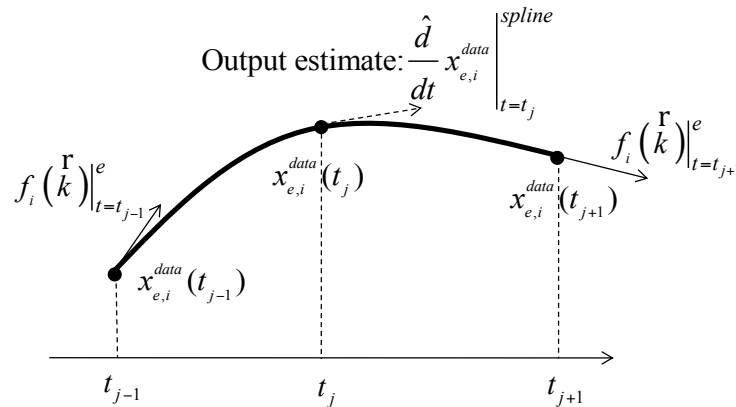


Figure 3.1 – Illustration of computing the approximate derivative using clamped spline interpolation

Product of functions

Among different schemes for combining error functions into an objective (e.g. sum of squares), we chose multiplication:

$$\min_k \text{POF} = \min_k \prod_{e \in \text{Experiments}} \prod_{i \in \text{Species}} \prod_{j \in \text{Timepoints}} \mathcal{E}_{e,i,j} \quad (3.7)$$

The product of functions (POF) is a decomposable expression that will later facilitate the use of belief propagation for probabilistic inference on a factor graph. By inspection, the POF is minimized when individual error terms $\varepsilon_{e,i,j}$ are minimized. Assuming the network is low-degree, each $\varepsilon_{e,i,j}$ is a low-dimensional term involving a small subset of the rate parameters \mathbf{k} . The $\varepsilon_{e,i,j}$ error terms cannot be optimized as independent problems because the subsets of \mathbf{k} are not mutually exclusive. However, the low-dimensionality of $\varepsilon_{e,i,j}$ means we can pre-compute solutions for each $\varepsilon_{e,i,j}$ subproblem *systematically*. We pre-compute a complete look-up table $T_{e,i,j}$ that gives the value of $\varepsilon_{e,i,j}$ for each possible (discretized) combination of the relevant \mathbf{k} parameters. To combine many low-dimensional systematic $\varepsilon_{e,i,j}$ solutions into an optimal high-dimensional parameter vector is a problem that resembles belief propagation, except with a sparsely connected, cyclic graph instead of an acyclic graph. We next describe in Section 5.4 how to compute a global estimate of \mathbf{k} as a graphical inference problem using LBP.

3.4 Loopy Belief Propagation (LBP)

We now express the POF optimization as an inference problem on a factor graph, in preparation for using a type of “belief propagation” or “message passing” algorithm to infer values of the variables that best satisfy the factorized objective function (Pearl, 1988; Yedidia, *et al.*, 2003). We construct a factor graph with nodes for the variable parameters of \mathbf{k} and the factors $\varepsilon_{e,i,j}$. The possible values of each k_i are represented as a discrete probability distribution, with uniform initial distributions (uniform *prior* probabilities). The joint probability distribution encoding the interdependence between the variable parameters is a lookup table for each factor, computing exhaustively the values of the error term $\varepsilon_{e,i,j}$ (the violation of one ODE, at one timeslice, in one experiment) for each combination of its variable parameters. This summarizes how

SPEDRE uses a factor graph to formally represent the decomposition of the global estimation problem into a network of sub-problems. Because the factor graph we define would not be acyclic, standard belief propagation (Pearl, 1988) does not apply. Finally we employ a message passing scheme (Koh, *et al.*, 2007; Murphy, *et al.*, 1999) that has been empirically successful in computing approximate MAP solutions on graphs with cycles (McEliece, *et al.*, 1998).

Factor graph

A factor graph is a bipartite graph with factor nodes $\varepsilon_{e,i,j}$ (for each experiment e , ODE i , and timepoint t_j) and variable parameter nodes k_i (for the members of $\overset{1}{k}$). We connect a factor node $\varepsilon_{e,i,j}$ to a parameter node k_i if and only if k_i appears in the equation for $\varepsilon_{e,i,j}$.

For each factor node, a factor graph has a joint table (or joint probability distribution) to describe the probability of each combination of values for the adjacent variable nodes. We compute a constant look-up table $T_{e,i,j}$, based on the error term $\varepsilon_{e,i,j}$, for the joint probability of each combination of the adjacent variable parameters. (Section 5.2 describes how errors are converted into probabilities.) Note that $\varepsilon_{e,i,j}$ represents the discrepancy between the right hand side of the i -th ODE (computed using the variable parameters) and the left hand side of the ODE (computed from spline-based interpolation of the data for experiment e , species i , and timepoint t_j). Each factor node thus serves to enforce the equality of one ODE at one timeslice and one experiment. An example factor graph corresponding to the 2-species $A \rightleftharpoons B$ system is shown in Figure 3.2 with variable nodes (rate parameters) represented by circles, and factor nodes ($\varepsilon_{e,i,j}$) by rectangles.

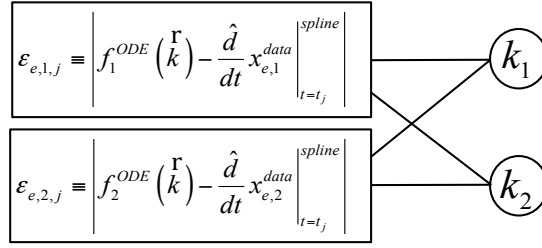


Figure 3.2 – A partial factor graph of the example 2-species system, shown for one timepoint t_j and one experiment e .

The complete factor graph would include factor nodes for every timepoint and every experimental treatment, each connected to the k_1 and k_2 variable nodes.

Discretization and Joint Probability Tables

Each variable node k_i is associated with a 1-dimensional discrete probability distribution, which represents the current belief about the likeliness of that value being in the optimal parameter vector. In theory, variable parameters are real numbers, but to permit us to evaluate combinations “systematically,” we discretize the domain of each parameter into a finite number of sub-intervals, or bins, and we represent each bin by its midpoint. Coarser intervals (larger bins) will yield faster runtime at the expense of accuracy. At the start of the algorithm, the 1-dimensional discrete probability distribution for each variable parameter is uniform, representing lack of prior knowledge about the value of that parameter. During the process of belief propagation, the discrete probability distributions will be updated by a message passing algorithm, until convergence or until an iteration limit.

If factor node $\varepsilon_{e,i,j}$ has degree d , then the joint table $T_{e,i,j}$ is a d -dimensional table, and each dimension is discretized with the same binning as the variable parameters of the d adjacent variable nodes (Figure 3.3). To convert the error terms $\varepsilon_{e,i,j}$ into probabilities, we use a Boltzmann-like exponential weighting: $p(f) = C \times \exp(-\varepsilon_{e,i,j})$. This makes large violations exponentially unlikely, and C is a normalization constant to make $p(f)$ a valid

probability distribution, *i.e.* all entries in the discrete joint table sum up to 1. (Alternative methods of representing a systematic solution of $\varepsilon_{e,i,j}$ would also have been possible.)

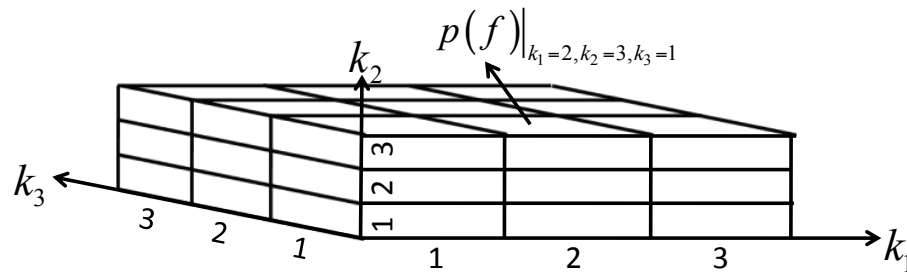


Figure 3.3 – Illustration of a joint probability table of 3 dimensions, corresponding to rate constants k_1 , k_2 and k_3 . Each dimension of the look-up table corresponds to one associated variable parameter (variable node in the factor graph), binned into 3 possible values. The joint probability computed for each cell of the table (e.g., $p(f)|_{k_1=2, k_2=3, k_3=1}$ for the cell with $k_1=2^{\text{nd}}$ bin, $k_2=3^{\text{rd}}$ bin, $k_3=1^{\text{st}}$ bin) is obtained by converting the $\varepsilon_{e,i,j}$ error term into a probability, via exponential weighting and normalization.

Note that minimizing the error means maximizing the probability. These probability distributions do not change during the course of belief propagation and can be pre-computed. The error term $\varepsilon_{e,i,j}$ must be computed for every possible discrete combination of the relevant parameters, using the midpoint of each parameter bin, and the errors can then be converted to probabilities to fill in the joint probability table $T_{e,i,j}$. The optimal combination of parameters for each $\varepsilon_{e,i,j}$ sub-problem can be found trivially by scanning the $T_{e,i,j}$ table.

Due to the discretization required by this method, the estimated value of each parameter is a range rather than a single value. Although discretization sacrifices some accuracy (analogous to round-off error), we choose the variable parameters to be discretized, sometimes quite coarsely, because the output of such a method might be ideal input for a local search method, such as Levenberg-Marquardt or Steepest Descent, to refine afterwards, using a more precise simulation-based objective function.

Loopy Belief Propagation

Belief propagation can be described informally as two types of message passing: variable nodes X pass messages (1-dimensional probability distributions, $\mu_{X \rightarrow f}$) to

adjacent factor nodes f to communicate what the variable node believes to be the value of its variable. Factor nodes f in turn pass a message (1-dimensional probability distribution, $\mu_{f \rightarrow X}$) to adjacent variable nodes X communicating what they believe the variable values to be. Each message from a factor causes the variable nodes to update their probability distributions, and that update also alters the later messages sent out by the variable nodes. In acyclic graphs, the message passing algorithm yields a provably exact, optimal MAP solution for the variables, efficiently. (Murphy, *et al.*, 1999) describe the LBP algorithm, extending the message passing framework to achieve good heuristic approximations for cyclic graphs. We use a variant of the LBP message-passing algorithm detailed in (Koh, *et al.*, 2007), summarized in Box1 as “SPEDRE-base.”

In a discrete joint distribution g with dimensions X_1, X_2, \dots, X_m , we define the maximization over a dimension X_i as follows:

$$\begin{aligned} \max_{\sim X_i} \{g(x_1, x_2, \dots, x_m)\} = \\ \max_{x_1 \in X_1} \left\{ \dots \left\{ \max_{x_{i-1} \in X_{i-1}} \left\{ \max_{x_{i+1} \in X_{i+1}} \dots \left\{ \max_{x_m \in X_m} g(x_1, x_2, \dots, x_m) \right\} \right\} \right\} \right\} \end{aligned} \quad (3.8)$$

where $\sim X_i$ denotes the set of all dimensions in g except X_i .

A. Initialization:

A.1. Compute lookup joint tables, $p(f)$, for each factor node

A.2. Set all variable nodes to uniform distribution

B. Propagation: repeat until convergence

B.1. For each factor node f

B.1.1. For each variable node $X \in N(f)$

B.1.1.1. Collect $\mu_{X_i \rightarrow f}$: the message from variable node $X_i \in N(f) \setminus \{X\}$ to f , which is $p(X_i)$, the current probability distribution of X_i

B.1.1.2. Compute $\mu_{f \rightarrow X} = \max_{\sim X} \left\{ p(f) \cdot \sum_f \log(\mu_{X_i \rightarrow f}) \right\}$

B.1.1.3. Send $\mu_{f \rightarrow X}$ to the message history of X

B.2. For each variable node X

B.2.1. Update the distribution of X to $p(X) \cdot \sum_f \log(\mu_{f \rightarrow X})$, where $\mu_{X_i \rightarrow f}$ are stored in the

Box 3.1 – SPEDRE-base algorithm for computing the MAP estimates on a factor graph.

$N(\text{node})$ is the set of neighbors adjacent to node. Steps B.1.1.2 and B.2.1 include a logarithm operation as a heuristic to avoid rounding off small numbers to zero. Because normalizing the messages or probability distributions does not affect the final MAP results (Yedidia, et al., 2003), we also perform normalization after the computation of step B.1.1.2 and B.2.1 so that the messages and beliefs are always valid probability distributions at every iteration. The messages history serves as a buffer for incoming messages, and the algorithm makes implicit use of the message history during steps B.1.1.2 and B.2.1. Input and output for the algorithm is illustrated in Section 5.5.

Convergence in step B occurs when no normalized message in the current iteration differs by more than a tolerance value from the corresponding message in the previous iteration. As the LBP algorithm is not guaranteed to converge, and in some cases might oscillate (Murphy, et al., 1999), we impose an additional criterion to limit the total number of iterations.

Asymptotic Analysis of the Modified LBP (SPEDRE-base) Algorithm

To determine the run time for step A in Box 5.1, we need to find the size of each lookup table and the number of lookup tables that need to be computed. Each dimension of the joint table corresponds to one variable node, which is one reaction in the corresponding ODE. Hence the number of dimensions of the joint table, which is the

degree of the factor graph, is proportional to the number of reactions in the ODE. The size of a joint table is $\mathcal{O}(\#bins^{degree})$. The factor graph defines one factor node for each ODE, for every experiment and at every timepoint excluding the two end timepoints. Therefore, the number of joint tables is the product of the number of ODEs (or species), experiments, and timepoints ($=\#species \times \#experiments \times \#timepoints$). Therefore, the required time for step A is:

$$\mathcal{O}(\#species \times \#experiments \times \#timepoints \times degree \times \#bins^{degree}) \quad (3.9)$$

From step B.1 in Box 5.1, for every iteration, each factor node iterates through each of the neighboring variable nodes and performs multiplication. This is equivalent to the multiplication operation between a joint tables and a one-dimensional discrete distribution, which takes the run time proportional to the size of the joint table, or $\mathcal{O}(\#bins^{degree})$. Since there are $degree$ variables connected to the factor node, the computation requires $\mathcal{O}(degree \times \#bins^{degree})$ operations. Thus the time required for step B.1 is $\mathcal{O}(\#species \times \#experiments \times \#timepoints \times degree \times \#bins^{degree})$. From step B.2 in Box 5.1, for every iteration, each variable node needs to compute its new distribution based on the messages from the factor nodes. As there are $\#rates$ variable nodes, the maximum the number of computed messages is $\#species \times \#experiments \times \#timepoints$ and each message has size $\#bins$, so the time required for step B.2 is:

$$\mathcal{O}(\#species \times \#experiments \times \#timepoints \times \#rates \times \#bins) \quad (3.10)$$

To run on all the factor nodes for $\#iterations$ iterations, the time required for step B is:

$$\begin{aligned} &\mathcal{O}(\#iterations \times \#species \times \#experiments \times \#timepoints \times (\#rates \times \#bins \\ &\quad + degree \times \#bins^{degree})) \end{aligned} \quad (3.11)$$

Since the run time for step B.1 and B.2 dominates that of step A and step C, the total time complexity of the LBP algorithm (SPEDRE-base) is:

$$\mathcal{O}(\#iterations \times \#species \times \#experiments \times \#timepoints \times (\#rates \times \#bins + degree \times \#bins^{degree})) \quad (3.12)$$

The time complexity scales exponentially with the factor graph degree, which is defined as the maximum number of variable nodes adjacent to any factor node, or the maximum number of unknown rate parameters appearing in any ODE. For a factor graph with bounded degree, the method scales polynomially with respect to the number of species, timepoints and discrete bins. This means the method scales very well on biological pathways with a small bounded number of reactions per species. Our asymptotic runtime compares favorably with conventional (“primal”) methods, because primal methods search for full-length parameter vectors in a space that grows exponentially with the number of parameters. Although primal methods with heuristic sampling do not have to cover the entire parameter space, they must maintain some coverage of the major “valleys” of the objective function. If the number of valleys and inflection points grows with the size of the parameter space, then primal methods will perform poorly (accuracy versus runtime) on large networks.

3.5 Web server implementation

Input

SPEDRE requires two main inputs from users: the connectivity of the network, and the concentrations of the molecular species. The connectivity must be specified as an XML file in COPASI_ML format (Hoops, *et al.*, 2006), which can be obtained from SBML format using a link to the conversion service in CopasiWeb (Dada and Mendes, 2009). The concentrations of the molecular species are specified in a comma separated value (CSV) file, and would typically contain time series measurement from western

blots or from SILAC proteomics (Zhang and Neubert, 2009). Using the submission form of SPEDRE, users can also customize the execution of SPEDRE. The web server homepage provides descriptions and illustrations for many sample pathways, and include a set of automatically constructed networks (circular or tree) with different sizes and published biological pathways (Akt canonical pathway (Hatakeyama, *et al.*, 2003), MAPK pathway (Huang and Ferrell, 1996) and Actin Filament Assembly-Disassembly pathway (Berro, *et al.*, 2010)).

SPEDRE allows advanced users to customize how the optimizer executes based on specific needs of the rate constant estimation problem. The universal discretization scheme for all the rate constants can be specified by setting three values: lower bound, upper bound and number of discrete bins. The individual rate constant can override its upper bound and lower bound if these are specified in the network connectivity input file. The binning scheme can be set to linear or logarithmic scaling. The maximum number of iterations allows users to limit the run time of SPEDRE, which is often a trade-off to the accuracy of returned results. The maximum number of iteration can be set to 0 if users wish to perform a standalone local search. The anticipated error rate allows users to add Gaussian noise to the provided observed data. The number of samples taken per voxel is used in the rate constant space discretization operation in SPEDRE where each voxel will be represented by the specified number of samples.

For every reaction in the pathway model, SPEDRE requires a predefined reaction type, as defined by the "rate law" value when the model is created using Copasi software (Hoops, *et al.*, 2006). Through the conversion service provided at the CopasiWeb service (Dada and Mendes, 2009), the reaction types in the output file are typically assigned a different name, which requires users to change name for these the reaction types (or rate laws) manually. Although more reaction types can be supported in the future, SPEDRE is

currently restricted to the following sets of reaction types: “Mass action (irreversible)”, “Michaelis-menten catalysis” and “Enzyme simple” (reaction rate \times enzyme \times substrate).

SPEDRE accepts data file described in comma separated value (TXT or CSV format). The content format is similar to a time-course simulation output from the Copasi software (Hoops, *et al.*, 2006), where first line specifies the headers (timepoints and species names) and first column specifies time values. When certain data point is invalid, the timepoint involved will be removed from all species before performing rate constant estimation as per normal.

Processing method

The SPEDRE web server estimates rate constants using a web server implementation of SPEDRE. Although there are many computational methods available for parameter estimation (Funahashi, *et al.*, 2003), as reviewed in (Hoops, *et al.*, 2006; Moles, *et al.*, 2003; Schmidt and Jirstrand, 2006) and (Rodriguez-Fernandez, *et al.*, 2006), we are not aware of any other web servers, besides CopasiWeb (Dada and Mendes, 2009) and SPEDRE (available at <http://webbppe.nus.edu.sg:8080/opal2/SPEDRE>).

Parameter estimation in biological networks is challenging because the parameters are shared between different ODEs, which makes them impossible to estimate individually. Even if each parameter can take on only a fixed number of possible values, the number of possible combinations of these parameter values becomes astronomical, growing exponentially with respect to the number of reactions. SPEDRE exploits the sparsity of the network to divide up the problem, and it performs a systematic search with approximate accuracy by using a probabilistic inference technique called Loopy Belief Propagation (Murphy, *et al.*, 1999). The pipeline for executing the rate constant estimation task is illustrated in Figure 3.4.

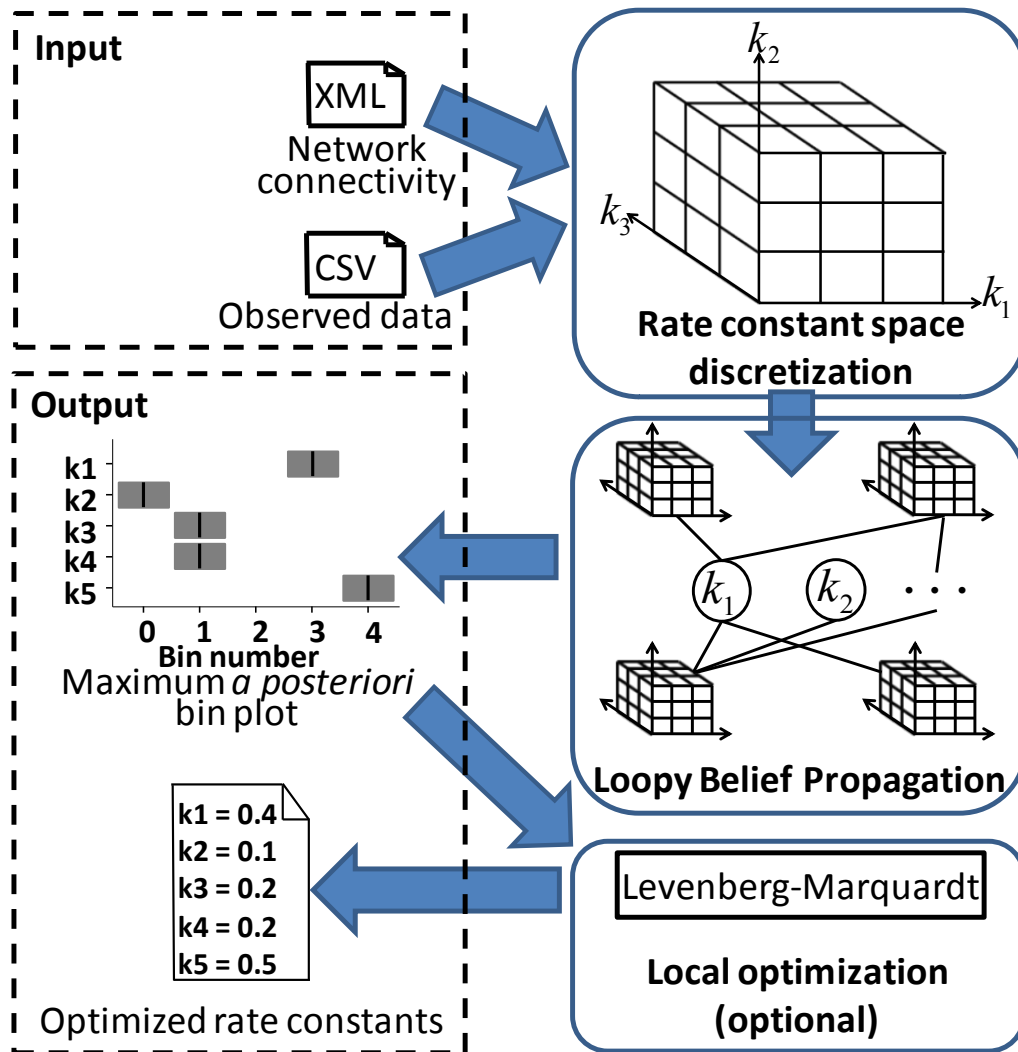


Figure 3.4 – Processing pipeline for SPEDRE

From Figure 3.4, the pipeline for rate constant estimation in SPEDRE can be described in five components: input, rate constant space discretization, loopy belief propagation, local optimization and output. Many options are available for users to customize how SPEDRE executes, including the number of bins per rate constant in computing the joint table and the number of iterations of belief propagation. Taking network connectivity and observed data from users, rate constant space discretization transforms the continuous range of rate constants into discrete bins, with the coarseness defined by users. The discrete rate constant space allows SPEDRE to perform loopy belief propagation, which is an iterative procedure that will terminate by convergence or when the specified maximum number of iterations is reached. Upon termination, a bin

plot is displayed to the users, where optionally the bins' midpoint will be used as initial guess for local optimization. Full methods are provided with the SPEDRE-base algorithm in Section 5.4.

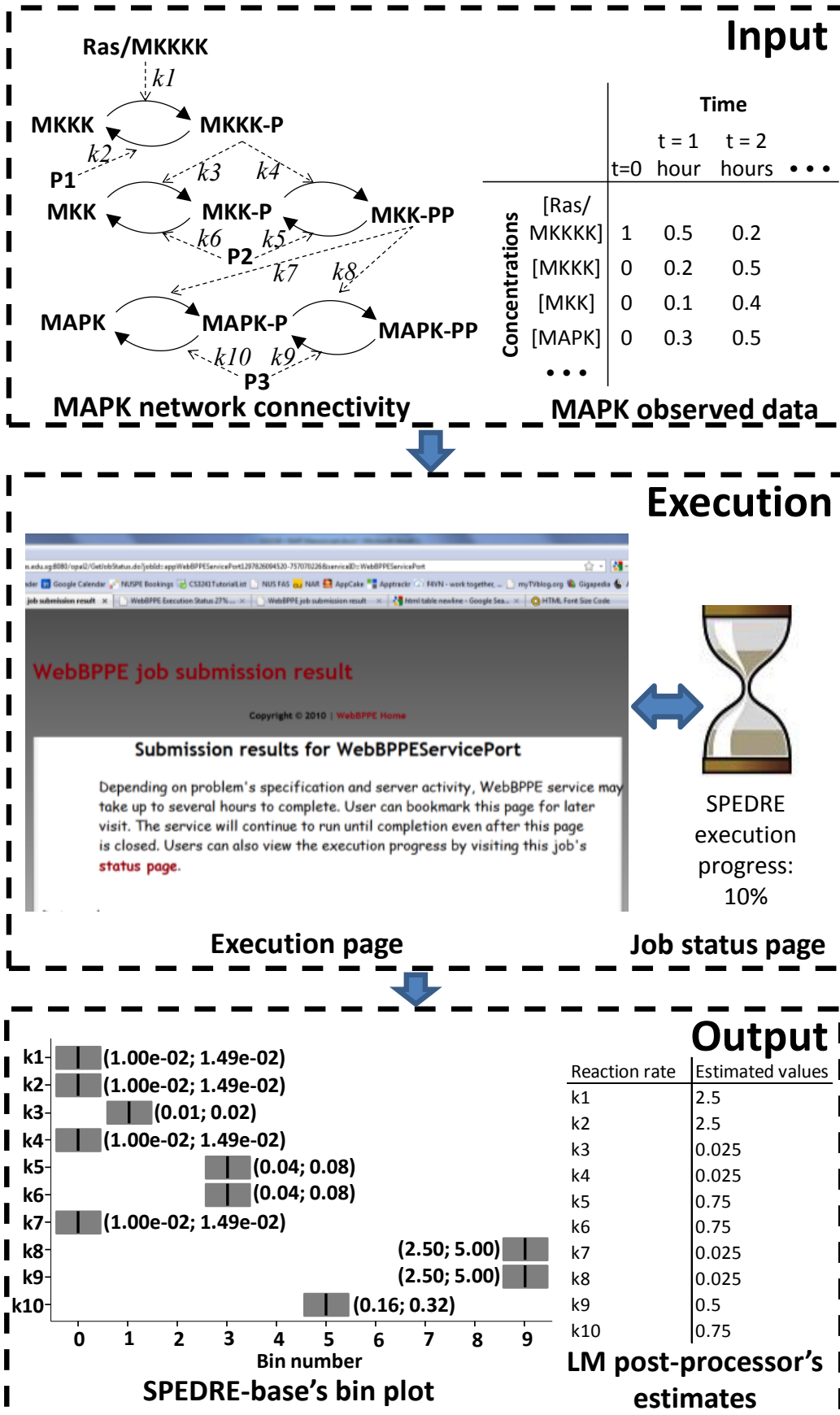
The asymptotic analysis of the SPEDRE algorithm reveals interesting properties of the method, in which the time complexity scales exponentially with the network degree but polynomially with the number of species, time points and discrete bins. Correspondingly, this means the method scales well on biological pathways with a bounded number of reactions per species. Dense networks with hub-like species have high network degree and thus are unsuitable for SPEDRE-base algorithm, and SPEDRE handles these cases by running the Levenberg-Marquardt algorithm (Marquardt, 1963).

The SPEDRE algorithm was implemented using C++ language with an interface with Copasi (version 4.6, build 32) (Hoops, *et al.*, 2006). SPEDRE web server was implemented using the Opal toolkit, as introduced in (Ren, *et al.*, 2010), among other tools. To display the customizable bin plot of SPEDRE results, Google Chart API (Google Inc.) was used.

Ouput

An example execution based on the MAPK cascade is shown in Figure 3.5. Using the web interface, users can submit the input files following the specified format, and SPEDRE performs the computation task while simultaneously displaying the execution page. Different execution specifications may result in very different run time, thus some may require several hours to complete. The users can therefore bookmark the location of the output page for a later visit. A status page is linked to the execution page and shows the percentage of the overall task that has been completed. Users are advised to refer to the asymptotic analysis of SPEDRE algorithm to adjust the SPEDRE execution configuration for dense networks.

Upon completion, SPEDRE returns an estimated range for each rate constant, in the form of a bin plot, as shown in Figure 3.5. A bin plot is a visual representation of the resulting voxel in high dimensional space, which gives users an impression of the exponential number of possible combinations of rate constants, even in a coarsely discretized search space. Each bin indicates a range in which the estimated reaction rate lies, and the mid-point can be taken as the estimated value. Further search within this range can be performed by any method, for example by using the midpoint of the output range as an initial guess for a point-based method. We follow SPEDRE-base with the Levenberg-Marquardt (LM) algorithm of local optimization (Marquardt, 1963), which is available through a seamless interface with Copasi, because hybrid global-local methods have been an effective strategy for many complex optimization problems (Ashyraliyev, *et al.*, 2009; Nim, *et al.*, 2010; Rodriguez-Fernandez, *et al.*, 2006).



The bin plot shown in Figure 3.5 was generated using the Google Chart API (Google Inc.), which imposed certain constraints, including the maximum URL length of 2,048 characters (for plot formatting) and maximum plot size of 300,000 pixels. Users may encounter a cluttered plot for a very large network (>30 rate constants). As the API is actively developed with large user base across the industry, this current limit can be overcome with new updates of the API.

3.6 Benchmark experiment setup

We propose that the SPEDRE-base algorithm should be followed by a local search method such as LM, because a hybrid approach can correct some of the fine-grained inaccuracies created by the discretization and by the numerically approximate derivatives. SPEDRE-base is written in C++, the same language as the Copasi parameter estimation tools (Hoops, *et al.*, 2006). A wide variety of parameter estimation algorithms assert claims of supremacy, and algorithms in the “evolutionary strategies” family are particularly well-reviewed (Moles, *et al.*, 2003). For a fair comparison, we chose a variety of standard methods:

- Local search: Steepest Descent (SD), Levenberg-Marquardt (LM)
- Global search: SPEDRE-base, Genetic Algorithm (GA), Evolution Strategy using Stochastic Ranking (SRES), Particle Swarm Optimization (PSO)

Four forms of global and two forms of local optimization produce 8 hybrid methods: SPEDRE, SRES_LM, PSO_LM, GA_LM, SPEDRE-base_SD, SRES_SD, PSO_SD and GA_SD. Note that hybrid methods GA_LM and PSO_LM were previously proposed by Katare *et al.* (Katare, 2004). Rodriguez-Fernandez *et al.* also proposed the hybrid of SRES with a local optimizer (Rodriguez-Fernandez, *et al.*, 2006). The implementations of the comparison algorithms were used through the Copasi software

package (version 4.4, build 26). Each parameter estimation method was run with custom configuration (*e.g.* number of generations, number of iterations, *etc.*) such that all methods take a similar amount of time to complete. However, this constraint may not always hold (see Table 5.1) as local search methods and GA can converge very quickly, regardless of user-defined iteration limits. Copasi (.CPS) source files are available at the SPEDRE homepage, describing the model parameters and configuration for each parameter estimation method on each test case (including the ring networks, artificial networks and the Akt model). Experiments were performed on an Intel® Core™ i7 2.8GHz CPU and 4GB memory workstation running Windows® XP™.

3.7 Results

Initial tests were designed to confirm that the SPEDRE-base method can solve simple parameter estimation problems. We also monitored performance as a function of network size and timepoint spacing, in order to probe two sources of potential error in the SPEDRE-base method: spline accuracy, and the POF objective function. Simple tests were designed with ring-shaped networks (Figure 3.6A) and with nominal parameters randomly chosen to be at exact mid-points of the parameter discretization bins. Simulated data were generated with random initial concentrations, using the nominal rate parameters. For each run of SPEDRE-base, we monitored the objective

$$\text{Normalized log(POF)} = \frac{\log(\text{POF})}{N_t * (N_s - 2)}, \quad (3.13)$$

normalized with respect to the number of factors in the product of Equation 3.13. The objective declined when the number of timepoints increased (Figure 3.6B), indicating as expected that SPEDRE gives better estimates of the parameters when timepoints are densely sampled.

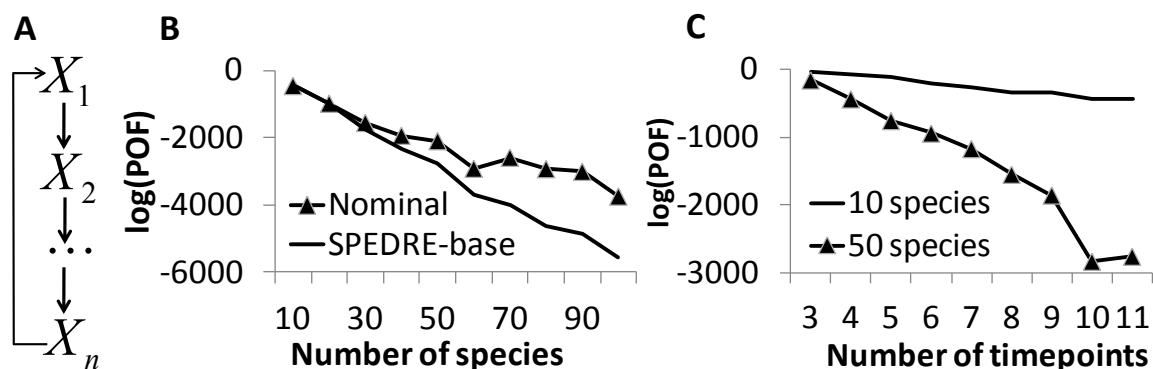


Figure 3.6 – Performance of SPEDRE on a series of ring networks. (A) Ring network diagram; (B) normalized log(POF) with respect to the number of timepoints on different network sizes; (C) normalized log(POF) of LBP predicted rate constants, versus the normalized log(POF) of nominal (“correct”) rate constants on circular networks of 10 to 100 species with 11 timepoints. (Total simulation duration was 4s, with 0.4s for each time step). Each rate constant was discretized into 10 equidistant bins from 0.05 to 1.05, with the nominal rate constants selected from among the bin midpoints. Dataset can be found at <http://webbpe.nus.edu.sg:8080/opal2/SPEDRE>.

Next we compared the normalized log(POF) value between the results of SPEDRE-base, and the nominal (“correct”) rate constants, using 10 time steps (*i.e.* 11 timepoints) for each test. Figure 3.5C shows that the POF scores of the exact nominal parameters were higher than the POF scores of the parameters found by SPEDRE-base, for all networks of significant size. Because SPEDRE-base found parameters with better scores than the “correct” parameters, we infer that the POF objective is an imperfect score of parameter accuracy.

Scalability with artificial networks

The complete SPEDRE method consists of SPEDRE-base (Sections 3.3-3.4) followed by LM to refine the discretized results from SPEDRE-base. We compared the performance of the complete SPEDRE method against a selection of popular local, global, and hybrid methods, on parameter estimation problems from low-degree networks. Random networks of increasing size (from 30 to 150 species) were constructed with low degree (two-thirds of the reactions involving 3 species, and one-third involving 2 species), to generate parameter estimation problems with increasing scale. We tested 14 parameter estimation methods including SPEDRE-base, LM (local), SD (local), SRES (global), PSO (global) and GA (global), plus hybrid global-local combinations of these

methods (*e.g.* SRES_LM denotes the global method SRES plus the local method LM). Runtime and multiple error scores were measured as a large-scale screen.

We compared the performance of all 14 parameter estimation methods on a series of randomly constructed low-degreed networks, including run time, species maximum relative error (MRE), median and maximum parameter percentage error (PPE). The networks vary in size from 30 species to 150 species. Data sets were obtained by simulating the networks with nominal reaction rates, to which 20% Gaussian noise or no noise was added to generate simulated observations. A sample network of size 30 is shown in Figure 3.7. Figure 3.8 showed the performance of all standalone and hybrid methods on an artificial network with 130 species and 130 reaction rates (each bar showing the average with error bar indicating standard deviation from three tests with different parameter sets using the same network topology), where complete comparison results on different network sizes are shown in Table 3.1. To score the quality of the parameter estimation results, we used an additional metric called weighted SSE, defined as:

$$\sum_{e \in \text{Experiments}} \sum_{i \in \text{Species}} \sqrt{\frac{N_t}{\sum_{j \in \text{Timepoints}} (x_{e,i}^{data}(t_j))^2}} \sum_{j \in \text{Timepoints}} \left(x_{e,i}^{data}(t_j) - x_{e,i}^{sim}(t_j, \mathbf{k}) \right)^2, \quad (3.14)$$

which follows the default SSE objective function used in the Copasi software package. All metrics were normalized such that the highest score for any method is 1.0. Note that low runtime indicates good scalability, and low species MRE, median and maximum PPE indicate good accuracy.

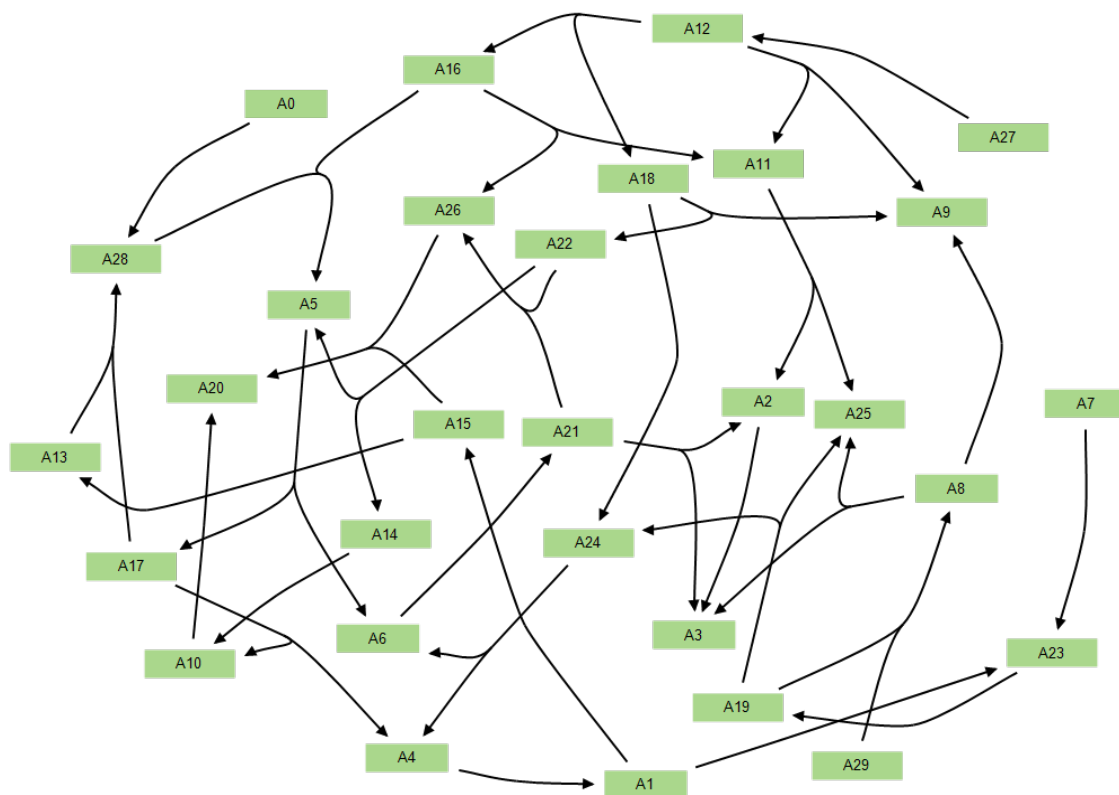


Figure 3.7 – Network diagram for a random artificial low-degree network of size $N=30$, with 30 species and 30 reaction rates.

Random reactions (with two-thirds of the reactions involving 3 species, and one-third involving 2 species) were added between the species such that the maximum degree for each node is three.

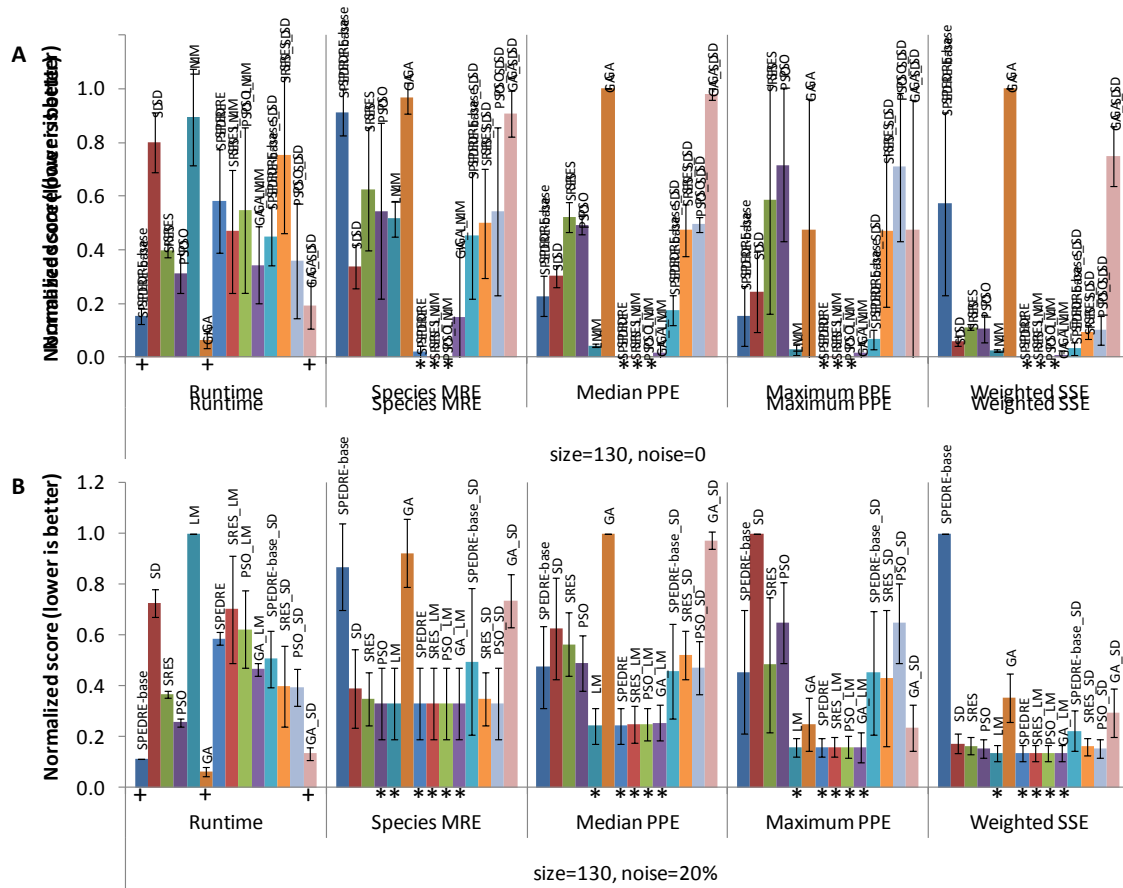


Figure 3.8 – Comparison of standalone and hybrid methods on artificial network containing 130 species and 130 reaction rates.

Test cases uses (A) noiseless and (B) 20%-noise data. Asterisks (*) denote the top methods with respect to accuracy. Pluses (+) denote the top methods with respect to runtime. When several methods have the same score, it often means these methods reached the same local minimum. Multiple scoring schemes (species MRE, PPE and weighted SSE) were used to compare the parameter estimation quality, but we advocate species MRE, as it specifies the maximum distance between the simulated and observed trajectories for all species.

A

		Noise = 0													
		#species	30	40	50	60	70	80	90	100	110	120	130	140	150
		#rates	30	40	50	60	70	80	90	100	110	120	130	140	150
Run time (s)	SPEDRE-base	179.00	371.00	403.00	438.00	445.00	820.00	1074.00	967.00	1296.00	1361.00	1313.00	2030.00	1523.00	
	SD	45.85	81.76	11.68	314.40	392.83	191.30	1620.82	2170.96	3419.98	2347.64	7703.70	11940.30	933.06	
	SRES	58.80	92.84	156.70	270.27	316.99	611.26	1021.93	1160.46	1480.59	2598.70	3479.96	5057.88	5062.28	
	PSO	41.12	71.39	113.57	178.25	212.99	484.20	656.73	961.04	983.49	1027.77	3261.39	2871.87	3390.76	
	LM	6.08	11.82	26.49	43.66	54.85	264.25	361.56	2378.30	742.78	7869.39	8861.93	7311.95	13759.10	
	GA	11.59	16.22	31.59	46.88	54.13	116.08	171.21	177.17	265.93	519.84	365.74	369.99	942.00	
	SPEDRE	184.90	383.50	428.66	482.30	497.90	1094.14	1341.31	2378.14	1837.57	2846.32	3382.29	3922.84	4590.40	
	SRES_LM	65.63	104.22	188.65	314.28	361.84	844.50	1298.83	1721.88	2237.46	6142.50	5363.98	6954.63	6959.03	
	PSO_LM	46.71	84.24	140.32	223.41	258.93	719.27	924.70	1494.72	1495.69	2405.80	5268.79	5170.96	10030.72	
	GA_LM	18.30	27.19	59.00	114.24	106.81	375.81	480.83	1547.64	774.23	1745.40	4726.79	3056.65	3935.97	
	SPEDRE-base_SD	199.22	376.69	491.70	593.56	661.64	1332.56	1870.68	1370.84	2936.21	2794.18	6406.89	5034.06	3277.99	
	SRES_SD	78.80	98.90	163.54	432.76	504.49	1053.32	1853.88	2166.70	3110.46	5773.13	3827.50	10126.94	12500.08	
	PSO_SD	57.28	104.94	140.76	353.53	410.83	846.24	1538.01	2156.44	2538.13	3021.81	4624.04	7522.93	5931.39	
	GA_SD	15.91	47.11	125.78	109.57	76.10	283.73	200.20	262.58	414.52	832.31	2470.91	606.38	1870.73	
Species MRE	SPEDRE-base	1.55	0.14	0.54	0.51	1.07	1.73	3.08	3.51	3.00	3.28	5.59	1.82	3.51	
	SD	1.90	0.01	2.50	0.63	0.18	1.77	1.85	1.44	3.95	3.74	1.43	1.51	4.32	
	SRES	0.14	0.07	0.43	0.07	0.21	0.38	1.92	1.82	2.33	1.75	2.03	1.59	1.47	
	PSO	0.21	0.00	0.13	0.04	0.10	0.10	0.16	1.37	1.39	2.28	1.66	1.34	1.97	
	LM	0.00	0.00	0.00	0.00	0.00	0.00	0.00	2.18	0.00	2.23	2.48	2.39	2.19	
	GA	0.32	0.06	0.35	2.01	1.24	0.69	1.93	3.34	2.38	4.74	5.02	4.65	2.99	
	SPEDRE	0.00	0.00	0.00	0.00	0.00	0.00	0.00	0.13	0.00	0.00	0.00	0.00	0.12	
	SRES_LM	0.00	0.00	0.00	0.00	0.00	0.00	0.00	0.00	0.00	0.03	0.00	0.00	0.00	
	PSO_LM	0.00	0.00	0.00	0.00	0.00	0.00	0.00	0.00	0.00	0.00	0.00	0.00	0.13	
	GA_LM	0.00	0.00	0.00	0.00	0.00	0.00	0.00	0.10	0.00	0.00	2.48	0.00	0.00	
	SPEDRE-base_SD	0.09	0.09	0.17	0.06	0.08	0.21	0.18	2.27	1.60	1.53	1.01	0.78	2.27	
	SRES_SD	0.11	0.06	0.43	0.06	0.06	0.36	1.93	1.37	2.35	0.93	1.95	1.29	1.38	
	PSO_SD	0.19	0.00	0.13	0.04	0.10	0.09	0.16	1.30	1.39	1.64	1.67	1.03	1.85	
	GA_SD	0.24	0.03	0.35	0.47	1.18	0.44	1.93	3.34	2.38	4.34	5.02	4.65	2.87	
Median PPE	SPEDRE-base	27.48	9.46	14.35	11.46	16.87	14.90	13.59	24.68	23.04	20.36	14.19	12.57	18.07	
	SD	32.54	4.20	67.69	23.81	29.29	42.41	59.20	28.70	52.41	45.93	28.26	27.87	65.22	
	SRES	18.66	13.53	38.71	29.67	32.58	29.69	28.60	32.68	30.55	34.69	47.00	42.75	35.73	
	PSO	8.95	6.29	11.04	22.17	16.29	18.28	31.39	33.23	20.21	32.37	41.24	34.79	36.50	
	LM	0.00	0.00	0.00	0.00	0.00	0.00	0.00	9.46	0.00	8.54	3.66	2.94	8.00	
	GA	28.36	26.15	42.18	75.22	65.25	48.71	48.29	80.16	35.85	68.05	80.80	85.08	59.39	
	SPEDRE	0.00	0.00	0.00	0.00	0.00	0.00	0.00	1.53	0.00	0.00	0.00	0.00	1.16	
	SRES_LM	0.00	0.00	0.00	0.00	0.00	0.00	0.00	0.00	0.00	0.32	0.00	0.00	0.00	
	PSO_LM	0.00	0.00	0.00	0.00	0.00	0.00	0.00	0.00	0.00	0.00	0.00	0.00	1.23	
	GA_LM	0.00	0.00	0.00	0.00	0.00	0.00	0.00	1.20	0.00	0.00	4.11	0.00	0.00	
	SPEDRE-base_SD	15.00	8.99	20.63	7.54	12.58	11.93	11.91	25.76	20.18	19.25	9.10	11.22	17.48	
	SRES_SD	17.54	12.90	38.69	27.41	24.57	29.15	27.77	23.80	26.69	20.23	46.97	35.11	24.46	
	PSO_SD	6.82	4.04	11.07	20.53	14.76	17.35	31.07	28.79	19.64	22.92	40.59	29.54	35.21	
	GA_SD	23.91	7.17	38.74	68.82	65.22	42.51	48.29	80.16	34.93	65.84	79.98	85.08	59.17	
Maximum PPE	SPEDRE-base	237.38	471.52	872.72	94.60	519.65	3176.70	2101.73	1322.18	3436.00	1078.67	1078.67	1322.18	1322.18	
	SD	625.76	2659.10	8329.70	670.23	5888.93	20566.17	3978.75	8772.20	17238.52	2460.96	3030.34	1469.82	6602.07	
	SRES	118.88	877.92	629.13	531.54	4382.51	2381.09	1595.55	1948.94	17032.30	5740.76	4490.07	9452.44	1944.64	
	PSO	183.45	916.74	995.66	113.44	195.62	2860.01	2439.33	1443.32	5924.59	10551.76	5279.34	880.36	3382.48	
	LM	0.00	0.21	0.01	0.00	0.02	0.09	0.02	2457.33	0.01	2131.87	375.86	472.85	2341.52	
	GA	298.17	965.15	867.51	269.92	909.93	3170.23	5041.65	2926.78	9206.24	3599.76	7302.22	2269.59	9361.82	
	SPEDRE	0.00	0.21	0.01	0.00	0.02	0.09	0.02	120.54	0.01	0.02	0.00	0.02	114.07	
	SRES_LM	0.00	0.21	0.01	0.00	0.02	0.09	0.02	0.01	0.01	64.12	0.00	0.02	0.01	
	PSO_LM	0.00	0.21	0.01	0.00	0.02	0.09	0.02	0.01	0.01	0.02	0.00	0.02	168.41	
	GA_LM	0.00	0.21	0.01	0.00	0.02	0.10	0.02	104.02	0.01	0.02	369.81	0.02	0.01	
	SPEDRE-base_SD	163.46	459.39	632.60	89.58	407.41	508.05	2102.31	1330.38	3486.13	696.18	767.21	1304.98	1330.38	
	SRES_SD	110.79	877.72	629.14	527.14	3934.94	2359.20	1564.14	1262.06	16963.00	4731.55	4485.81	6973.70	1882.32	
	PSO_SD	155.06	881.96	995.78	110.93	188.06	2859.58	2439.40	1169.56	5906.41	6398.32	5271.96	841.59	3282.58	
	GA_SD	297.65	1045.57	845.51	266.91	910.23	3113.74	5041.65	2926.78	9206.24	3586.45	7262.57	2269.60	9320.24	
Weighted SSE	SPEDRE-base	23.13	5.03	18.80	3.90	36.87	26.27	29.50	480.92	40.72	65.07	71.35	62.15	495.80	
	SD	9.58	0.06	53.89	6.34	3.76	44.35	66.39	15.30	25.57	29.95	23.12	12.87	359.18	
	SRES	1.46	0.49	3.62	2.24	4.72	7.66	23.39	20.74	10.50	18.10	35.88	29.20	40.59	
	PSO	1.02	0.05	0.73	1.17	1.48	2.43	4.77	7.39	7.56	12.88	19.05	14.76	31.28	
	LM	0.00	0.00	0.00	0.00	0.00	0.00	0.00	19.83	0.00	22.31	8.07	10.51	19.25	
	GA	6.86	1.59	7.65	57.48	45.11	23.28	63.96	206.90	21.51	91.17	291.94	296.91	95.13	
	SPEDRE	0.00	0.00	0.00	0.00	0.00	0.00	0.00	0.02	0.00	0.00	0.00	0.00	0.02	
	SRES_LM	0.00	0.00	0.00	0.00	0.00	0.00	0.00	0.00	0.00	0.00	0.00	0.00	0.00	
	PSO_LM	0.00	0.00	0.00	0.00	0.00	0.00	0.00	0.00	0.00	0.00	0.00	0.00	0.05	
	GA_LM	0.00	0.00	0.00	0.00	0.00	0.00	0.00	0.02	0.00	0.00	8.05	0.00	0.00	
	SPEDRE-base_SD	2.06	2.79	4.50	0.54	1.81	2.13	3.75	32.40	13.20	14.41	2.79	3.41	35.58	
	SRES_SD	1.02	0.43	3.61	1.86	2.25	6.52	20.15	9.61	6.93	4.53	35.42	20.18	12.16	
	PSO_SD	0.84	0.02	0.69	0.91	1.03	2.24	4.58	5.81	6.63	8.86	17.40	10.58	29.05	
	GA_SD	5.81	0.18	5.04	19.74	40.63	10.10	63.96	206.67	20.32	44.23	236.46	295.48	83.22	

		Noise = 20%														
		#species	30	40	50	60	70	80	90	100	110	120	130	140	150	
		#rates	30	40	50	60	70	80	90	100	110	120	130	140	150	
Run time (s)	SPEDRE-base	218.00	337.00	394.00	476.00	623.00	854.00	663.00	978.00	1334.00	1526.00	1064.00	971.00	1131.00		
	SD	46.18	89.19	11.64	316.70	514.65	257.48	1599.03	2125.53	3167.19	3153.12	7448.58	3874.49	933.42		
	SRES	67.91	100.85	162.09	266.29	366.18	1022.04	910.20	1105.80	1420.47	2417.06	3434.50	4284.40	4967.57		
	PSO	38.16	75.86	111.68	175.06	291.10	561.95	637.14	924.54	966.24	1587.53	2420.28	2422.15	3296.85		
	LM	33.43	70.15	168.29	274.05	364.45	689.68	960.56	1165.86	2993.21	6320.72	9437.22	7686.98	13845.50		
	GA	11.01	18.17	28.41	38.95	81.31	175.38	151.01	152.66	240.05	360.74	623.43	696.54	900.67		
	SPEDRE	451.19	713.20	868.42	1093.52	1486.02	2295.08	1823.81	3370.43	4082.31	5944.94	6351.52	5904.16	7852.76		
	SRES_LM	83.07	135.02	241.65	408.60	610.45	1476.64	1444.57	2470.96	2800.64	5257.76	7769.19	8540.23	12118.42		
	PSO_LM	54.60	111.42	188.78	315.36	529.44	1138.85	1265.09	2281.20	2382.06	4418.50	6690.32	6648.70	10082.04		
	GA_LM	26.07	54.34	105.64	177.54	327.68	829.96	898.97	1094.38	1602.22	3288.61	4847.31	4999.45	7697.34		
	SPEDRE-base_SD	236.30	384.55	489.41	641.28	878.14	1149.22	1338.42	2583.02	1665.05	2164.93	4774.39	4904.55	8001.94		
	SRES_SD	88.39	144.35	171.96	430.30	645.24	1728.72	1770.72	1767.84	2682.67	4831.30	5502.14	5945.54	10262.09		
	PSO_SD	56.33	79.69	116.52	328.93	570.18	614.44	1511.03	2194.90	2206.35	4633.73	6857.10	2572.82	4480.91		
	GA_SD	27.80	64.58	51.98	160.38	119.89	279.41	877.63	179.88	447.78	1674.19	1133.25	1282.67	1931.93		
	Species MRE	SPEDRE-base	0.62	0.23	0.68	0.60	1.42	0.90	3.26	3.17	4.04	3.13	4.71	3.08	2.67	
SD		2.08	0.04	2.49	0.79	0.21	1.84	2.13	1.53	2.03	3.60	2.68	1.83	4.62		
SRES		0.25	0.09	0.15	0.14	0.21	0.50	1.85	1.58	2.99	1.78	2.12	1.66	2.01		
PSO		0.18	0.06	0.06	0.10	0.17	0.63	0.26	1.05	4.90	1.51	2.13	2.54	2.01		
LM		0.17	0.04	0.03	0.09	0.06	0.22	0.15	2.14	0.31	2.32	2.13	2.78	2.84		
GA		0.82	0.09	0.29	1.31	0.79	0.75	2.39	3.61	1.99	4.85	5.07	4.04	3.45		
SPEDRE		0.17	0.04	0.03	0.09	0.06	0.22	0.15	0.26	0.31	1.51	2.12	2.79	2.01		
SRES_LM		0.17	0.04	0.03	0.09	0.06	0.22	0.15	0.26	0.31	1.51	2.12	1.56	2.01		
PSO_LM		0.17	0.04	0.03	0.09	0.06	0.22	0.15	0.26	0.31	1.51	2.13	1.56	2.01		
GA_LM		0.17	0.04	0.03	0.09	0.06	0.22	0.15	2.15	0.31	2.31	2.13	1.56	2.01		
SPEDRE-base_SD		0.17	0.05	0.24	0.18	0.06	0.33	0.43	1.19	2.97	1.97	3.56	1.56	2.69		
SRES_SD		0.19	0.05	0.15	0.12	0.18	0.47	1.81	1.40	2.59	1.77	2.12	1.65	2.01		
PSO_SD		0.20	0.06	0.06	0.11	0.15	0.63	0.19	0.95	4.85	1.51	2.13	2.54	2.01		
GA_SD		0.34	0.05	0.24	0.30	0.77	0.68	1.97	3.61	2.00	3.98	4.29	3.89	2.93		
Median PPE		SPEDRE-base	13.41	16.81	21.63	29.40	17.12	17.94	29.75	45.31	35.82	37.16	35.55	36.36	28.97	
	SD	26.81	7.99	67.50	21.12	27.67	42.35	55.31	26.39	27.04	43.61	47.13	42.36	65.22		
	SRES	14.24	21.62	45.60	24.40	26.05	24.04	35.09	32.22	31.92	28.97	42.76	43.67	34.29		
	PSO	10.91	8.70	25.92	12.96	33.91	39.60	27.67	34.68	23.70	36.76	45.97	36.23	33.08		
	LM	4.57	7.54	6.80	5.98	5.12	7.69	6.10	13.09	6.76	23.59	19.11	22.47	22.18		
	GA	36.65	20.17	50.95	57.63	69.44	38.35	46.63	67.29	44.62	68.36	91.36	51.93	65.77		
	SPEDRE	4.56	7.58	6.74	6.37	5.12	7.69	5.78	6.90	6.56	20.67	19.04	24.43	20.74		
	SRES_LM	4.56	7.76	6.86	5.81	5.12	8.14	5.66	7.31	6.73	16.78	16.64	20.84	19.37		
	PSO_LM	4.56	7.53	6.93	5.86	5.12	7.51	5.73	6.53	6.62	17.25	18.92	21.75	21.96		
	GA_LM	4.56	7.47	6.87	6.18	5.12	7.88	5.92	11.86	6.65	22.56	19.70	21.45	20.37		
	SPEDRE-base_SD	8.44	8.90	18.90	19.52	12.85	16.33	21.96	26.43	35.39	35.03	33.54	28.40	28.99		
	SRES_SD	11.76	13.87	45.50	19.84	20.74	23.74	34.72	30.16	24.79	29.14	39.75	40.37	29.12		
	PSO_SD	9.18	8.42	25.91	8.86	28.33	40.20	24.58	30.94	22.50	35.64	46.00	36.23	32.29		
	GA_SD	28.57	11.59	49.60	44.78	69.23	35.31	42.83	67.29	44.61	66.60	89.71	51.65	65.76		
	Maximum PPE	SPEDRE-base	91.97	1614.55	446.12	94.60	3690.53	992.23	1375.99	1786.26	1078.67	3562.98	3941.98	2864.12	2325.19	
SD		614.91	2690.55	8321.16	1265.29	5918.13	20546.73	3940.45	7626.02	17028.11	2367.48	5390.70	4422.37	6602.05		
SRES		97.85	540.13	605.26	199.47	2347.42	1581.79	816.01	2747.54	14673.32	4694.30	1077.28	6786.43	2565.13		
PSO		121.47	193.26	1403.78	93.88	3378.73	4383.18	1517.32	833.99	6533.92	3055.62	2910.83	2016.52	12826.11		
LM		31.73	2018.79	1426.18	54.84	91.58	617.49	2176.05	2356.21	120.80	2507.12	1058.79	1634.69	1273.24		
GA		368.26	1175.42	877.94	110.83	2333.11	5992.86	2982.71	3866.59	558.68	3210.93	935.67	2857.30	18994.64		
SPEDRE		32.97	2031.75	1426.18	55.21	91.58	667.07	2177.95	795.87	316.41	322.57	1063.96	1639.72	964.11		
SRES_LM		33.10	2061.66	1426.18	54.83	91.58	797.79	2201.72	698.90	115.77	370.60	1083.64	970.82	1058.46		
PSO_LM		32.97	2025.21	1426.18	55.48	91.58	601.37	2251.30	761.80	99.83	1049.41	1073.30	1012.75	964.79		
GA_LM		32.91	2000.01	1426.18	54.26	91.58	674.29	2188.84	2369.24	203.50	2416.73	1175.29	866.83	1006.20		
SPEDRE-base_SD		73.69	1567.19	93.98	93.80	3094.34	975.27	808.96	1737.04	1092.61	3577.90	3940.50	2498.67	2312.60		
SRES_SD		87.34	726.95	604.68	189.53	2164.01	1581.41	740.72	2641.92	14371.91	4205.20	1083.35	5995.12	2170.82		
PSO_SD		113.66	192.93	1403.78	93.03	3275.05	4383.32	1516.37	598.21	6517.54	2847.95	2910.79	2016.52	12727.29		
GA_SD		354.57	1238.28	878.42	108.00	2333.10	5989.61	2417.63	3866.59	544.95	3208.83	858.57	2797.69	18993.98		
Weighted SSE		SPEDRE-base	8.60	4.68	16.63	18.32	36.53	16.99	51.56	577.58	60.17	1721.13	1354.80	5819.39	610.46	
	SD	9.58	1.16	54.33	8.52	5.99	47.48	62.54	27.09	9.74	172.17	289.92	234.15	512.19		
	SRES	3.33	1.64	5.49	4.72	5.41	7.98	19.22	25.43	19.86	161.01	275.56	230.12	122.01		
	PSO	1.50	1.29	1.52	2.35	5.34	24.25	8.50	21.83	11.81	159.34	264.46	222.68	104.50		
	LM	1.28	1.06	1.05	1.86	1.82	2.59	2.83	3.17	3.17	161.24	235.46	208.96	105.18		
	GA	14.66	2.34	6.92	24.72	36.26	21.44	38.21	145.10	21.83	266.69	615.43	276.80	202.57		
	SPEDRE	1.28	1.06	1.05	1.86	1.82	2.59	2.83	12.47	3.17	146.49	235.72	210.69	78.98		
	SRES_LM	1.28	1.06	1.05	1.86	1.82	2.60	2.83	12.52	3.17	146.64	235.16	200.31	78.83		
	PSO_LM	1.28	1.06	1.05	1.86	1.82	2.59	2.83	12.47	3.17	146.40	234.92	200.26	78.99		
	GA_LM	1.28	1.07	1.05	1.86	1.82	2.60	2.83	31.67	3.17	161.29	235.80	200.33	78.86		
	SPEDRE-base_SD	2.43	1.16	4.17	4.60	2.71	8.80	9.49	19.12	40.38	184.38	343.15	227.37	189.19		
	SRES_SD	2.83	1.27	5.44	3.25	4.28	7.52	18.42	23.27	12.59	158.30	270.34	224.91	106.56		
	PSO_SD	1.42	1.28	1.51	2.06	4.11	23.86	7.11	17.54	26.96	156.71	263.99	222.68	102.94		
	GA_SD	6.32	1.18	6.38	8.65	33.05	17.94	23.91	145.10	20.83	252.69	508.89	272.44	192.69		

Table 3.1 - Comparison of standalone and hybrid methods on artificial networks of size N=30 to 150. Test cases uses (A) noiseless and (B) 20%-noise dataset. Each dataset used in each test case was constructed by simulating the network using nominal reaction rates, where no noise or 20%-noise (Gaussian) was added to the data. Multiple scoring schemes (species MRE, PPE and weighted SSE) were used to compare the parameter estimation accuracy. Cells highlighted in reds have the best score among all methods being compared for each test case (i.e. column).

The speed and accuracy of stochastic global methods (e.g., SRES, PSO, GA) depend on the degree of sampling, where greater sampling gives better quality at the expense of runtime. To compare sampling methods fairly, we chose all user-defined

iteration limits to allow the sampling-based (global or hybrid) methods to run for at least the same length of time as SPEDRE (-base or hybrid), prior to comparing accuracy. However it was often not possible to ensure equal runtime. SRES and its hybrids usually required additional runtime on large networks, and PSO sometimes suffered poor scaling as well. The GA method always converged very quickly, regardless of user-defined iteration limits, but this is not necessarily an advantage because the accuracy of GA (and GA hybrids) was significantly worse for large networks. A full assessment of comparative performance therefore requires a holistic view of the trade-off between runtime and accuracy.

Accuracy comparison based on the size-130 error-free test case (Figure 3.8A, asterisks) showed SPEDRE to be among the best scoring methods. Tied with SPEDRE were two hybrid global-local methods SRES_LM and PSO_LM. Error bars on these three methods are negligible, indicating that the performance was consistent across the three random replications of the test. Note that SRES_LM, PSO_LM, and SPEDRE, in addition to comparable accuracy, showed comparable runtime (first column group). It should be noted that LM had much worse performance (blue columns marked with LM label) when not seeded with an initial guess from global methods such as SPEDRE-base, SRES or PSO.

For the 20%-noise test case, Figure 3.8B showed a set of 5 methods (marked with asterisks), including SPEDRE, that were tied for best performance. This comparative result should be interpreted with awareness that all methods had poor absolute accuracy (see Table 5.1B, column 130).

For test cases of size below 100 (Table 5.1A, column 30-90), the local search method LM easily achieved best accuracy, as did any LM-hybrid methods (rows for species MRE, maximum PPE, median PPE and weight SSE, cells highlighted in red). For

networks of size 100 and above (columns 100-150), LM performed worse than any LM-hybrid method, with the exception of the size-110 test case. In test cases of size 110 to 140 (column 110-140), SPEDRE was tied with PSO_LM in accuracy (species MRE row, cells highlighted in red) and both were not worse than any other method. Test cases of size 100 and 150 were the only large cases where SPEDRE did not achieve the best score.

As expected, introduction of 20% noise (Table 5.1B), caused worse accuracy on most methods, compared with noiseless tests (Table 5.1A). For tests with 20% noise, SPEDRE and SRES_LM were the best performing methods for large test cases, according to the species MRE score, except in the test of size 140 (Table 5.1B, comparing the Species MRE set of rows, with best scores in red). In the size-140 test case, SPEDRE scored worse than other LM-hybrid methods, but SPEDRE-base_SD achieved the same best score as other LM-hybrid methods (column 140, species MRE row, cells highlighted in red). Based on other measures of accuracy (maximum PPE, median PPE and weighted SSE), the best scoring method may vary between test cases (maximum PPE, median PPE and weighted SSE, cells highlighted in red), but most best-scoring methods are LM-hybrid methods. We thus conclude that SPEDRE was “tied” with other state-of-the-art methods, for the spectrum of artificial, low-degree data-rich problems we constructed.

In summary, the best performing methods (asterisks in Figure 3.8) are consistently SPEDRE and a subset of hybrid stochastic-local methods. Highly similar scores can occur when multiple methods converge to the same local optimum. Accuracy tests showed the following trends: (a) for small networks, local methods performed well; (b) hybrid methods (including SPEDRE) showed superior accuracy to standalone local or global methods; (c) SPEDRE accuracy was comparable to the accuracy of other hybrid methods; (d) the quality scores of SPEDRE-base were significantly worse than SPEDRE, confirming that the LM post-processor is indeed important for refining discretized results.

We conclude that SPEDRE was “tied” with other state-of-the-art methods, for the spectrum of low-degree data-rich problems we constructed.

Web service performance

Depending on execution configuration, SPEDRE can achieve various performance outcomes. Table 3.2 shows the web server’s performance on 5 test cases using noiseless and 20%-noise data. The objective function value provides an indication of how well the simulated dynamics using estimated rate constants matches the time-series data. The total run time is represented as the sum of the SPEDRE run time and the Levenberg-Marquardt local optimization run time. SPEDRE was executed with lower bound = 0, upper bound = 1, logarithmically spaced binning with 5 bins, maximum number of iterations = 5, Gaussian noise = 0 and number of samples per voxel = 5.

	Objective function value	BPPE run time (s)	LM run time (s)	Total run time (s)
Circular network (80 species)	0.71	17.00	3.17	20.17
Tree network with random branching (80 species)	1.56	75.00	4.26	79.26
PI3K/Akt cascade	6.72E-07	25.00	0.41	25.41
MAPK cascade	9.29E-07	91.00	0.51	91.51
Actin Filament Assembly / Disassembly	1.37	468.00	0.51	468.51

Table 3.2 – SPEDRE’s performance on synthetic networks (circular network, tree network with random branch) and biological networks (PI3K/Akt cascade, MAPK cascade and Actin Filament Assembly / Disassembly pathway).

The test cases used coarse discretization to complete fast at the expense of accuracy. For the PI3K/Akt cascade and the MAPK cascade, the objective function was low, indicating good match with data. Run time was low for Levenberg-Marquardt post-processing compared to SPEDRE, indicating that a hybrid global-local method incurs low additional run time cost compared to a global method alone. The BPPE run time gives empirical validation of the asymptotic run time. The high-degreed Actin Filament

Assembly / Disassembly pathway has only 14 species and 25 reactions while the low-degreed circular network has 80 species and 80 reactions, yet execution on the latter network finishes about 27 times faster than the former.

3.8 Discussion

Contribution

The key innovations of SPEDRE are the use of a probabilistic graphical model to decompose the dual objective function, and pre-computation of discrete solutions to each subproblem. The method has a well-defined asymptotic runtime and good scalability, in exchange for approximate heuristic optimization.

The web-service interface of SPEDRE has its unique properties from other competitors and the computational power of a web server makes it suitable for intensive rate constant estimation jobs. The server has dynamic display of the bin plot, as shown in Figure 3.4 (bottom) which is customizable, due to the interface with the Google Chart API. There are certain limited types of invalid input that are tolerated, such as by eliminating mis-input datapoints from the data file. The interface with Copasi (Hoops, *et al.*, 2006) also provides an automatic "rescue" for parameter estimation problems involving a dense network or other features that violate the requirements of SPEDRE. This service is not predictive because measured rate constants are not yet available for pathways of significant size. For users who wish to address the accuracy of parameter estimation as a purely mathematical problem, artificial datasets are available and a weighted sum of squared error (SSE) is displayed.

The SPEDRE approach aims for asymptotic scalability at the expense of accuracy. This philosophy appears in (a) the use of splines to approximate the species derivative, (b) the use of binning to discretize the parameter space, and (c) the use of loopy belief propagation for probabilistic inference. Each of these elements can introduce error. We

believed that the dangers of compounded errors would make the SPEDRE method less robust to noisy data than simulation-based methods. The expected sensitivity of SPEDRE to input noise has not yet been confirmed in the tests shown (and in other tests); rather we found that all methods gave unacceptably poor answers with noisy data. Future work must continue to characterize the numerical stability, approximation error, and noise tolerance of SPEDRE and other parameter estimation methods.

The accuracy and speed of SPEDRE were compared against several methods of parameter estimation, in low-degree, data-rich test cases. SPEDRE performance was competitive in all tests, and SPEDRE was the best performing method for the Akt network test. We conclude that SPEDRE performs well when tested in the specific niche of problems for which it was designed. Naturally the SPEDRE performance would degrade (perhaps exponentially) outside of its intended niche. SPEDRE exhibits an abrupt trade-off between problem type and performance, but performance trade-offs are not new to parameter estimation research. Major pathway simulation software packages already maintain collections of multiple parameter estimation methods, rather than expecting a single best method to cover all problems.

A current hurdle for broader applicability of SPEDRE is the inability to handle high-degree nodes. Many biological networks are scale-free (*i.e.* the degree distribution follows a power law). Thus, while many small networks are low-degree, large networks often have at least one hub. In order for new spline-based collocation methods to be truly superior to conventional (“primal” objective) parameter estimation methods, they would have to handle high-degree networks and extensive gaps in experimental observations, robustly. Future innovations may be able to develop a new composition of parameter estimation methods, so that low-degree subproblems can be solved by SPEDRE and high-degree hubs can be treated separately.

A side-effect of our work is to provide performance comparisons for several hybrid and standalone parameter estimation methods. Our tests reproduced the earlier observation that hybrid methods generally perform better than standalone global methods (Ashyraliyev, *et al.*, 2009; Rodriguez-Fernandez, *et al.*, 2006). Future work may be able to exploit this non-additive runtime effect, perhaps through deeper integration of global and local search methods, rather than applying independent methods sequentially.

Data mountain: challenges and opportunities

Development of high-throughput technologies has enabled large-scale quantitative readouts for many proteins simultaneously (Yaffe, 2008). The massive amount of information is a challenge for many researchers who seek to unfold the complex mechanism of many biological functions. Particularly, this potentially rich source of biological knowledge calls for novel data analysis and modeling paradigms (Tan and Linding, 2009).

Systems biology was famously attacked by Sydney Brenner as “low input, high throughput, no output” (Friedberg, 2008). However, when applied to large-scale data (high input), the “high throughput” capability of computational modeling can be powerful enough to discover many complex biological relationships than many other methods. Indeed the advent of large scale technologies, such as genomics and proteomics technologies, created an opportunity where computationally driven analysis methods could accelerate the pace of knowledge discovery.

From large quantitative proteomics data, Toni *et al.* employed Bayesian model selection to infer the posterior distribution over four models for phosphorylation and dephosphorylation dynamics, and computed the amount of support given to each model (Toni, *et al.*, 2012). In a different context, Tan and Linding surveyed and devised various computational methods to handle phosphorylation data detected in systematic proteomic

experiments for a “kinome” network reconstruction (Tan and Linding, 2009). These cases underline the importance of handling massive amount of data.

A distinguishing feature of SPEDRE is that it requires large amounts of concentration measurement data, which would have been prohibitive a decade ago. Traditional experimental methods required an investment of labor and resources that was roughly linear in the number of proteins studied. New proteomic methods can measure additional proteins at virtually no additional cost, and proteomic datasets are starting to provide data-rich environments with measurements of all proteins in a system. SILAC technology has recently been used for time-series measurements of 147 proteins (Tasaki, *et al.*, 2010) in NIH3T3-derived cells, and again for time-series of 534 proteins in the cytosol and 626 proteins in the nucleus in glucocorticoid-exposed myogenic cells (Reeves, *et al.*, 2009). Most proteomic studies have not been performed with time-series repeats for studying dynamics, but large-scale dynamic data will become increasingly available with the explosive growth in the number of proteomic experiments (Zhang, *et al.*, 2011). New studies of large networks will give rise to huge parameter estimation problems, with rich datasets, but with too many unknown parameters for conventional methods to solve.

We believe that proteomic technology both enables and requires novel approaches to parameter estimation such as SPEDRE. As models grow in size due to technological advances, decomposition-based methods will probably dominate non-decomposition-based search methods, which suffer from the curse of dimensionality. The trade-offs exhibited by our method may be increasingly desirable for future trends in parameter estimation.

CHAPTER FOUR: REDOX-REGULATED AKT ACTIVATION – BIOLOGICAL TEST CASE FOR SPEDRE AND OPPORTUNITY FOR MODELING

Cell signaling pathways and metabolic networks are increasingly subject to mathematical modeling that simulates biochemical reaction kinetics using ordinary differential equations to represent the production/consumption of molecular species over time. Whether a model is built *de novo*, or adapted by recalibrating a previous model for a new cellular context, there is often a need to estimate kinetic rate constants based on time-series experimental measurements of molecular concentrations or enzyme activities. The SPEDRE method described in the previous chapter estimates reaction rates for biochemical networks, taking as input the connectivity of the network and the concentrations of the molecular species at discrete timepoints. The method was tested on artificial networks that could satisfy the requirement of sparse networks with abundant observation of pathway species.

After testing SPEDRE on a series of artificially constructed networks, we next applied the SPEDRE method to a real-life pathway which describes the redox-regulation of Akt activation based on previous experimental studies of Akt by our collaborators (Lim and Clement, 2007). Recall that aberrant hyper-activation of the Akt pathway has been detected in up to 50% of all human tumors and the Akt pathway is an attractive target for anti-cancer drug discovery (Mitsiades, *et al.*, 2004). Our model of Akt includes oxidative inactivation of the lipid phosphatase and tensin homolog on chromosome 10 (PTEN), as well as the phosphatidylinositol 3-kinases (PI3K) activation, as competing regulators of Akt in serum-stimulated fibroblasts (Kwon, *et al.*, 2004; Testa and Bellacosa, 2001). A more detailed understanding of PTEN dynamics is important because many cancers activate Akt through disruptions of PTEN.

In this chapter, we will first give a background overview of signaling pathway modeling (Section 4.1), before introducing the kinase Akt and its activation pathways (Section 4.2). We will then describe the modeling efforts for constructing a redox-regulated model of Akt activation (Section 4.3-4.6). Section 4.7 describes the Akt activation pathway model constructed as a biological test case to benchmark the performance of the SPEDRE method with current state-of-the-art parameter estimation methods. As a side effect, the Akt model brings out a puzzling phenomenon (Section 4.8) that requires further investigations, which will be covered in Chapter Five.

4.1 ODE modeling of cell signaling pathways

Signal transduction pathways (signaling pathways) are actively being unraveled and reconstructed (Palsson, 2011). Many disease processes (such as heart disease, diabetes, autoimmunity, and cancer) arise from defects in signal transduction pathways, which underscores the importance of studying signaling pathways (Loewenstein, 1999). In modeling study of signaling pathways, it is an essential task to describe the biochemical processes involved and ultimately formulate a mathematical model.

Mathematical modeling is a powerful technique to describe and abstract the underlying processes involved in complex systems such as those in a cell or organism (de Jong, 2002). For signaling pathways, mathematical models use quantitative variables to represent the concentrations of the signaling molecules and describe the rates at which these molecules interact under the physical and biochemical laws that govern the reactions. To describe biochemical processes in signaling pathways, many modeling formats have been developed including stochastic modeling, probabilistic modeling, and ordinary differential equation (ODE) modeling. This thesis will work exclusively with ODE modeling for signaling pathways, which is a continuous and deterministic modeling framework describing the production/consumption rates of the species in a pathway. For

studies of complex biochemical pathways, ODE modeling has been highly successful at elucidating complex dynamic behaviors (Aldridge, *et al.*, 2006) and emergent properties in a complex system (Huang and Ferrell, 1996). Modeling has the potential to supplement or to reduce the number of bench work experiments required for hypothesis generation and biological data interpretation (Voit, 2000).

ODE modeling typically includes model construction, calibration (*i.e.* parameter estimation), simulation, and analysis. The following subsections will describe in more detail each of the techniques listed above.

Model construction

Before constructing a model, it is an essential task to search for published models that are topologically similar or having common species and reactions to the current signaling pathway of interest. If the model of interest is built *de novo*, canonical knowledge of the pathway should be gathered from literature and evaluated for inclusion/exclusion in the model. Upon the derivation of the model topology from literature evidence and other necessary assumptions, an equivalent system of ODEs for the model can be constructed.

Following the construction of the ODEs, the parameter values (initial values of system components and kinetic parameters of chemical reactions) are obtained from literature evidence or marked for parameter estimation (described in the next section). Literature evidence may also help confine the unknown parameters to certain ranges based on the biochemical reactions involved. The narrower the permissible ranges of the parameters, the easier it is for the optimization process to find a good solution (*i.e.* prediction for parameter values) since the search space will be smaller. Assumptions and constraints for the model should be clearly defined at this stage.

Model calibration (parameter estimation)

Construction of ODE models requires knowledge of the reaction rates and initial concentrations, which must typically be estimated based on experimental measurements of molecular concentrations over time. The process of estimating model parameters is referred to as model calibration or parameter estimation. This is equivalent to a search in the space of models (same network topology with different parameter values) for a small subset of models that could produce time-course simulations in agreement with the training data. Model calibration is a critical and difficult step in any ODE modeling study, due to the complex interdependency between the ODE variables. Parameter estimation can be a challenging task because some ultra-sensitive models may exhibit vastly different dynamics and property with different parameter values (Trunnell, *et al.*, 2011).

Model calibration (parameter estimation) involves solving an optimization problem, which essentially attempts to minimize an objective function that measures the quality of an estimated parameter set in satisfying a given criteria (*e.g.* recapitulating dynamics of training data) for the ODE model. More discussion of the metrics for evaluating goodness-of-fit in model calibration can be found in Chapter Five. However, model calibration is often a difficult nonlinear optimization problem (Kleinstein, *et al.*, 2006) which poses a challenge to many modeling research studies including this work. Thus manual tuning still play an important role in calibrating ODE model for signaling pathways (Albeck, *et al.*, 2008; Basak, *et al.*, 2007; Birtwistle, *et al.*, 2007).

Innovative parameter estimation algorithms continue to be developed with significant improvement over previous methods. Many of these methods are heuristics-based, relying on randomized sampling of an exponential-sized parameter space, and therefore suffering from having slow runtime on large networks (Chou and Voit, 2009). A wide variety of optimization methods (Fogel, *et al.*, 1991; Kennedy and Eberhart, 1942 ;

Levenberg, 1944; Marquardt, 1963; Michalewicz, 1994; Runarsson and Yao, 2000) are applicable to the parameter estimation problems. A strategy of running some of these parameter estimation methods together with manual tuning will be adopted in Chapter Four.

Model simulation

After parameters are estimated, models can attempt to simulate new configurations of the system, which is essentially to extrapolate beyond the data used in model fitting. This means models can be used for predicting the experiments that have not been performed or used in calibration process. One of the most important steps to achieve this task is by performing dynamic simulation. Once the set of ODEs in the model is defined and the parameter values are known, the ODE system can be numerically solved, and thus the behavior of a network can be simulated in response to certain initial conditions and external inputs.

From the dynamics simulation, the time-dependent behavior of the concentrations (*i.e.* the ODE variables) can be obtained and analyzed. Various software packages such as SimBiology (The MathWorks, MA), COPASI (Hoops, *et al.*, 2006), and SBToolbox (Schmidt and Jirstrand, 2006) can graphically display the time course of any species in the system. These simulated time-series (or trajectories) provide a comprehensive dynamic view of the system, including the changes in species concentrations and in fluxes of reactions in the pathway. In addition to providing visualization of dynamic trends, model simulation is also useful as part of other analysis methods, described in the next section.

Model analysis

One very powerful property of ODE models is their ability to simulate the time-dependent behavior of protein concentrations in the system. As the complexity increases

with the interplay between pathway species, dynamics become a rich source of information which may shed light on the underlying biological mechanisms of the signaling pathway. An example of how dynamical analysis could lead to biological insights can be found in a recent modeling study of plasmin activation mediated by urokinase-type plasminogen activator (Venkatraman, *et al.*, 2011). Simulation of the states and dynamics of plasmin activation suggested a transition of the plasmin steady state (*i.e.* bistability) that was dependent on the initial concentration of precursor urokinase. This prediction was subsequently validated *in vitro*, and the findings could have potential impact in the study of angiogenesis, metastasis, wound healing, and fibrosis.

Parameter sensitivity analysis (or sensitivity analysis for short) describes changes of molecule concentrations as result of changes in the values of parameters (thus sometimes referred as local sensitivity analysis). Sensitivity analysis has been shown to be a powerful tool to investigate complex kinetic models, identifying the “influential” parameters which has strong impacts on certain model behaviors (*e.g.* readout species) while screening out the non-influential ones (Komorowski, *et al.*, 2011).

Model identifiability analysis evaluates the theoretical possibility of learning the true value of the underlying parameter after obtaining an infinite number of observations. While it is unrealistic to obtain an infinite number of observations, the practical identifiability of the model can still be obtained by computing the Hessian matrix (or the Fisher information matrix). By inverting the Hessian matrix, the approximate Variance-Covariance matrix is obtained, and the diagonal elements of this matrix can be used to construct the confidence intervals for the parameters. With this knowledge, certain strongly correlated parameters can be removed or refined in order to improve model identifiability (Quaiser and Mönnigmann, 2009).

4.2 Akt activation pathway

The critical decision between cell survival and apoptosis is regulated by sophisticated signaling networks, where the kinase Akt (also known as protein kinase B – PKB) plays many important anti-apoptotic roles. Akt promotes cell survival by inactivating the pro-apoptotic proteins BAD, FKHR and pro-caspase-9; by activating the pro-survival kinase mTOR; and by inactivating the tumor repressor p53 through MDM2 (Carnero, *et al.*, 2008). Note that some articles may use “Akt” to denote the gene and AKT to denote the protein, but this work will refer to both as “Akt”. Akt is frequently overactivated in many cancer types (Osaki, *et al.*, 2004) and promotes resistance to anti-cancer drugs (Tokunaga, *et al.*, 2008). There are three known isoforms of the human Akt kinase: Akt1, Akt2, and Akt3; whose functions are specific to cell lines (Koseoglu, *et al.*, 2007). The three closely related isoforms consist of a central catalytic domain, a conserved N-terminal pleckstrin homology (PH) domain, and a C-terminal regulatory hydrophobic motif (Hanada, *et al.*, 2004). In serum starved primary and immortalized fibroblasts, Akt1 is catalytically inactive and can be activated by growth factors, rapidly and specifically. Akt2, also activated by growth factors, plays an important role in the maintenance of normal glucose homeostasis (Cho, *et al.*, 2001), and is found to be activated in $\approx 40\%$ of ovarian cancers (Yuan, *et al.*, 2000). Akt3 has a less clear role, but increased Akt3 enzymatic activity was detected in estrogen receptor-deficient breast cancer and androgen-insensitive prostate cancer cell lines (Nakatani, *et al.*, 1999), suggesting that Akt3 is involved in the aggressiveness of steroid hormone-insensitive cancers.

Except Akt3, all Akt isoforms contain two regulatory phosphorylation sites: Thr³⁰⁸ in the activation loop within the kinase domain, and Ser⁴⁷³ in the C-terminal regulatory domain. In vitro, phosphorylation of either Thr³⁰⁸ or Ser⁴⁷³ leads to partial activation of

Akt; and phosphorylation of both residues leads to a synergistic activation of the enzyme (Alessi, *et al.*, 1996). This thesis study will focus on the activation of Akt (all isoforms) by Thr³⁰⁸ phosphorylation, which is specifically phosphorylated by the kinase PDK1 (phosphatidylinositol dependent kinase 1). Activation of the kinase Akt by growth factors is mediated by its membrane recruitment by phosphatidylinositol (3,4,5)- trisphosphate (PIP3). In addition to the PIP3/Akt cascade, a number of novel Akt binding proteins have been identified and these proteins (including Actin, Erk1/2, Hsp90, and Hsp27) could regulate the activity of Akt, (Song, *et al.*, 2005).

One of the most well-studied mechanisms of Akt activation is the PIP3/Akt cascade. The membrane lipid phosphatidylinositol(3,4,5)-trisphosphate (PIP3) is capable of activating protein kinases (Newton, 2009), including the recruitment of Akt and PDK1 to the cell membrane, where Akt can be phosphorylated at Thr³⁰⁸ by 3- phosphoinositide-dependent protein kinase 1 (PDK1 or PDK1) (Raimondi and Falasca, 2011). Upon being phosphorylated, Akt dissociates from the plasma membrane and can be dephosphorylated by many phosphatases such as PP2A (Protein phosphatase 2). Therapeutic studies to inhibit the upstream pathway of Akt at different points, including the kinases (such as PDK1) and phosphatases (PP2A) are actively underway (Carnero, 2010).

4.3 Motivations for modeling dynamics of Akt phosphorylation upon activation by growth factors

Transient hyper-activation of Akt pathway in normal cells could provide insight into why tumor cells have sustained Akt activation (Leslie and Downes, 2004; Lim and Clément, 2007). A recent trend across biology is to separate the effects of signal duration (timing) from that of signal magnitude in determining some of the functions of a pathway (Ebisuya, *et al.*, 2005; Longo, *et al.*, 2008). A famous study of temporal control of the transcription factor NFkappaB activation unearthed a crucial signaling module for inter- and intracellular signaling, cellular stress responses, cell growth, survival, and apoptosis

(Hoffmann, *et al.*, 2002). In another case study using rat pheochromocytoma PC12 cells, sustained activation of ERK leads to neuronal differentiation whereas transient activation of ERK leads to increased proliferation (Qiu and Green, 1992). In the Akt pathway, traditionally the magnitude of phosphorylated Akt is associated with various signaling functions (Cicenas, *et al.*, 2005; Descamps, *et al.*, 2004; Lafon-Cazal, *et al.*, 2002), but recent studies have raised the importance of the kinetics of phosphorylated Akt, such as for cell proliferation (Costello, *et al.*, 2002; Donahue and Fruman, 2003; Murphy, *et al.*, 2002; Pouysségur and Lenormand, 2003) and cell cycle progression (Longo, *et al.*, 2007). Duration of Akt activation is therefore an important property that has not been fully characterized.

Understanding of the dynamics and duration of Akt activation is of wide applicability to various cell signaling functions. For studies of temporal pathway dynamics, mathematical modeling has been highly successful elucidating complex dynamic behaviors (Aldridge, *et al.*, 2006) and emergent properties in a complex system (Huang and Ferrell, 1996). Thus, we anticipate that modeling of Akt pathway dynamics will provide indirect information that may provide biological insight into the pathway.

4.4 Redox regulation of Akt activation pathway

Reactive oxygen species (ROS) can be damaging at high doses, but at low doses ROS participate in a range of normal signaling processes (“redox regulation”) (Flohé, 2010), for example via reversible modifications of cysteine residues (Stamler and Hess, 2010). Redox regulation is an important influence in signaling pathways involving tumorigenesis (Montero and Jassem, 2011), cancer cell metabolism (Cairns, *et al.*, 2011), inflammation (Li and Fukagawa, 2010) and cytoskeletal remodeling (Cannito, *et al.*, 2010). ROS have very potent effects on cell survival and apoptosis (Acharya, *et al.*, 2010), but the mechanisms are numerous and complex. Ratio of two intracellular ROS,

superoxide and hydrogen peroxide, correlates with cell fate decisions (Pervaiz and Clement, 2007; Zhu, *et al.*, 2011). In fibroblasts and endothelial cells, superoxide ($O_2^{\bullet-}$) was found to promote Akt activation and survival signaling with potency comparable to growth factors, via phosphatase inactivation (Clément and Pervaiz, 2001). We reported that $O_2^{\bullet-}$ promotes phosphorylation of Akt via S-nitrosylation to inactivate PTEN (Lim and Clément, 2007) in mouse embryonic fibroblasts (MEF). Several other mechanisms have been found for redox regulation of the Akt pathway, including the oxidation of protein tyrosine phosphatases (PTPs) and oxidation of pathway kinases such as PI3Kinase and Akt (Leslie, 2006).

4.5 Regulation of intracellular superoxide

Superoxide, a radical far less reactive than other free radicals such as HO^{\bullet} , does not react at all with most molecules in aqueous solution. First discovered as leakage from the electron transport chain in mitochondria, superoxide has long been studied as the key player in aging and apoptosis (Halliwell and Gutteridge, 2007). Superoxide also functions as a signaling species for cell (Pervaiz and Clement, 2007; Clément and Pervaiz, 2001; Suzuki *et al.*, 1997; Kamata and Hirata, 1999). Figure 4.1 shows the time-series dynamics of intracellular superoxide in MEF cells using lucigenin assay.

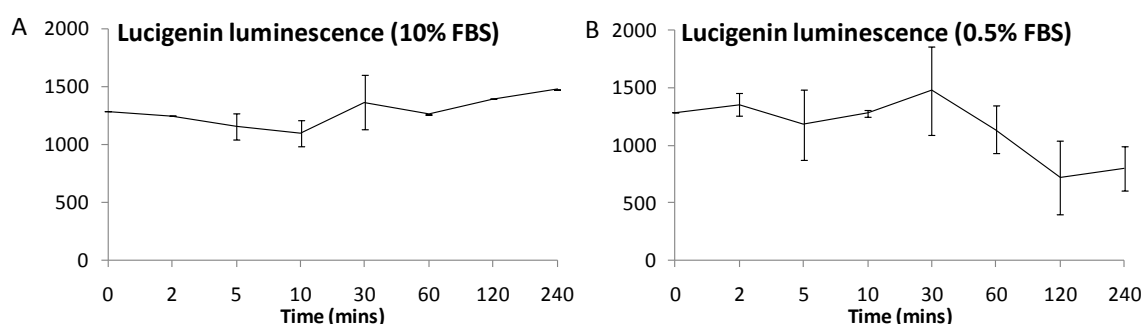


Figure 4.1 – Lucigenin measurements of superoxide time-series in MEF. Cells were grown in (A) 10%FBS or (B) serum starved in 0.5%FBS for different time points before intracellular superoxide level was measured by lucigenin luminescence. The level of intracellular superoxide was expressed as percent of DMSO control cells for each time point. The value represents the mean and standard deviation of two independent experiments.

forming a complex with it, and is released by H₂O₂ oxidization. This reduces the availability of Rac1, the activator of NOX, which consequently inhibits superoxide production.

4.6 Modeling redox-regulated Akt activation

The kinase Akt takes a “hub” position in the vast and complex signaling networks in various cell types (Chen, *et al.*, 2009). The mechanism and dynamics of Akt activation by growth factor is complex and is further complicated by various crosstalk with other pathway such as p53 and Erk. Study of Akt activation thus may shed light to the complex machinery that confers cell survival advantages to tumors. As a result, a number of published models were specifically built to study the activation and dynamics of Akt (Hatakeyama, *et al.*, 2003; Suresh Babu, *et al.*, 2008; Wang, *et al.*, 2009).

Many modeling studies of Akt, such as (Lee, *et al.*, 2008) and (Shih, *et al.*, 2008), collapse the Akt activation cascade into a single step containing only PI3Kinase and Akt. However, other studies such as (Hatakeyama, *et al.*, 2003; Suresh Babu, *et al.*, 2008), address the complex biochemical interplay between kinases, phosphatases and phospholipids in regulating the dynamics of Akt phosphorylation. The complexity of Akt dynamics also led to increasing efforts to construct multi-scale models, such as the study by (Shih, *et al.*, 2008) which describes the activation mechanisms of Akt both at the molecular scale and at the scale of the signaling network. However, it should be noted that few or no modeling studies have addressed the role of “intracellular environmental effects” such as redox regulation in the activation and dynamics of Akt.

We built a novel model of Akt activation (“Akt model”), using our experimental data from recent studies (Lim and Clément, 2007). The model was built manually based on dynamic measurements of the Akt pathway, observed in serum-starved mouse embryonic fibroblasts stimulated by the addition of 10% serum to the culture medium

(Lim and Clément, 2007). Recall that Akt is a kinase, frequently over-activated in cancers, that signals for survival and proliferation. The signaling events in our model of Akt activation are illustrated in Figure 4.3, Table 4.1, and described as below.

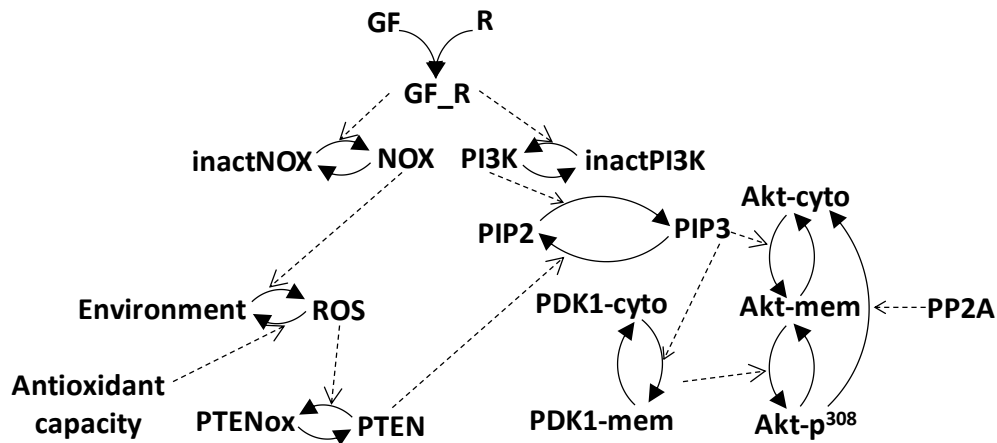


Figure 4.3 – Network diagram of the Akt model, including redox-regulation of PTEN.
 The prefix “inact” denotes inactive species; the suffix “cyto” (or “mem”) indicates cytosolic (or plasma membrane) localization. The suffix “p³⁰⁸” indicates phosphorylation at residue Thr³⁰⁸.

As PTEN oxidation promotes Akt activation, we represented the inactive form of PTEN by PTENox. The sources for generating ROS (O₂, water, etc.) and consuming ROS were group into “Environment”, in order to simplify the complex chain of cellular ROS production. Among the enzymes capable of catalyzing superoxide production (*e.g.* NOX and NOS family), the model simplifies the process by only using NOX, which can catalyze the production of ROS from Environment. DPI is known for inhibiting proteins in NOX family, as shown earlier in Figure 4.3. It has been observed that PTEN is oxidized by superoxide upon addition of GF stimulus, indicating a mechanism for GF_R to activate PTENox production (Lim and Clément, 2007). Therefore, it is hypothesized that the signal from GF_R is transmitted to PTENox by activating NOX, which in turn activates superoxide production, which promotes PTEN oxidation. “Antioxidant capacity” (such as SOD), which can be inhibited by DDC functions as a counterbalance of NOX to maintain homeostatic level of ROS (Halliwell and Gutteridge, 2007).

Akt is activated after stimulation by serum (growth factors), not only via the canonical activation of PI3Kinase (PI3K) by serum, but also via reactive oxygen species (ROS) and ROS-induced inactivation of the phosphatase PTEN. ROS are produced by NADPH oxidase (NOX), and degraded by anti-oxidants. The phosphorylation and activation of Akt is a multi-step process, involving the translocation of Akt from the cytosol to the cell membrane and its phosphorylation by the kinase PDK1 at Thr³⁰⁸. The translocation of Akt and PDK1 to the membrane is controlled by the level of phosphatidylinositol 3,4,5-trisphosphate (PIP3), which is determined by the balance between PIP3 production (by serum-activated PI3Kinase) and PIP3 degradation (by the PTEN phosphatase). Phosphorylated Akt returns to the cytosol and is subject to dephosphorylation by PP2A.

Index	Reaction	Rate constant name	Value
1	GF + R → GF_R	k_uptake	14.39
2	inactNOX → NOX	kM_activNOX	0.1
3	inactNOX → NOX	kcat_activNOX	5.19
4	inactPI3K → PI3K	kM_activPI3K	0.09
5	inactPI3K → PI3K	kcat_activPI3K	6.81
6	NOX → inactNOX	k_deactNOX	3.19
7	PI3K → inactPI3K	k_deactPI3K	8.46
8	Environment → ROS	kM_NOX	0.15
9	Environment → ROS	kcat_NOX	13.56
10	ROS → Environment	kM_AntioxidantCapacity	1
11	ROS → Environment	kcat_AntioxidantCapacity	50
12	PTEN → PTENox	kM_ROS	0.09
13	PTEN → PTENox	kcat_ROS	0.72
14	PIP2 → PIP3	kM_PI3K	0.3
15	PIP2 → PIP3	kcat_PI3K	0.4
16	PIP3 → PIP2	kM_PTEN	0.3
17	PIP3 → PIP2	kcat_PTEN	0.5
18	Akt-cyto → Akt-mem	kcat_PIP3_Akt_cyto	0.4
19	Akt-mem → Akt-cyto	k_Akt_cyto	0.01
20	Akt-mem → Akt-p ³⁰⁸	kcat_PDK1_mem	0.6
21	Akt-p ³⁰⁸ → Akt-cyto	kcat_PP2A_Akt_cyto	0.1
22	Akt-p ³⁰⁸ → Akt-cyto	kM_PIP3_PDK1_cyto	0.5
23	PDK1-cyto → PDK1-mem	kcat_PIP3_PDK1_cyto	0.22
24	PDK1-mem → PDK1-cyto	k_PDK1_mem	0.12

Table 4.1 – Rate constant and nominal values in the Akt model.

The prefix *kM* indicates a Michaelis-Mentent constant. The prefix *kcat* indicates a catalytic rate constant. As described in main text, the prefix “inact” denotes inactive species; the suffix “cyto” (or “mem”) indicates cytosolic (or plasma membrane) localization; and the suffix “p³⁰⁸” indicates phosphorylation at residue Thr³⁰⁸, which is crucial for Akt activation. The following species have initial concentration of 1.0: GF, R, NOX, PI3K, Environment, SOD, PTEN, PIP3, Akt-cyto, PP2A, PDK1. The remaining species have initial concentration of 0.0.

4.7 Performance of SPEDRE in comparison with other standalone and hybrid methods on the Akt model

Using simulation, we generated complete datasets with artificial noise at levels of 0%, 1%, and 20%. Experiment setups follow the artificial test cases described in Section 3.6. Parameter estimation performance was compared between SPEDRE and some popular methods (Figure 4.4). The complete comparison results (14 methods using 6 different noise levels) are shown in Table 4.2.

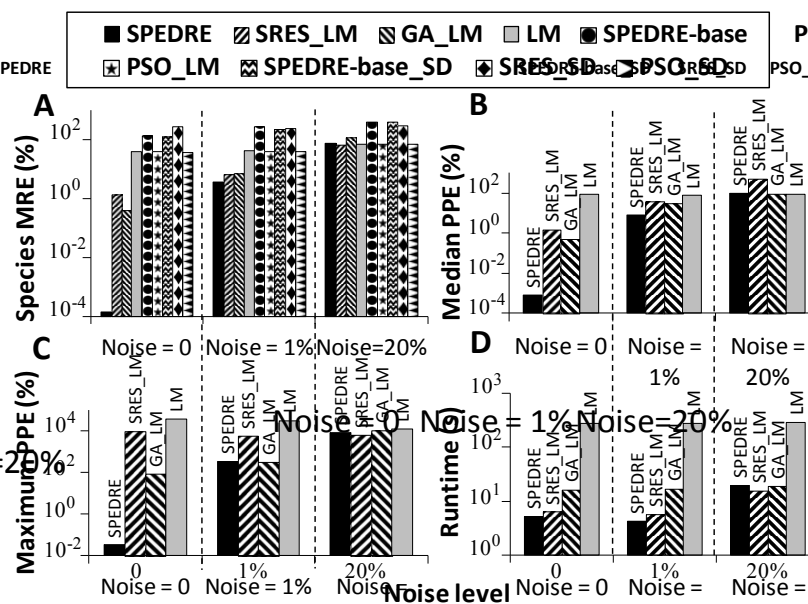


Figure 4.4 – Comparison of parameter estimation algorithms applied to the Akt network, with noise levels 0, 1% and 20%. Method performance was assessed by (A) species maximum relative error (MRE), (B) median parameter percentage error (PPE), (C) maximum parameter percentage error, and (D) runtime.

According to Figure 4.4A-C, the prediction quality of SPEDRE (leftmost bar, shaded black) is better than the other methods for noise-free and 1%-noise data sets. With noise levels of 20%, all methods perform unacceptably, providing worse than 100% species maximum relative error, as shown in Figure 4.4A. Similarly, on the 20%-noise data set, all methods have unacceptably high median and maximum parameter percentage error, as shown in Figure 4.4B-C. In this parameter optimization test with Akt dynamics, SPEDRE out-performed other methods, indicating that the parameter neighborhoods it

gave to LM were better than the neighborhoods from other global methods, even though SPEDRE-base had equivalent performance in non-biological tests.

Figure 4.4D also displays a counterintuitive phenomenon, in which the local search method LM takes longer to run than any hybrid method including LM as a post-processor. LM performs many iteration cycles if it starts with a random guess, but it converges quickly if it starts with the output of a global search method. Adding more phases of search would be expected to increase rather than decrease the total runtime, but in this case, a phase of global search led to faster LM convergence, which more than compensated for the time of running the global search.

A	Gaussian Noise	SPEDRE-base	SD	SRES	PSO	LM	GA
	Run time (s)	0%	0.11	13.16	69.42	272.70	272.70
	1%	0.09	13.55	66.88	278.09	278.09	17.45
	2%	0.08	15.34	62.69	270.17	270.17	10.55
	5%	0.09	15.53	68.72	272.19	272.19	15.47
	10%	0.09	14.39	57.81	328.20	328.20	8.95
	20%	0.08	11.31	67.53	282.88	282.88	21.83
Species MRE	0%	139.71	651.59	276.99	38.57	38.57	207.01
	1%	279.58	649.47	251.58	40.41	40.41	306.70
	2%	168.50	649.98	312.91	14.39	14.39	327.88
	5%	358.35	655.63	269.93	15.16	15.16	133.78
	10%	350.64	656.86	324.63	41.42	41.42	329.15
	20%	401.46	670.21	303.99	71.40	71.40	209.25
Median PPE	0%	37.95	5695.86	3046.31	86.67	86.67	74.49
	1%	90.47	5688.68	2679.22	75.60	75.60	94.92
	2%	69.06	5678.84	2711.93	68.13	68.13	99.54
	5%	96.48	5699.22	2082.84	98.97	98.97	74.86
	10%	181.24	5684.21	1423.99	94.33	94.33	95.58
	20%	86.93	5698.06	1913.27	91.70	91.70	97.77
Maximum PPE	0%	5119.05	394607.37	257379.30	39476.90	39476.90	30494.72
	1%	10393.03	453194.65	180024.46	31861.77	31861.77	7099.94
	2%	12395.93	486121.75	177815.97	13015.37	13015.37	17846.60
	5%	42036.94	344113.26	36698.60	17219.76	17219.76	1012.34
	10%	39882.51	443011.03	310906.61	49899.80	49899.80	5252.86
	20%	6139.83	388826.77	106555.93	12211.36	12211.36	12715.30

B	Gaussian Noise	SPEDRE	SRES	LM	PSO	LM	GA	LM	MLBP	SD	SRES	SD	PSO	SD	GA	SD
	Run time (s)	0%	5.11	6.31	3.53	16.53	9.03	0.42	0.17	4.72						
	1%	4.14	5.80	0.91	16.95	0.61	0.44	0.38	0.59							
	2%	3.00	5.91	1.98	2.72	0.61	0.22	0.17	3.97							
	5%	5.20	9.63	2.42	6.20	0.64	0.28	0.17	6.30							
	10%	6.73	16.08	22.19	14.36	0.63	0.22	0.23	7.34							
	20%	19.09	15.56	16.27	18.88	0.53	0.44	0.20	1.13							
Species MRE	0%	1.44E-04	1.37	39.19	0.41	130.16	276.55	38.57	206.99							
	1%	3.51	6.74	40.34	6.96	233.96	251.38	40.41	307.27							
	2%	7.00	7.14	14.28	6.99	168.48	312.89	14.39	327.85							
	5%	17.90	17.89	15.34	17.43	354.81	269.86	15.17	104.31							
	10%	36.01	34.74	40.35	33.38	348.85	324.63	41.42	249.89							
	20%	71.72	66.45	71.28	117.40	394.03	303.83	71.40	209.25							
Median PPE	0%	8.18E-04	1.46	86.61	0.52	34.08	3046.31	86.67	68.10							
	1%	7.76	37.39	75.60	30.13	94.86	2679.22	75.60	94.47							
	2%	21.61	16.64	68.09	17.42	69.05	2711.93	68.13	98.63							
	5%	33.68	46.49	98.29	27.59	93.25	2082.84	98.97	30.65							
	10%	60.94	98.97	98.94	88.71	182.22	1423.99	94.33	95.86							
	20%	93.32	519.97	87.40	91.55	94.95	1913.29	91.70	97.77							
Maximum PPE	0%	3.23E-02	9898.98	39281.20	86.64	5144.11	257379.30	39476.90	30494.72							
	1%	352.71	5666.18	31862.44	326.44	10392.66	180024.46	31861.77	7099.94							
	2%	587.63	9900.00	13003.46	584.17	12395.93	177815.97	13015.37	17273.97							
	5%	9679.44	3308.92	17113.54	353.17	42036.82	36698.60	17219.76	198.35							
	10%	9085.24	22857.83	49460.50	18064.79	39882.51	310906.61	49899.80	5275.28							
	20%	8307.48	6621.28	12235.64	10563.50	6139.73	106555.62	12211.36	12715.30							

Table 4.2 – Comparison of rate parameter estimation methods applied to the Akt model. The methods were grouped standalone (A) and hybrid (B) methods. Each dataset used in each test case was constructed by simulating the network using nominal reaction rates. Different levels of Gaussian noise were added to the simulated dataset: 0%, 1%, 2%, 5%, 10%, and 20%. The accuracy of each method was evaluated using species MRE, median PPE and maximum PPE.

4.8 Puzzling redox regulation phenomenon in serum-induced Akt activation

Despite recent progress, there remain many puzzling effects of redox regulation in cancer cells (Reeves and Hoffmann, 2009; Ufer and Wang, 2011). One such puzzle can be found in our own previous work, where we give 10% serum to cells growing in 0.5% serum, to trigger both superoxide production and Akt pathway activation. In particular, MEF^{PTEN^{-/-}} cells exhibited strong Akt activation upon serum-stimulation, unless superoxide production had been blocked with the inhibitor diphenyleneiodonium chloride (DPI) as shown in Figure 4.5 and (Lim and Clément, 2007). Although serum (containing a cocktail of growth factors) had been found to augment Akt activation via superoxide and oxidation of PTEN, the apparent ability of superoxide to increase Akt activation in MEF^{PTEN^{-/-}} cells suggests an additional, novel PTEN-independent mechanism.

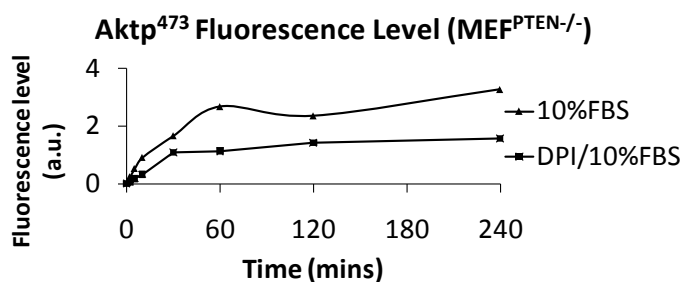


Figure 4.5 – Time series data from MEF^{PTEN^{-/-}} cells treated with 10%FBS with or without DPI pre-incubation for 2 hours. Data obtained from Dr. Sharon Lim and quantified by the author.

4.9 Conclusion

Redox regulation is a major mechanism controlling the Akt activation pathway, and study of this regulation mechanism may lead to potential therapeutics application (Leslie, 2006). We constructed a novel Akt model which contains mechanisms for ROS to control the dynamics of Akt Thr³⁰⁸ phosphorylation. Model simulation could lead to important insights about the dynamics of redox regulation in MEF cells, although more measurements would be required for model calibration.

The model was used as a realistic test case for comparison between SPEDRE and other state-of-the-art parameter estimation methods. Benchmark performance of SPEDRE

was shown to be superior to other methods in terms of accuracy, while the runtime of all methods was comparable. However, certain limitations of SPEDRE, including its stringent requirement of rich data and sparse networks (as discussed in Section 4.7 of the previous chapter), still remain a problem for future development.

While building the Akt activation pathway models, a puzzling phenomenon (Figure 4.5) motivated us to perform further investigations into the activation dynamics of Akt under serum induction. It was also noticed from the time-series measurements that the Akt activation pathway contained non-trivial dynamics (with peaks and declines) that might not be fully explained by the current literature (Hatakeyama, et al., 2003). The next chapter will describe a modeling study which identifies a mismatch between the canonical pathway and current data from serum-induced Akt activation. We use modeling to characterize the ups and downs in the time-series dynamics of Akt phosphorylation, and consequently we discover unexpected difficulty in using the canonical model to explain even the qualitative ups and downs of the time-series measurements. The chapter then proposes some alternative hypotheses capable of reconciling the model with the observations.

CHAPTER FIVE: NON-CANONICAL ACTIVATION OF AKT IN SERUM-STIMULATED FIBROBLASTS, REVEALED BY COMPARATIVE MODELING OF PATHWAY MECHANISMS

5.1 Introduction

The pathway of Akt activation has many documented influences (Carnero, 2010; Leslie, 2006; Osaki, *et al.*, 2004; Reeves and Hoffmann, 2009; Ufer and Wang, 2011) but the key steps can be summarized simply. Growth signals and stress pathways activate PI3K, which converts PIP2 (Phosphatidylinositol (4,5)-bisphosphate) into PIP3 (Phosphatidylinositol (3,4,5)-trisphosphate). PIP3 is a membrane phospho-lipid with potent signaling effects, and its concentration is kept low by the PTEN phosphatase, which converts PIP3 back into PIP2 (Vazquez and Devreotes, 2006). PIP3 activates PDK1 (3- phosphoinositide-dependent protein kinase 1 or PDK1) through a binding reaction that recruits PDK1 to the cell membrane (Newton, 2009). PIP3 also recruits Akt to the cell membrane, where Akt can be phosphorylated at Thr³⁰⁸ by PDK1 (Raimondi and Falasca, 2011). We use Thr³⁰⁸ phosphorylation interchangeably with Akt activation because the phosphorylation of Akt at Thr³⁰⁸ correlates strongly with Akt kinase activity, and in some contexts is a better correlate with activity than Ser⁴⁷³ (Vincent, *et al.*, 2011). Active Akt dissociates spontaneously from the membrane, and targets many downstream effectors (Ananthanarayanan, *et al.*, 2007). The PP2A phosphatase de-phosphorylates and inactivates Akt (Liao and Hung, 2010). We refer to these key steps as the “canonical” Akt pathway. The total net activation of Akt represents a competitive dynamic between processes of activation and inactivation.

Many signaling “hubs” such as Akt achieve differential specificity of downstream function in part through the dynamics of activation, and not only through the magnitude of activation (Ebisuya, *et al.*, 2005; Longo, *et al.*, 2008). Temporal effects in the

activation of NF-kappaB have been found to regulate cell growth, survival, and apoptosis (Hoffmann, *et al.*, 2002). In MAPK signaling, transient versus sustained activation of Erk is responsible for the difference between proliferation and neuronal differentiation in rat pheochromocytoma PC12 cells (Qiu and Green, 1992). In the TGF- β /Smad signaling pathway, changes in doses of TGF- β stimulation have differentiated effects on short-term versus long-term P-Smad2 response dynamics (Zi, *et al.*, 2012; Zi, *et al.*, 2011). By precisely controlling the p53 response duration upon DNA damage, Purvis and colleagues discovered different fates for cells exposed to p53 pulses (recovery) versus cells exposed to sustained p53 signaling (senescence) (Purvis, *et al.*, 2012). In the Akt pathway, dynamics are also important. Both cell proliferation (Costello, *et al.*, 2002; Donahue and Fruman, 2003; Murphy, *et al.*, 2002; Pouysségur and Lenormand, 2003) and cell cycle progression (Longo, *et al.*, 2007) have been found to depend on the timing, not just the magnitude, of Akt activation.

When quiescent cells are stimulated with growth factors, the level of phosphorylated Akt rises from very low to a brief extreme of very high activation, followed by a decline to a moderate steady level. Indeed many signal transduction pathways have a similar trend, which is routinely attributed to receptor internalization. This peak and decline (sometimes called “overshoot” or “negative feedback”) is a dominating feature of Akt dynamics.

Previous modeling studies (Hatakeyama, *et al.*, 2003; Suresh Babu, *et al.*, 2008; Wang, *et al.*, 2009) have included the PIP3/Akt pathway, but their focus of analysis has been the downstream targets of Akt (*e.g.* Erk) and the crosstalk between the PIP/Akt pathway with other pathways (*e.g.* Ras/Raf). Thus the relationship between the peak-and-decline dynamics of PIP3 and Akt Thr³⁰⁸ has not been questioned in these studies. Previous modeling has simulated the peak and decline of Akt phosphorylation by

assuming a receptor-internalization effect (Hatakeyama, *et al.*, 2003), but this assumption should be examined more rigorously. Akt is an exceedingly popular protein in biomedical research, with >5000 Akt publications in NCBI Pubmed (<http://www.ncbi.nlm.nih.gov/pubmed/>) during 2011. Countless groups perform time-series measurements of phospho-Akt, expecting it would reflect the canonical pathway, including PI3K, PTEN, PIP3, and PDK1. For example, our previous work measured Akt activation dynamics, as readout for the downstream functional impact of PTEN modification (Lim and Clément, 2007). The use of Akt as a landmark makes it particularly important to understand Akt activation dynamics accurately and quantitatively.

Mathematical modeling with ordinary differential equations (ODEs) can simulate the simultaneous interplay between multiple activation and inhibition effects, and has been particularly useful for revealing how simple binary reactions can come together to produce a complex emergent behavior (Aldridge, *et al.*, 2006; Huang and Ferrell, 1996). Another use of dynamic models is to compare simulations against observations, and identify unexplained effects or incompatibilities that might escape notice without quantification. In previous work, we used a dynamic model of pathway activation to uncover unknown effects of the drug LY303511 in regulating the sensitivity of HeLa cervical carcinoma cells to apoptosis (Shi, *et al.*, 2009). In this way, detailed analysis of network dynamics can help find novel relationships. The peak and decline of Akt activation contain implicit dynamic information, which can be analyzed via modeling, and may shed light on system regulation.

When an observed behavior has an unknown mechanism, computational modeling can be used for generating and managing a set of alternative biochemical hypotheses, as demonstrated by Hua *et al.* for alternative mechanisms of Bcl-2 (Hua, *et al.*, 2005). The

use of models for hypothesis construction and evaluation is particularly powerful in studying pathways where many signaling species participate in highly intertwined and sometimes non-intuitive networks. Carrying out wet lab experiments to probe each candidate in a traditional hypothesis-experiment approach consumes valuable time and resources. In contrast, a hypothesis-model-experiment paradigm may contain less expensive cycles of hypothesis-model-hypothesis that can reduce the number of experiments. Furthermore, mathematical modeling can exploit subtle features of experimental data such as dynamics or non-additive effects, to make deeper interpretations or stronger inferences, thus providing return for the investment of resources into modeling. Non-automated human intuition is often excellent at generating hypothetical mechanisms, but a computational approach reduces bias in selecting hypotheses, illustrates the likely outcomes of possible experiments, and refines intuitive hypotheses (*e.g.*, less binding) into quantitative components (*e.g.*, less association, more dissociation).

In this work, we used modeling and experiments to study the peak and decline of Akt Thr³⁰⁸ in serum-stimulated fibroblasts. We modeled the Akt pathway downstream of PIP3 and upstream of Akt Thr³⁰⁸ phosphorylation, and compared model simulations against available observations, including our previous time-series immune-blot of Aktp³⁰⁸ and immuno-fluorescence of PIP3. We assessed and rejected the “canonical” pathway (the null hypothesis), and then systematically generated a series of alternative hypotheses, each corresponding to a novel explanatory effect occurring at one step of the pathway. Simulations suggested informative experiments, and measurements were performed. Because our experimental observations were relative fold-change and not absolute concentrations, and because we don’t know the rates of the unknown mechanisms, we evaluated each hypothesis using a family of differently parameterized

models, and we aligned model and data according to fold-change behaviors such as peak time. Multiple hypotheses were disqualified as incompatible with observations. We conclude that the peak and decline of Akt activation is predominantly caused by recruitment or retention of Akt at the cell membrane by some factor that is PI3K-dependent but PIP3-independent.

5.2 Canonical PIP3/Akt cascade

The delay between peak PIP3 activation and peak Akt phosphorylation.

As input data for building a model of serum-stimulated Akt activation, we used previously published time-series measurements of PIP3 abundance and Akt phosphorylation in mouse embryonic fibroblasts (MEFs) (Lim and Clément, 2007). MEFs had been serum-deprived (given 0.5% FBS for 24 hours) prior to stimulation at time $t=0$ with 10% serum (FBS). In four replicates of Akt phosphorylation at Thr³⁰⁸ (Aktp³⁰⁸) time series, Aktp³⁰⁸ peaks at 30-60 minutes before declining to a steady state of activation (Figure 5.1, solid curves). Surprisingly, PIP3 activation peaked at 2 minutes (Figure 5.1 dashed curve), an order of magnitude earlier than Aktp³⁰⁸. We replicated some of the PIP3 and Aktp³⁰⁸ time-series measurements and tested additional time-points, but we continued to observe the delay between 2-5 minutes peak activation of PIP3 (Figure 5.S3). During model calibration, we will fit the Aktp³⁰⁸ simulation to mimic only the earliest of the 4 curve peaks (which is the most conservative approach).

Previous models of Akt pathway dynamics produced nearly simultaneous peaks for PIP3 and Akt phosphorylation (Hatakeyama, *et al.*, 2003; Suresh Babu, *et al.*, 2008), and to the best of our knowledge, previous models of Akt pathway dynamics have not been compared with experimental observations of PIP3 dynamics. The large time difference between PIP3 and Aktp³⁰⁸ (Figure 5.1) is intriguing considering that PIP3 is only one step away from Akt activation in the canonical PIP3/Akt cascade. Recall that

PIP3 activates PDK1 (PIP3-dependent kinase 1), by binding it and recruiting it from the cytosol to the plasma membrane. PIP3 also recruits Akt to the membrane. At the membrane, PDK1 phosphorylates Akt directly at Thr³⁰⁸ (Raimondi and Falasca, 2011). So we asked whether a standard “null hypothesis” model of Akt activation dynamics would be capable of reproducing the observed dynamics of PIP3 and Aktp³⁰⁸.

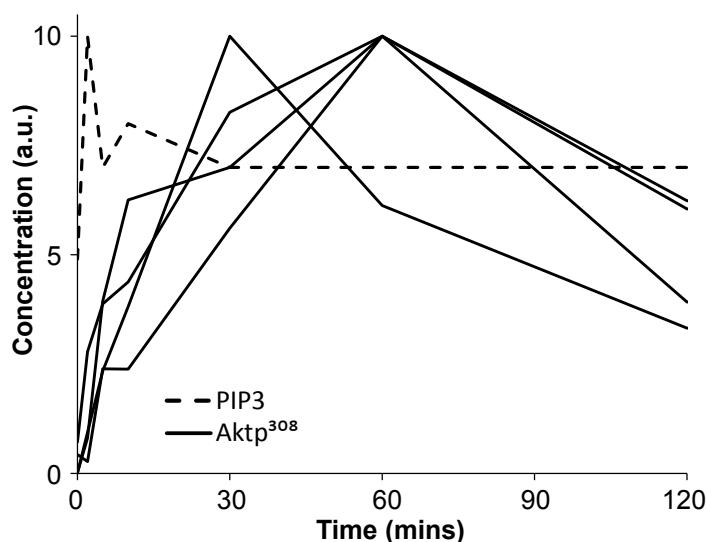


Figure 5.1 – Quantified time-series of PIP3 (dotted line) and Aktp308 (4 solid lines for 4 experimental replicates) in arbitrary units.

The densitometry of Aktp³⁰⁸ was normalized by the densitometry of total Akt, and then rescaled such that the highest level in each time-series was equal to 10.0 (for consistency with the previous model by Hatakeyama et al.) Note that the earliest of the Aktp³⁰⁸ curves peaks at 30 minutes. The first PIP3 immunofluorescence experiment was performed by Sharon Lim, NUS Department of Biochemistry, and two replicates were performed by Luo Le and the author (Appendix A1). Cells were normally grown in culture containing 10% fetal bovine serum (FBS). At 24 hours before t=0, cells were starved in culture containing 0.5% FBS. At time t=0, cells were treated with 10%FBS and measurement was performed at different timepoints after t=0. Raw data was rescaled before plotting, and rescaled data were used in model calibration.

The null hypothesis model

Although the PIP3/Akt cascade is included in some previous models (Hatakeyama, *et al.*, 2003; Suresh Babu, *et al.*, 2008), we constructed a custom model of the canonical PIP3/Akt cascade (network diagram shown in Figure 5.2A) tailored to reconciling the time difference between PIP3 and Aktp³⁰⁸ in Figure 5.1. This model, called H0, functions as our null hypothesis. The H0 model was constructed using ordinary differential equations (ODEs), where each ODE represents the production/consumption of a molecular species over time. Integrating the ODEs provides a time-evolution (a simulated trajectory) of the species abundance over time.

The reaction equations and parameters of H0 appear in Table 5.1 and Table 5.2. PIP3 levels, assumed to be a time-varying input stimulus for the system (previously adopted by (Nägele, *et al.*, 2010)) were plugged into the model by spline interpolation of the time-series data to provide a continuous curve (Figure 5.1C, dashed line). The interpolated PIP3 levels were utilized in the ODEs for the downstream species, but the PIP3 levels were not governed by the ODEs. Under different treatment conditions (see Materials and Methods), PIP3 level may be taken from different spline curves. The key output of the simulations would be Aktp³⁰⁸, the sum of membrane Aktp³⁰⁸ and cytosolic Aktp³⁰⁸.

Index	Process	Reaction velocity	Modifier	Rate constants	Reference
#1	PIP3 + PDK1 => PIP3:PDK1m	k1[PIP3][PDK1]	PIP3	k1 = 1.79	Estimation
#2	PIP3:PDK1m => PIP3 + PDK1	k2[PIP3:PDK1m]		k2 = 9.9	Estimation
#3	PIP3 + Aktc => PIP3:Aktm	k3[PIP3][Aktc]	PIP3	k3 = 5.27	Estimation
#4	PIP3:Aktm => PIP3 + Aktp ³⁰⁸ m	k4[PIP3:PDK1m][PIP3:Aktm] / (k5+[PIP3:Aktm])	PIP3:PDK1m	k4 = 2450 k5 = 68000	(Biondi, et al., 2000) (Biondi, et al., 2000)
#5	Aktp ³⁰⁸ m => Aktp ³⁰⁸ c	k6[Aktp ³⁰⁸ m]		k6 = 0.49	Estimation
#6	Aktp ³⁰⁸ c => Aktc	k7[Phosphatase] [Aktp ³⁰⁸ c] / (k8+[Aktp ³⁰⁸ c])	Phosphatase	k7 = 5 k8 = 1.65	Estimation Estimation

Table 5.1 – Reactions and rate constants used in the H0 model.

The “process” column describes conversion from substrates to products. Modifier: the enzymes (PIP3:PDK1m, Phosphatase) or the recruiter (PIP3). Reaction velocity: the speed which the reaction takes place, which may depend on some modifiers. Rate constants: values of the reaction rates used. Reference: the source of the rate constant values, or “Estimation” if the values were allowed to be optimized.

Species	Initial concentration	Optimized?
PIP3	Input	No
PDK1_total	10	No
PDK1	9.75	Yes
PIP3:PDK1m	0.25	No
Akt_total	10	No
Aktc	9.988	Yes
PIP3:Aktm	0.001	Yes
Aktp ³⁰⁸ _m	0.001	Yes
Aktp ³⁰⁸ _c	0.01	No
Aktp ³⁰⁸	Aktp ³⁰⁸ _m + Aktp ³⁰⁸ _c	No
Phosphatase	0.24	Yes

Table 5.2 – Initial concentrations of the species used in the H0 model.

Species: name of the species in H0. *Initial concentration*: initial concentration values used in the model, where PIP3 value is taken from measured data as "Input", and Aktp³⁰⁸ is the sum of Aktp³⁰⁸_m and Aktp³⁰⁸_c. "Optimized": whether the values were subjected to optimization process.

Parameters were adjusted to maximize agreement between simulations and observations, for multiple experimental treatments. We required the same reaction rates and initial concentrations to be used when fitting multiple experimental treatments, because the treatments were performed on the same cell type. All model parameters were constrained such that every species started at its un-stimulated steady state (*i.e.*, when nothing is added at $t=0$). The binding rate of PIP3:PDK1m to PIP3:Aktm was derived from (Biondi, *et al.*, 2000; Hatakeyama, *et al.*, 2003). The binding rate of PIP3 to Aktc and that of PIP3 to PDK1 were allowed to be different. Finally, based on the observation that PDK1 and Akt have undetectable levels at the membrane in serum-deprived cells (Lim and Clément, 2007), we required that the initial state of the system must have all PDK1 and Akt in the cytosol. The H0 model was fit to the observations (Figure 5.1C) using a multiple fitting approach. Both global search (particle swarm optimization) and local search (Nelder-Mead) methods with multiple initial starts were used (Kennedy and Eberhart, 1942; Nelder and Mead, 1965).

Rejection of the null hypothesis

As there are unknown parameters in the H0 model, we considered a family of different models, each containing the same set of ODEs as in Table 4.1, but with different values for the model parameters. Extensive efforts to fit the H0 model family to the observed Aktp³⁰⁸ measurements were unsuccessful, suggesting that there was no instance of H0 model that recapitulates the observed dynamics of Aktp³⁰⁸ with the given PIP3 data as input. Among the 200 optimized models, the top 20 models for H0 family (ranked based on sum-of-square difference with data) were simulated (Figure 5.2B, solid black curves) and compared with measured Aktp³⁰⁸ time-series (Figure 5.2B, dashed red curve). Each model in the H0 family may contain different values for the kinetic parameters, derived from the reaction equations of H0 combined with multiple independently optimized rate parameters.

Compared with the observations for Aktp³⁰⁸, simulation of the H0 model was unable to produce a slow rise and a late decline of Akt activation producing a peak at 30 minutes and the assortment of simulated trajectories contains no match with the observed concentration profile. There are some simulations of peak and decline, but they are early, mirroring the early peak and decline of PIP3 at 2 minutes. We interpret these experiments to mean that the downstream effects of PIP3 are insufficient to explain the dynamics of Aktp³⁰⁸. Dynamics of Aktp³⁰⁸ in response to that of PIP3 is at the heart of the Akt pathway and we focus narrowly on this phase of the cascade for the remainder of the paper. We henceforth use observations of PIP3 as input, and build models that seek to explain Aktp³⁰⁸ as output.

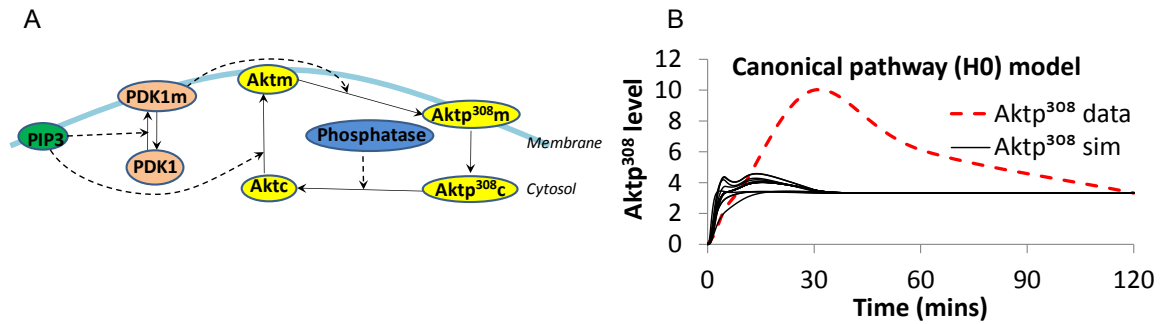


Figure 5.2 – The canonical model of Akt activation.

(A) Network diagram for H0 (canonical pathway) model family and (B) Time course simulation of the best-fit models for H0 compared with measured Aktp³⁰⁸ time-series. All simulated time courses were normalized to have the same concentration at $t=120\text{min}$. The assumptions used in constructing the model, how the kinetic parameters were estimated and how simulations of the model were performed are described in materials and methods. The phosphatases capable of dephosphorylating Aktp³⁰⁸ are represented by a single entity Phosphatase in the model.

5.3 Non-canonical mechanisms for Akt activation

Non-canonical causes of altered Akt localization

In normal cells, the majority of Akt is in its inactive form at the cytosol (Lim and Clément, 2007). The canonical PIP3/Akt cascade describes the well-studied recruitment of Akt to the membrane by the membrane lipid PIP3. The lesser known mechanisms of altering Akt localization are described below.

A number of other factors have been reported to directly or indirectly alter the localization of Akt at the membrane. H-ras and Rac1 were reported to induce Akt translocation to the membrane (Yang, *et al.*, 2012). The PAK1 kinase domain was found to function as a scaffold to facilitate Akt stimulation by PDK1 and to aid recruitment of Akt to the membrane (Higuchi, *et al.*, 2008). The TNF receptor associated factor 6 (TRAF6) protein was found to be a direct E3 ligase for Akt and was essential for Akt membrane recruitment and phosphorylation upon growth-factor stimulation (Yang, *et al.*, 2009). Gao *et al.* and Lasserre *et al.* report that Akt activation is mediated by raft and membrane microdomain compartmentalization (Gao, *et al.*, 2011; Lasserre, *et al.*, 2008). While not affecting the localization of Akt, p38alpha can induce re-localization of PP2A to the membrane, leading to dephosphorylation and inhibition of Akt phosphorylation (Zuluaga, *et al.*, 2007). The membrane-bound complex Freud-1/Aki1, when stimulated by

EGF, was able to induce the formation of a PDK1/Akt complex and thus regulated Akt activation in a concentration-dependent biphasic manner (Nakamura, *et al.*, 2008). All Akt recruitment factors above are non-canonical and have not been as well studied as PIP3. However, this body of literature motivates us to consider non-canonical mechanisms which might be capable of explaining the canonical PIP3/Akt pathway fails to explain the peak time difference between PIP3 and Aktp³⁰⁸.

Non-canonical causes of altered Akt phosphorylation dynamics

With the increased understanding of Akt activation mechanisms, many studies have discovered many signaling molecules that affect both the duration and magnitude of membrane Akt phosphorylation. Prolonged Akt activation is increasingly found to be an important factor in for cells to perform many signaling functions. The duration of Akt activation is known to work by regulating the dephosphorylation (Brognard and Newton, 2008; Brognard, *et al.*, 2009; Rocher, *et al.*, 2007; Zhang and Riedel, 2009). When nutrients are limiting, Akt signaling is intensified and prolonged due to the blockage of mTOR activation and the release of Akt from p70S6K-dependent inhibition (Plas and Thompson, 2005). Mutant forms of PI3K catalytic subunit and mutations in PTEN might result in modified abundance of PIP3, promoting an increase in the strength or duration of Akt-activating signals (Zhang, *et al.*, 2011). The inhibition of the p38/MAPK pathway leads to an amplification of the magnitude and duration of the PI3K/Akt pathway (Heit, *et al.*, 2002). In human mammary epithelial cell, knocking down INPP4B or PTEN has a significant effect on the magnitude and duration of insulin-stimulated Akt activation (Gewinner, *et al.*, 2009).

Some recent studies are starting to pay attention to the signaling molecules that may directly alter the duration of Akt activation, which may further our current understanding of the important kinase. Brognard and colleagues reported that the

depletion of PHLPP2 significantly prolonged the duration of Akt phosphorylation (Brognard and Newton, 2008; Brognard, *et al.*, 2009). However, the two isoforms PHLPP1 and PHLPP2 were found to have differential activity to attenuate the duration of Akt signaling (Zhang and Riedel, 2009). Liu *et al.* showed that MyCF may interfere with regulation of the duration of Akt activation or signaling (Liu, *et al.*, 1998). In astroglial cells, the duration of Akt activation was much more abbreviated in response to streptozotocin compared to glucosamine (Matthews, *et al.*, 2007). The treatment of the growth factors NGF and PDGF produced equivalent maximal activation of Akt relative to IGF-1 and insulin but of shorter duration (Habib, *et al.*, 1998). In retinal progenitor cells treated with both Epo and insulin, while the total amount of Akt phosphorylation remained unchanged, the duration of Akt phosphorylation was prolonged compared to that of Epo alone (Sanghera, *et al.*, 2011). Rocher *et al.* reported that the early response gene IEX-1 prolonged the activity of Akt by inhibiting the direct dephosphorylation of Akt by the PP2As (Rocher, *et al.*, 2007). Liu *et al.* reported that phorbol 12-myristate-13-acetate (PMA) reduced Akt phosphorylation duration from 90 minutes down to 15 minutes in myeloid 32D cells (Liu, *et al.*, 2006). In HepG2 cells, the combined “heat shock + mild electrical stimulation” treatment extended the duration of Akt phosphorylation through an increase of Hsp72 expression (Morino, *et al.*, 2008). Finally, Yoon and colleagues reports that selenite maintained the duration of the activation of PI3-K/Akt pathways for at least 48h, much longer than that of growth factors and other stress factors (Yoon, *et al.*, 2002). This stream of evidence suggests that many factors exist to alter the dynamics of Akt activation, and many of them may be non-canonical.

Systematic generation of alternative scenarios

The failure of the canonical PIP3/Akt pathway to explain the peak time difference between PIP3 and Aktp³⁰⁸ (see Section 4.2) necessitated the quest for alternative

explanations. To obtain maximum coverage and generality, we considered different hypotheses affecting the same step in the pathway (Figure 5.3A). Each hypothesis contains the canonical pathway with the addition of a hypothetical “pseudo-species”. This approach demonstrated two main components of the CHEGS common techniques: systematic evaluation of alternatives and sacrificing complexity for generalizability.

Some proteins and complexes were found to recruit Akt to the membrane (Higuchi, *et al.*, 2008; Nakamura, *et al.*, 2008; Yang, *et al.*, 2009), justifying the introduction of a hypothetical “recruitment factor” in recruitment model. Akt was known to have different states depending on the environments (Murata, *et al.*, 2003), and thus we hypothesize that one state of Akt is trapped at the membrane (retention model). PP2A, a phosphatase of Akt, was found to have differential activity under normal environment and under oxidative stress (Foley, *et al.*, 2007), and hence we hypothesize that one state of Phosphatase is inaccessible to Akt (dephosphorylation model). There is not much literature evidence suggesting that the phosphorylation activity of PDK1 is regulated by external factors, but a model for this scenario was constructed for the purpose to complete coverage of all alternatives.

Starting with five steps of the pathway (Figure 5.3A) corresponding to five alternative hypotheses, we immediately discarded the hypothesis of perturbed PDK1 recruitment to the membrane (“PDK1 recruitment”), based on previous time-series measurements of membrane PDK1 (Luo, 2011). PDK1 recruitment dynamics were a close mirror of the PIP3 dynamics (peaking at 2-5mins), indicating no non-canonical effect modifying or delaying the dynamics of PDK1.

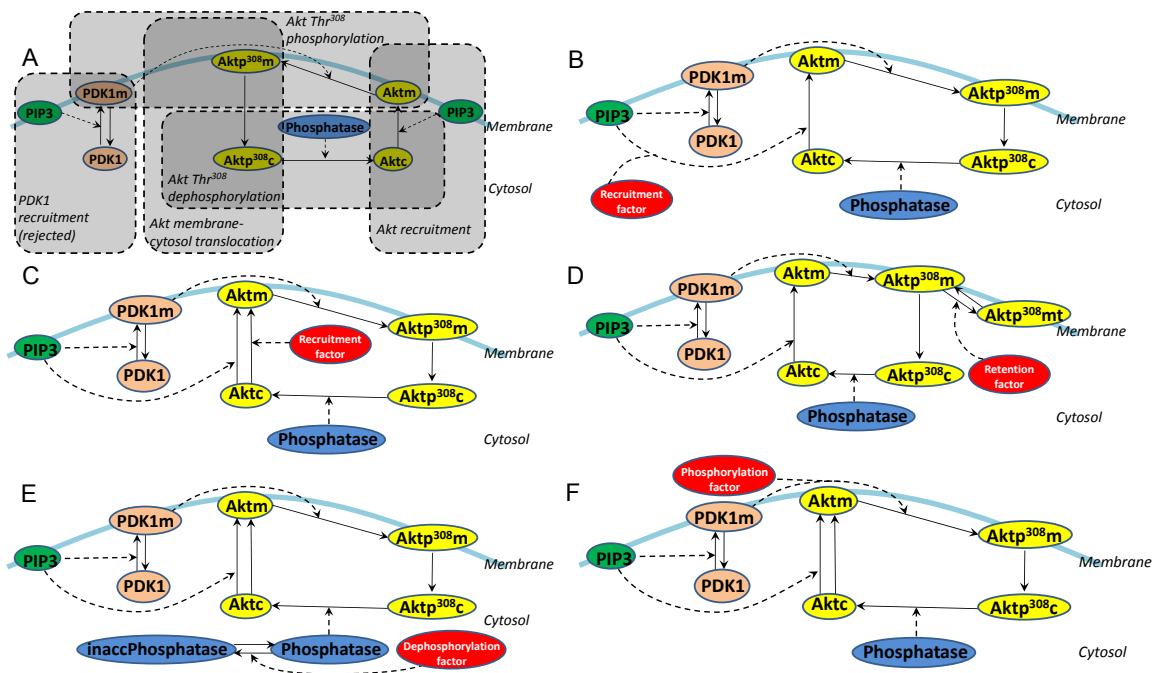


Figure 5.3 – Five alternative hypotheses, each with one non-canonical effect (in red).
 (A) Systematic investigation of the pathway for unknown effect. Five events (dashed boxes) in the canonical PIP3/Akt cascade were identified: PDK1 recruitment, Akt recruitment, Akt Thr^{308} phosphorylation, Akt membrane-cytosol translocation and Akt Thr^{308} dephosphorylation. One event (PDK1 recruitment by PIP3) dashed gray box) was considered unlikely to be regulated by external effects, due to our measurement of membrane PDK1 time-series. The systematic investigation generates five models (each corresponding to one hypothesis) to reconcile the discrepancy between PIP3 and Akt 308 : (B) PIP3-dependent recruitment model (C) PIP3-independent recruitment model, (D) retention model, (E) dephosphorylation model, and (F) phosphorylation model. In recruitment models, a “recruitment factor”, dependent or independent of PIP, alters the rate of PIP3-induced Akt translocation from cytosol to membrane. In retention model, a “retention factor” prevents dissociation of Akt from the membrane after phosphorylation. In dephosphorylation model, a “dephosphorylation factor” disrupts the interaction between cytosolic Akt 308 and its phosphatases. In phosphorylation model, a “phosphorylation factor” enhances the catalytic activity of PDK1 to phosphorylate membrane Akt.

There could potentially be some non-canonical perturbation at any of the remaining 4 steps of the canonical PIP3/Akt cascade in Figure 5.3 (Akt recruitment, Akt Thr^{308} phosphorylation, Akt membrane-cytosol translocation, and Akt Thr^{308} dephosphorylation). We do not know the exact molecular mechanism that would cause each hypothetical perturbation, so we cannot model potential perturbations with explicit enzyme kinetics. Instead, we constructed an arbitrary spline curve to represent any hypothetical perturbation effect over time. The shape of the spline curve can later be optimized for the model to fit the observed trends (the “reverse fitting pipeline”, Figure 5.4). For each potential scenario, the hypothetical effect was represented as an input to the system, whose value was obtained from a linear spline. The spline was constructed by linearly interpolating between the knots, which became part of the system’s parameters

for optimization. The dynamics of this input was obtained based on the optimized spline knots (see Section 2.3). In other words, optimizing the perturbed model to fit the data would solve for the shape of the spline curve, which tells us when the perturbation would occur.

We constructed the alternative models by adding a pseudo-reaction (spline curve) at the appropriate step of the pathway. Since “Akt recruitment” may or may not require PIP3, we build two mechanisms for perturbing this step (Figure 5.3B-C). For each of the remaining 3 steps, one alternative hypothesis was constructed (Figure 5.3D-F).

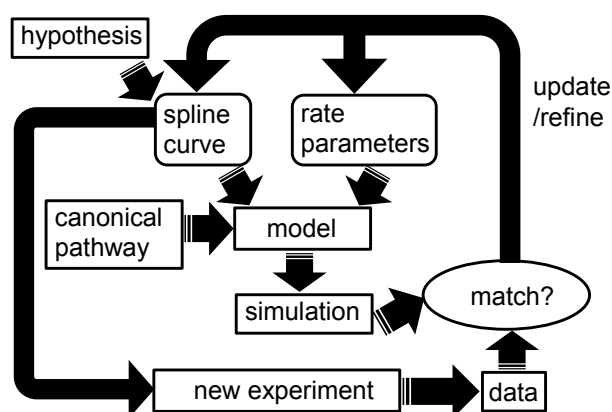


Figure 5.4 – Flowchart describing the reverse-fitting method used in this study. Each hypothesized perturbation was encoded as a pseudo-species with a spline curve for its time series profile. Rate parameters for biochemical reactions and the spline curve were optimized simultaneously, to fit data. Finally, models improve subsequent experiments by predicting when hypothetical effects would achieve peak effect, or by rejecting unlikely hypotheses.

Note that the pseudo-reaction should not be misinterpreted as representing a true biochemical mechanism; it is only an interface between the differential equations of the canonical pathway, and the spline curve for the dynamic of the perturbation. The alternative hypotheses (Figure 5.3B-F) were constructed based on previous evidence whenever possible, and the hypothetical effects were introduced systematically to each reaction of the H0 model. To maximize the generality of the representation, we use a reaction-like process to describe the unknown perturbation that might occur at each step of the pathway. A more conventional approach would have been to construct an artificial molecule and hypothesize its parameters, but we rejected this approach because it can

give an artificial appearance of validity to the cosmetic implementation of the perturbation. We utilize instead a time-dependent process (in the form of a linear spline) because it creates greater emphasis on delineating when an unknown event reaches its peak. We then computed the spline knots to derive what perturbation would have to occur to the hypothesis in question, such that including this perturbation would suffice to explain Aktp³⁰⁸ based on PIP3 input.

5.4 Membrane fractionation dynamics

Model predicts non-trivial dynamics of membrane fractions

Using the same fitting procedure that had been applied to the H0 model families, all five model families with additional hypothetical effect could match the dynamics of Aktp³⁰⁸ equally well (Figure 5.5A). This necessitates acquiring additional data for model calibration, in an attempt to single out a scenario that is more likely to happen in cells than other scenarios. Simulation of membrane PDK1 (Figure 5.5B) did not show a clear distinction between different models, suggesting that measuring this time-series may not provide useful information for discriminating between the alternative hypotheses. In contrast, simulation from four alternative models revealed non-trivial dynamics of membrane total Akt and membrane phosphorylated Akt (Figure 5.5C-D), which motivated the measurement the two time-series.

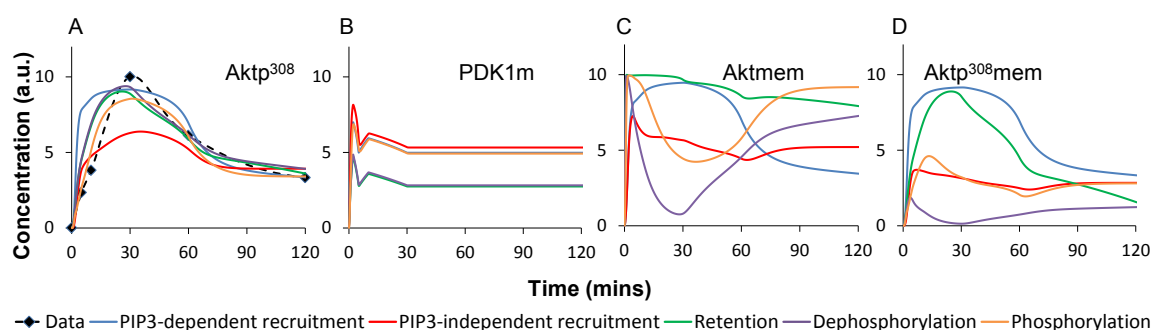


Figure 5.5 – Time course simulations of the five alternative models.

(A) Aktp³⁰⁸, (B) membrane PDK1, (C) membrane total Akt, and (D) membrane Aktp³⁰⁸. Model predictions suggested measurement of membrane total Akt and membrane phosphorylated Akt may help discriminate between alternative hypotheses.

Membrane fractions time-series

Fractionation experiments were performed to obtain the time-series membrane fractions of Aktp³⁰⁸, total Akt and PDK1 (Figure 5.6). We summarize the major peaks from the fraction time-series as follow: the PDK1m level (solid curve) peaks at 2 minutes and quickly decreases to near its un-stimulated (t=0) level by 60 minutes; the membrane total Akt level (dashed curve with diamond markers) peaks at 5 minutes and stays high until 30 minutes before decreasing; and the membrane Aktp³⁰⁸ level (solid curve with triangle markers) peaks at 30 minutes with a minor peak at 5 minutes. These time-series fractionation measurements indicate that Akt is present at the membrane for a prolonged period of time after the PIP3 levels have increased and decreased. We interpret this to mean that the delayed activation of Aktp³⁰⁸ in total cell lysate is contributed by the delayed activation of membrane Aktp³⁰⁸.

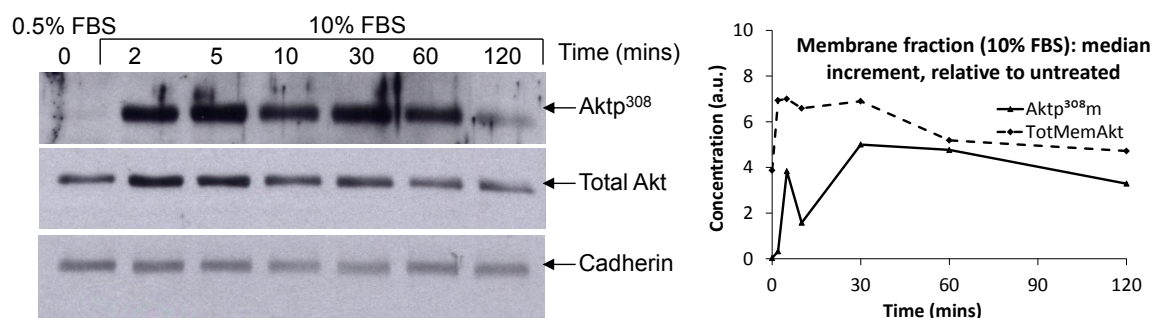


Figure 5.6 – Time-series western blot fractionation experiments.

Fractionation experiments (performed by Luo Le, NUS Department of Biochemistry) of the membrane fraction of total Akt (Akt mem) and Aktp³⁰⁸ (Aktp³⁰⁸ mem). Methods and Materials for the experiments can be found in Dr. Luo Le's thesis, Section 2.2. Quantification was performed based on western blot densitometries from at least three replicates. The time-series were measured in fold-changes compared to un-stimulated state (t=0). Aktp³⁰⁸ measures were taken from Aktp³⁰⁸ at t=0 plus median increments from 3 replicates. Measures of total Akt were taken from total Akt at t=0 plus median increments from 6 replicates (measured in fold-change). Due to the use of median measures, error bars are not applicable to the plots, but complete datasets are available at the project webpage (<http://webbippe.nus.edu.sg:8080/Akt>). The curves were arbitrarily scaled and offset such that the concentration of Aktp³⁰⁸ is always less than that of total Akt, and the data is of the same scale as the arbitrary units being used in the alternative models. The dynamics observed in the right plot was produced by at least three replicates. Numerical values for normalization procedures can be found at the project webpage.

5.5 Model analysis with additional membrane fraction time-series

Model re-calibration using additional membrane fraction time-series

Based on the total cell lysate time-series and the additional membrane fraction data, we performed model fitting to assess the ability of each alternative hypothesis to recapitulate the measured dynamics. Simulated time-course from optimized model in each hypothesis was compared with time-series data in total cell lysate Akt^{p308} (Figure 5.7A-J, blue curves) and membrane fraction experiments (Figure 5.7A-J, red, green and purple curves).

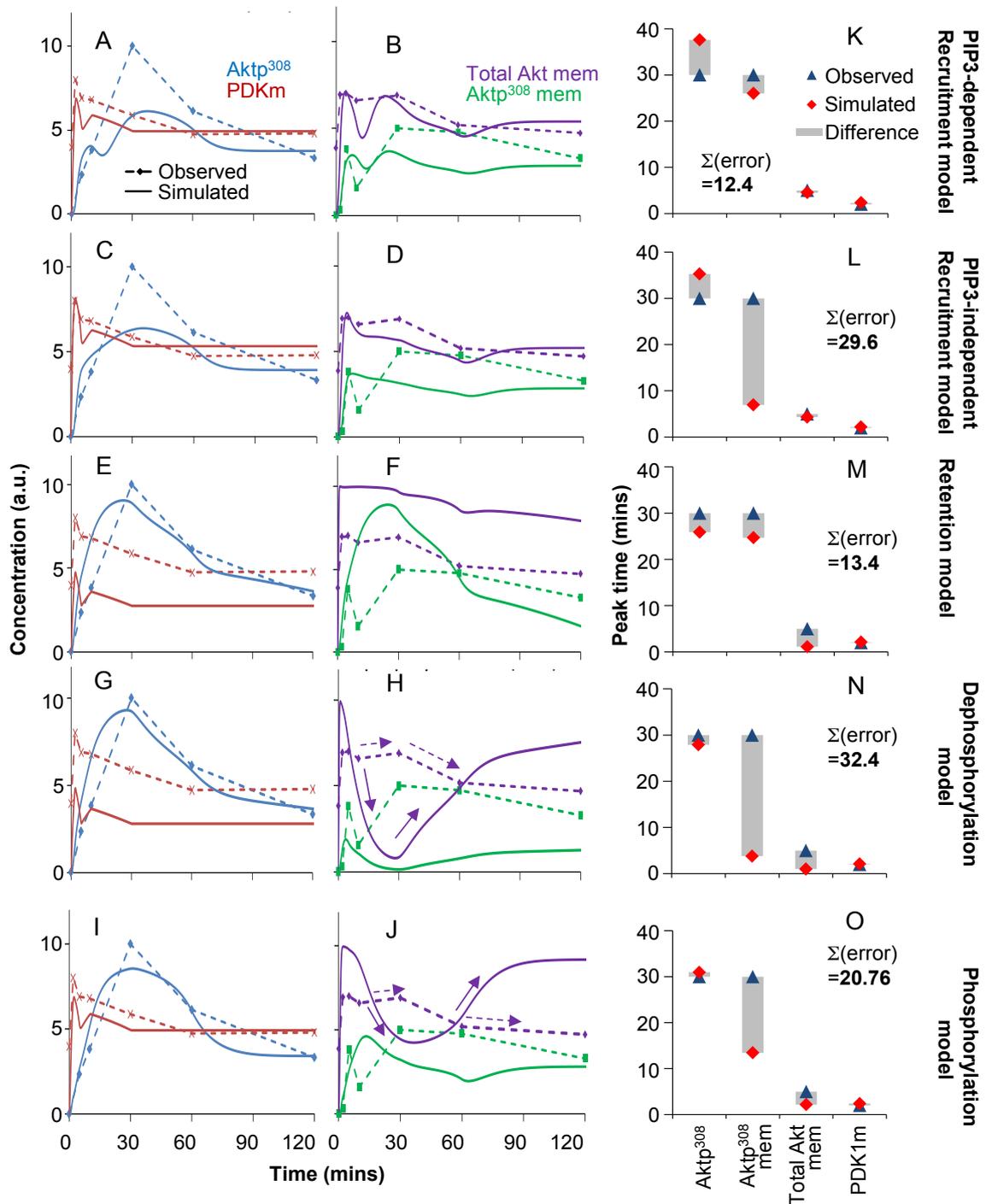


Figure 5.7 – Comparison between experimental time-series and simulated time courses.

Evaluation was performed for PIP3-independent recruitment model (A-B), PIP3-dependent recruitment model (C-D), retention model (E-F), dephosphorylation model (G-H), and phosphorylation model (I-J). The following species were compared and contrasted: total cell lysate Aktp³⁰⁸ (blue curve), membrane PDK1 (red curve), membrane total Akt (purple curve), and membrane Aktp³⁰⁸ (green curve). (A-J) Solid line represented simulation and dashed line represented measurements. All dynamics were measured in relative concentration (arbitrary unit). Criteria for match include the ability of simulated time course to reproduce the peak time, peak duration and peak amplitude of measured time-series, in the order of importance. The following simulation-data pairs were considered poor matches: (H) purple curves, and (J) purple curves, due to the dynamic mismatch shown by the purple arrows. The green curves in (F), (H) and (J) were considered partial matches. (K-O) Peak time of each model was compared with peak time of data and the difference is highlighted by gray bar. $\Sigma(\text{error})$: sum of all differences (gray bars).

A good fit was determined by the sum-of-square error (SSE) score between simulated and measured time-series. However, as data was arbitrarily scaling and offset was applied to data quantification, requirement of absolute timepoint-by-timepoint match between simulated and measured time-series would be unnecessary. We instead evaluated a match based on its peak properties: peak time, peak duration (width) and peak amplitude. Note that peak timings are not affected by scaling and offset. Based on the numerical values for peak difference and by manually observing the curve dynamics in Figure 5.7, we define the following three categories of comparison outcomes: plausible match (matching peak times and rise-and-decline dynamics), partially plausible match (mismatching peak times but agreeing in most rise-and-decline dynamics), and implausible match (failing both criteria). The curve pairs classified as partially plausible or implausible match are described in the caption of Figure 5.7.

Our previous work (Nim, *et al.*, 2010) suggested that the Akt model might contain high complexity and the objective function landscape might be rugged with multiple local minima. This prevents any standalone parameter estimation method from delivering satisfactory agreement between simulation and measurements, and model calibration tasks required broad and repeated sampling of the parameter space. Indeed our early attempts to fit the models with the data were unsuccessful, and we subsequently employed a multi-step strategy for model calibration. In this multi-step method, a collection of fitted models were obtained from global optimization (particle swarm optimization), manual fitting was performed to pick out the potential candidates based on ability to match peak timings of measured time-series, and local optimization (Nelder-Mead method) was performed as the last step to refine the parameters.

As observed in Figure 5.7A-B, the PIP3-dependent recruitment model was able to reproduce all four sets of dynamics in the serum-stimulated MEF. In simulations of this

model (Figure 5.7B purple solid curve), the “recruitment factor” augmented the amount of Akt recruited to the membrane, generating a second peak at 30 minutes. While measured membrane total Akt time-series of did not display this 2-peak dynamics dramatically (Figure 5.7B, purple dashed curve), it showed that membrane total Akt level was high at both 5 minutes and 30 minutes, in agreement with the computed dynamics. The 2-peak dynamics of membrane total Akt created a similar 2-peak dynamics of membrane Aktp³⁰⁸, which was observed in membrane Aktp³⁰⁸ measurement. In summary, the PIP3-dependent recruitment model showed a strong resemblance to the data.

The PIP3-independent recruitment model, similar to the PIP3-dependent recruitment model, showed a reasonable match between PIP3-independent recruitment model and time-series data (Figure 5.7C-D). In this model simulation, the 2-minute peak of PIP3 created a similar 2-minute peak of membrane PDK1 (Figure 5.7C, red curves), in agreement with data. This PDK1m peak was delayed to 30 minutes when propagated to membrane Aktp³⁰⁸ (Figure 5.7C, blue curves), in agreement with the 30-minute peak of data. Model simulation also exhibited a peak at 2 minutes and a prolonged high level of membrane total Akt (Figure 5.7D, purple curves) from 2-60 minutes, similar to the observed trend. The peak at 30 minutes from observed membrane Aktp³⁰⁸ time-series (Figure 5.6D, green curves) was not recapitulated by simulation, but the difference is not strong enough to reject the PIP3-independent recruitment model. In summary, the PIP3-independent recruitment model showed an adequate resemblance to the data.

In retention model, simulation showed that membrane total Akt level stays high upon recruitment (Figure 5.7F, purple solid curve). Under this condition, the level of Aktp³⁰⁸ was able to reach a high level at 30 minutes (Figure 5.7F, green curve) before the retention effect decreased and allow more Aktp³⁰⁸ to reach the cytosol and be dephosphorylated. Thus the simulated membrane Aktp³⁰⁸ dynamics was able to capture

the peak at 30 minutes of observations, albeit with a much stronger peak. This led us to conclude that the retention model was inferior to the PIP3-independent and PIP3-dependent recruitment models evaluated by agreement with membrane fraction time-series. In summary, the retention model showed a good match to the data.

While the dephosphorylation model was able to match the total cell lysate Aktp³⁰⁸ data (Figure 5.7G), it exhibited irreconcilable mismatch with membrane fraction measurements (Figure 5.7H). Under this scenario, the inaccessibility of cytosolic phosphatases (“Phosphatase”) created an augmented level of cytosolic Aktp³⁰⁸ which produced a peak at 30 minutes (data not shown) leading to the similar 30-minute peak of total cell lysate Aktp³⁰⁸. However, this effect led to a dramatic decrease of membrane total Akt from 2 minutes (Figure 5.7H, purple solid curve, marked with arrows) and membrane Aktp³⁰⁸ from 10 minutes (Figure 5.7H, green solid curve), both of which contradicted the measured dynamics. In summary, the dephosphorylation model did not adequately resemble the data.

Finally, the phosphorylation model was also able to match two data series (Figure 5.7I). However, this model failed to reproduce the dynamics of membrane total Akt (Figure 5.7J, purple curves) and has partially plausible match with the dynamics of membrane Aktp³⁰⁸ (Figure 5.7J, green curves). It should be noted that the dynamic behavior of the phosphorylation model shared some similarity with the dephosphorylation model. Thus, similar to the dephosphorylation model, the phosphorylation model also did not adequately resemble the data.

We next compared between the peak time of the simulated and observed time course, highlighted the mismatch by grey bars (Figure 5.7K-O). While the PIP3-dependent recruitment and retention models displayed good agreement in terms of peak time (total error = 12.4 and 13.4, respectively), the phosphorylation, PIP3-independent

recruitment, and dephosphorylation models exhibited poor agreement especially with respect to membrane Aktp³⁰⁸ (total error = 20.76, 32.4, and 29.6 respectively). By also taking into account the comparison results with measured membrane total Akt and membrane Aktp³⁰⁸ time-series into account, the dephosphorylation model (Figure 5.7H) and phosphorylation model (Figure 5.7J) had much poorer agreement compared to the PIP3-independent recruitment model (Figure 5.7D). By failing in both categories, the dephosphorylation and phosphorylation models were both rejected as not being supported by the membrane fractionation measurements.

Model prediction of PIP3 inhibition experiments

From the model calibration results earlier (Figure 5.6), three remaining models were not disqualified based on dynamics comparison with membrane fraction time-series measurement: PIP3-dependent recruitment, PIP3-independent recruitment and retention models. We next performed PIP3-blocked simulation experiments using these three models and asked whether the predicted results of PIP3 knockdown, according to the three remaining hypotheses, would be different enough so that doing this experiment would allow at least one hypothesis to be excluded by the results.

We simulated the three remaining models under the two treatments: a control treatment where cells were stimulated by serum as in previous experiments, and a PIP3-blocked treatment where PIP3 concentration is constant over time. When PIP3 was blocked, two of the models (the PIP3-dependent recruitment and the retention model) showed dramatic change where the peak of membrane total Akt was obliterated (Figure 5.8A, B, and C). The remaining PIP3-independent model (Figure 5.8C, dashed red curve marked with black arrow) showed that membrane total Akt level still increase rapidly to peak at 30min.

Based on model simulations (Figure 5.8C), we proposed to measure total membrane Akt dynamics, using a PIP3-specific inhibitor in addition to 10%FBS treatment at time $t=0$. Measurement of Aktp³⁰⁸ in total cell lysate or other protein may not be beneficial in discriminating among three alternative hypotheses (Figure 5.8A, B, and D). If this experiment showed non-trivial dynamics similar to simulated dynamics of membrane total Akt under PIP3-independent recruitment hypothesis, two hypotheses (PIP3-dependent recruitment and retention) can be disqualified, greatly reducing the number of alternatives. On the other hand, if the measured dynamics showed a flat trajectory, this could be used as a basis to reject the PIP3-independent recruitment hypothesis, narrowing the number of possibilities in our study. However, it should be taken into consideration that PIP3-blocked experiments may also have practical constraints, including the lack of PIP3-specific inhibitors.

This PIP3-blocked experimental design may not be obvious from manual observation of previous measurements. A PIP3-independent Akt recruitment effect might recruit Akt to membrane and not activate it, because there might not be enough active PDK1 available. The relative availability of PDK1 relative to membrane total Akt is uncertain and other members of the hypothesis family might predict otherwise. But there exist parameter values for the PIP3-independent recruitment model, in which Akt would not get activated after PIP3 is blocked. In other words, all the hypotheses would show the same behavior towards Aktp³⁰⁸ in total cell lysate. On the other hand, the fractionation would show Akt recruitment which would always differ between the PIP3-independent recruitment and PIP3-dependent recruitment hypotheses under the PIP3-blocked condition.

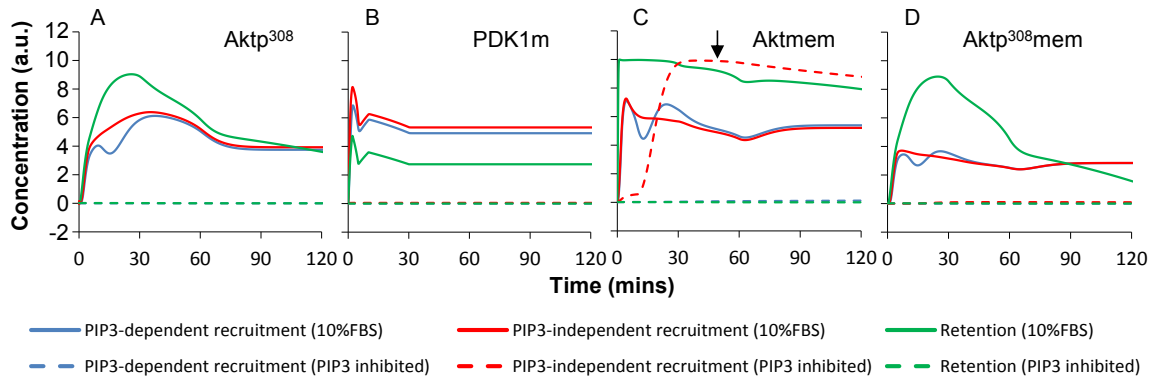


Figure 5.8 – Time course simulation of three candidate alternative models.

(A) $Aktp^{308}$, (B) membrane PDK1, (C) membrane total Akt, and (D) membrane $Aktp^{308}$ from three alternative models: PIP3-dependent recruitment, PIP3-independent recruitment, and retention. Treatment conditions in simulation include: 10%FBS (control) and PIP3 inhibition+10%FBS at time $t=0$. Model predictions suggested that membrane total Akt (black arrow) has non-trivial dynamics under the PIP3-independent recruitment hypothesis.

5.6 Model ensemble analysis

With the complexity and potential lack of well-defined minima in the alternative models, it was possible that multiple models within each alternative hypothesis could match data equally well. Modeling studies such as by Chen *et al.* have considered multiple fits for evaluation model behavior rather than relying on a single best model (Chen, *et al.*, 2009). Following this approach, we proceeded to evaluate a broad spectrum of individuals belonging to each model family.

We defined a feature vector called the “peak vector” which is a simplified representation of the dynamics of each trajectory, based on the properties of the highest peak in all species time course. In this current system, the peak vector is a 12-dimensional vector consisting of peak time, peak amplitude and peak width (illustrated in Figure 5.9A) of the four species that were measured in time series. All peak vectors obtained from simulation were divided by the peak vector from the measured time-series of the corresponding species. In each model family, each of the 26 nominal parameters (*i.e.* best estimates from the optimal recruitment or retention model obtained by multiple-fitting described in the previous sections) was one-at-a-time doubled or halved, generating additional 52 slightly modified individuals surrounding the optimal model (*i.e.* model with nominal parameters). The normalized peak vectors computed from these model

simulations (solid thin lines) were plotted alongside the peak vector of the measured time-series (dashed thick line) in Figure 5.9B-D.

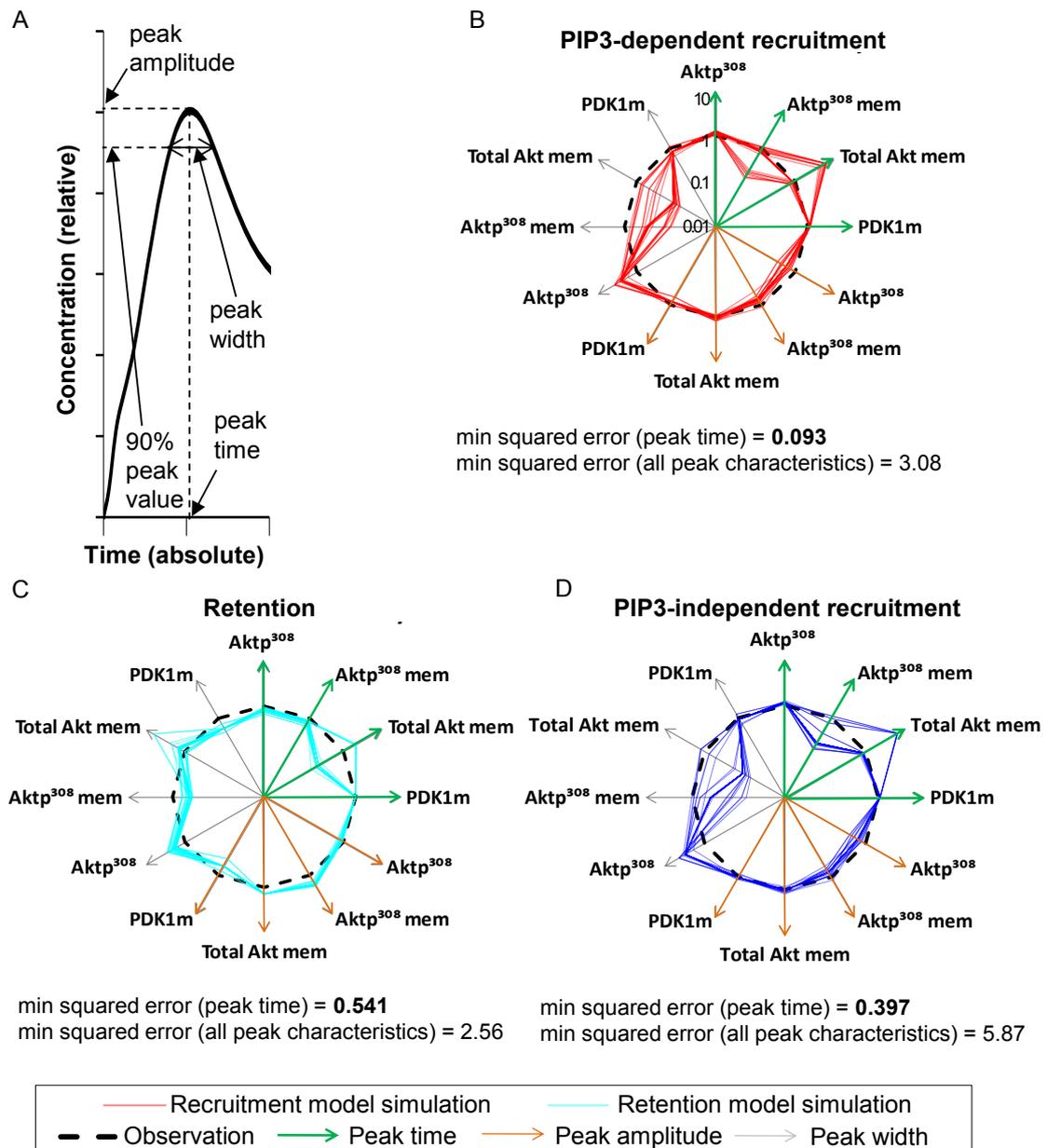


Figure 5.9 – Model ensemble analysis of three candidate alternative models.

(A) A diagram illustrating the definitions of the peak properties. Peak width is defined as the difference between the times when the level reaches 90% of the peak value in the time course. (B-D) A novel visualization scheme for displaying a multi-factorial comparison between an experimental dataset and a family of models. In these comparisons, 3 peak properties are used for comparing each of 4 measured species ($3 \times 4 = 12$ axes). In each radar chart plot, four green axes indicate the peak times of the four measured species. Four brown axes indicate the peak amplitude and four gray axes indicate the peak width of the four measured species. The thickly dashed black circle indicates the peak vector of measurements, which is normalized to a unit vector. Multiple individuals of (B) PIP3-dependent recruitment, (C) retention, and (D) PIP3-independent model families (53 models per family) were compared with respect to the 12-dimensional peak vectors. Each model family contains the nominal parameters with one parameter doubled or halved. Peak time, peak amplitude and peak width were grouped into arcs of the circle marked by solid, dashed and dotted double-headed arrows. Each arc contains four axes corresponding to the four measured time-series. All peak vectors from simulation (solid thin lines) were normalized with respect to the peak vector from measured data (dashed thick lines) before plotting. Min squared error: minimum sum of squared error, evaluated using 4 either peak times or all 12 peak characteristics within each model ensemble.

If all peak characteristics are considered equally important, the retention model family (minimum squared error = 2.56) would rank slightly higher than PIP3-dependent recruitment model family (minimum squared error = 3.08), and both are much better than the PIP3-independent recruitment model family (minimum squared error = 5.87). However, if peak time (green arrows) of each measured time-series is considered the most important property, it can be observed that some individuals of recruitment model could match all four measured peak times (minimum squared error = 0.093). In comparison, no individuals of the retention model family (minimum squared error = 0.541) or PIP3-independent recruitment model family (minimum squared error = 0.397) could match the peak time of measured membrane total Akt.

The PIP3-independent recruitment model has bad agreement with the membrane Aktp³⁰⁸ peak time, but that alone was considered insufficient to disqualify it because the simulated time course matched a second peak in the experimental observation of membrane Aktp³⁰⁸. However, another reason why PIP3-independent hypothesis is ranked low by the score is that multiple species having poor agreement with the peak width (Figure 5.9D, gray axes). It is an interesting observation that this hypothesis family can match either one peak time or another peak time but not both (Figure 5.9D, green axes). We observe that this type of diagram gives an intuitive display of this either-or contradiction, and we hope future work in pathway modeling will consider reuse of this visualization approach.

The variation among members of each model family indicates the landscape ruggedness of the peak vector around the nominal parameters. Variation within both PIP3-dependent recruitment is high (Figure 5.9B) but some of the individuals have good agreement with measurements, implying that this locality in the parameter landscape is rugged with some deep minima. In comparison, the retention model family and PIP3-

independent recruitment model family (Figure 5.9B-C) showed a lower variation level where all individual peak vectors have almost equal values in all dimensions except the peak time and peak width of membrane total Akt.

In summary, based on the model families comparison in Figure 5.9 (in addition to time-series matching in Figure 5.7 earlier), we ranked the PIP3-dependent recruitment hypothesis highest. While the other two hypotheses were hard to discriminate from Figure 5.9 visually, we relied the peak time matching score to rank the PIP3-independent recruitment hypothesis second, and the retention hypothesis third.

5.7 Robustness analysis of PIP3-dependent recruitment model

Model calibration may produce models that are hyper-sensitive to certain parameters. We have observed earlier (Figure 5.8) that the PIP3-dependent recruitment model might have high variation around the nominal parameters (best estimates from model calibration), and we proceeded to identify the core set of parameters that most strongly impact the peak vector values. We thus performed the robustness analysis on all three hypotheses that were not disqualified, and this section will take the PIP3-dependent recruitment as an example. Robustness analysis results of other two hypotheses are available at the project webpage (<http://webbippe.nus.edu.sg:8080/Akt>).

In our robustness analysis (or local parameter sensitivity analysis), we systematically multiplied each parameter by $10x$, where x took 21 evenly distributed values from -1 to 1. The 12 peak vector dimensions were plotted for model with modification in each reaction rate parameter (Figure 5.10A) or “recruitment factor” spline knot parameters (Figure 5.10B).

Overall, each subplot in Figure 5.10 contains mostly flat lines, suggesting that the peak vector of the recruitment model is insensitive to most parameters, although there are certain exceptions. The peak times of Akt³⁰⁸, membrane Akt³⁰⁸ and membrane total Akt

is highly sensitive to the value of recruitment factor at 30 minutes (Figure 5.10A, dashed lines) and 120 minutes (Figure 5.10A, dotted lines with marker). This is expected as with low values of recruitment factor at 30 minutes, the 30-minute peak in nominal recruitment model could diminish leading to an earlier peak; or with high values of recruitment factor at 120 minutes, a new higher peak could be generated abruptly at a later timepoint than 30 minutes. While the peak amplitude is robust to reaction rate parameters (Figure 5.10B), the peak time and peak width can be sensitive (*i.e.* increased outcome amount is more than the changed amount in parameters) to some reaction rate parameters. These cases often correspond to the situations where the peak was abolished due to the reaction rate values, resulting in an excessively wide and/or late peak. In summary, it can be concluded that the recruitment model is partially robust, *i.e.* robust with respect to many but not all parameters.

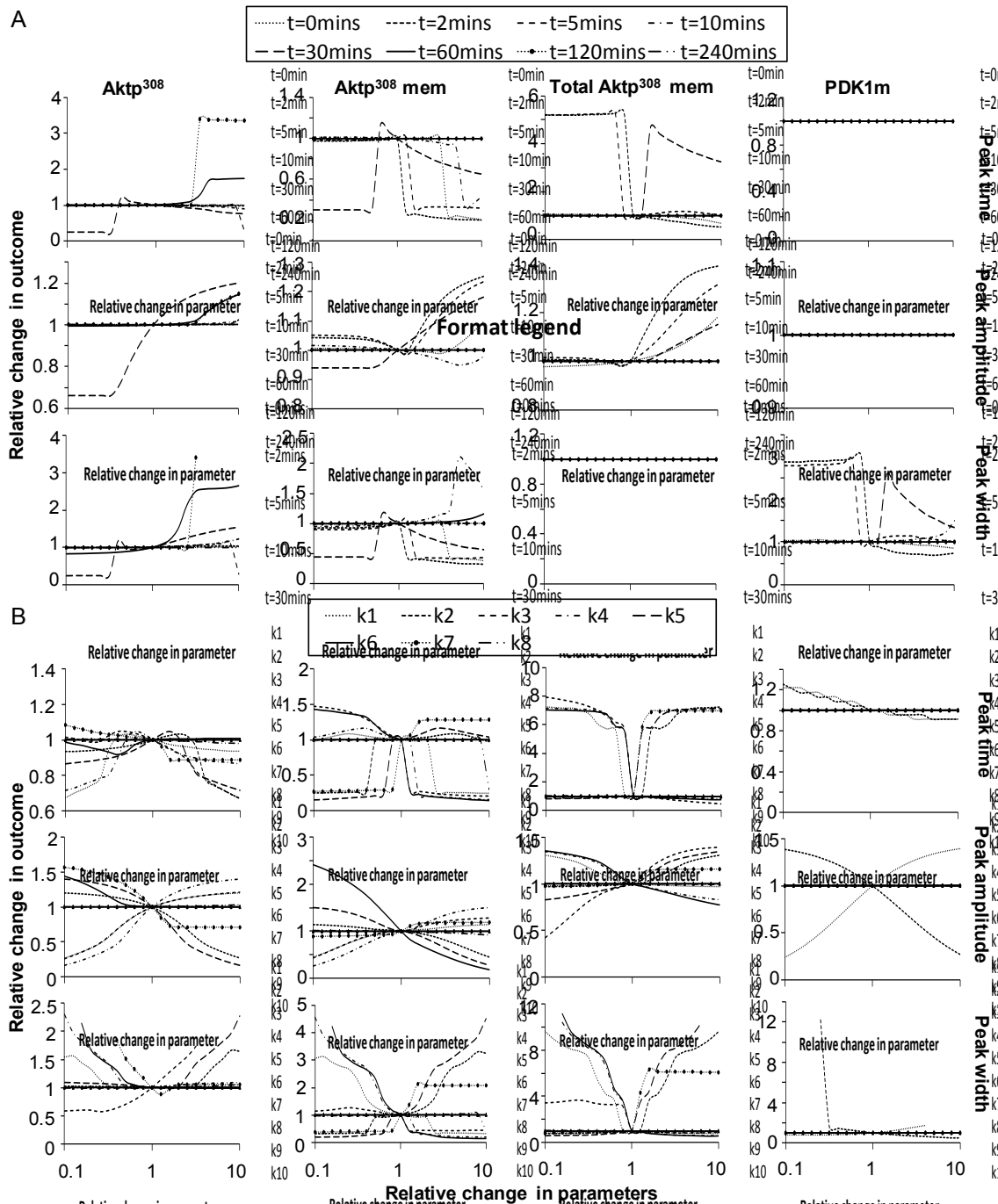


Figure 5.10 – Model robustness analysis. Robustness analysis of Aktp³⁰⁸ peak time, Aktp³⁰⁸ peak amplitude and Aktp³⁰⁸ peak width with respect to (A) reaction rate parameters and (B) recruitment factor spline knot parameters in PIP3-dependent recruitment model. The model was simulated with each parameter varied 1 order of magnitude above and below nominal values. Here k1-k8 correspond to the reaction rates as indicated in Table 1. Peak properties are described in Figure 5.9.

5.8 Discussion

Scope of study: PIP3-Aktp³⁰⁸

In Chapter Four, we identified a puzzling phenomenon in the Akt activation pathway under serum stimulation, leading to the search for “non-canonical activation of

Akt in serum-stimulated fibroblasts” as described in this chapter. Starting from the earlier Akt model for testing the SPEDRE method (Chapter Four), we narrowed down the scope to between PIP3 and Aktp³⁰⁸, due to the discovery of the large delay between the peak times of the measured time-series of these two species (Figure 5.1).

Within this PIP3-Aktp³⁰⁸ scope, we constructed the H0 model representing the canonical Akt activation pathway, at the individual-biochemical-process level of details. There have been numerous models that contain Akt activation pathway, but models such as by Leander *et al.* (Leander, et al., 2012) collapse the signaling cascade between PIP3 and Akt, making the activity of Akt closely tied to that of PI3Kinase. In our H0 model, by examining the pathway at a more fine-grained level of details, we discovered that interesting phenomena affecting the activation dynamics of Aktp³⁰⁸ may occur between PIP3 and Aktp³⁰⁸. More specifically, H0 was unable to explain the delay between the peaks of PIP3 and Aktp³⁰⁸, suggesting that some non-canonical effect causes the overshoot dynamics of Aktp³⁰⁸.

The failure of H0 to explain the large time-delay led to the search for an alternative hypothesis to reconcile the mismatch. We performed a modeling-driven hypothesis management approach in which the back-and-forth interaction between modeling and experiments is the centerpiece. As a result, we obtained novel biological insights about the prolonged membrane localization of Akt upon serum induction, and we reduce the initial number of hypotheses from 6 down to 3 remaining candidates, all capable of explaining the current data.

With the success demonstrated above, we found that the hypothesis management approach with reverse fitting pipeline was effective enough to allow many mechanisms to be discarded. However, manual effort was required for many steps in the process, and

this requirement is not yet a limiting factor in our PIP3-Aktp³⁰⁸ scope. To expand this method to large pathways, future developments are need to provide greater automation.

Timeline of hypothesis exclusions

Based on simulations for the canonical pathway (H0) model, this null hypothesis was insufficient to explain the dynamics of Aktp³⁰⁸ in total cell lysate. An external time-dependent factor was systematically introduced to different steps of the activation pathway, producing five alternative hypotheses. We assessed and ranked these five models based on agreement between simulated and measured time courses. The dephosphorylation and phosphorylation model families were rejected by the membrane fraction time-series experiments, because they couldn't explain why Akt would remain localized at the membrane after PIP3 levels decline. This analysis left three hypotheses potentially capable of explaining current data: PIP3-dependent augmented recruitment, prolonged membrane retention, and PIP3-independent augmented recruitment. Finally, the PIP3-dependent recruitment model was ranked highest based on the “peak vector” analysis from an ensemble of models from each hypothesis family, but the retention model and PIP3-independent recruitment model were not ruled out. Table 5.3 summarizes which models were considered viable (Pass) or unviable (Fail) after each stage.

		Test		
		Aktp ³⁰⁸ time-series	Membrane time-series	Ensemble analysis
Model	H0	Fail		
	Dephosphorylation	Pass	Fail	
	Phosphorylation	Pass	Fail	
	PIP3-independent recruitment	Pass	Pass	Ranked second
	Retention	Pass	Pass	Ranked third
	PIP3-dependent recruitment	Pass	Pass	Ranked first

Table 5.3 – Summary of model evaluation for null hypothesis and four alternative hypotheses, based on three tests performed in this study.

Biology contributions

Several aspects of this study may be of potential interest to Akt scientists. First is the novel mismatch between the peak times of PIP3 and Aktp³⁰⁸ (Figure 5.2), which has

not been reported in the literature. This mismatch of kinetics was not previously known and the peak and decline was previously attributed to receptor internalization (Hatakeyama, et al., 2003). The duration and timing of Akt phosphorylation were of wide biological significance, ranging from neuron latency (Camarena, et al., 2010), cardiac function (Hu, et al., 2008), cytotoxic T cell fate (Macintyre, et al., 2011), angiogenesis (Liao, 2008; Reed, et al., 2009), and proliferation in many cell types (Longo, et al., 2007; Longo, et al., 2008). The three remaining plausible hypotheses, out of five initial candidates, imply there is a membrane-localized mechanism that augments Akt levels at the membrane. This prolonged presence of Akt at the membrane (whether via recruitment or retention) is important because Akt impacts many downstream targets and the timing of its activity can regulate the downstream effect.

The second biology contribution is the implied significance of non-canonical activators. Via a series of hypothesis exclusion steps, we narrowed the initial five alternative scenarios down to a few very similar hypotheses: recruitment (PIP3-dependent or PIP3-independent) or retention of Akt at the membrane. Based on literature evidence, we can list some known non-canonical effects that fit these criteria: (1) Akt can bind PI34P in addition to PIP3 (Burelout, et al., 2007), and so PI34P might be responsible for the prolonged localization of Akt at the membrane after PIP3 levels decline. (2) Pak1 has been reported to serve as an anchor for localizing Akt at the plasma membrane (Higuchi, et al., 2008). (3) NHE1 is an integral membrane protein has been reported to promote Akt signaling through an indirect scaffolding effect (Wu, et al., 2004). (4) Membrane microdomains and caveolae are also known to regulate Akt localization (Gao, et al., 2011). These candidates do not represent an exhaustive list of non-canonical Akt activators, but carries substantial biological importance worthy of further investigation as future work.

Modeling-driven methods contribution

After finding the canonical model to be inadequate, we investigated the PIP3/Akt cascade following a top-down and holistic approach typical for a systems biology study, but without requiring extensive omic-scale data. We assumed there was a single non-canonical effect acting on the canonical pathway, and we systematically enumerated the steps of the canonical pathway at which a hypothetical perturbation may occur. This perturbation at each step was encoded using a pseudo-reaction (mathematically a linear spline), and we allowed the perturbation to take an arbitrary dynamic (spline shape). Then this spline can be optimized to allow the model to best match the data. In a simplistic view, we are making the following assumption: the observed Akt curve(s) should be equal to the network-propagated effects of PIP3, plus the network-propagated effects of the non-canonical perturbation. This allows us to perform the reverse fitting process (Figure 5.4), by back-computing the unknown perturbation curve shape from the known PIP3 and Akt³⁰⁸ dynamics. In our implementation, we represented the perturbation curve using a linear spline with unknown spline knots, and we reverse-fit the solution by optimizing the values of the spline knots, to maximize agreement with the observations.

The introduction of splines to represent the combined effect of the multiple unknown effects on the reactions is unconventional, and proves to be useful in distinguishing among hypotheses in this study. Effectively, we obtained a complete model of the perturbed system, facilitating various *in silico* experiments. This enables us to carry out experimental validation to distinguish among different hypothesis families, to prioritize the experiments which may lead to novel biological discovery. Biological experiments are often expensive compared to *in silico* experiments, and performing a smaller number of more efficient experiments may provide enough savings to pay for the cost of computational modeling. Although anecdotal, the illustrations from model

simulation were concrete, evocative, and valuable for the human process of deciding how to spend money. For example, by simulating the different alternative scenarios, modeling helps illustrate the time windows when the novel effects would be most easily observable. This allows more efficient extraction of information from a minimum expense of experiments to perform.

Importance of studying Akt membrane localization

For future studies of how Akt achieves prolonged localization at the membrane after PIP3 levels fall, there is a technology available for controlling Akt localization, independent of PIP3. Akt-Myr, a chimeric protein which was composed of a myristoylated constitutively active form of Akt and the ligand-binding domain of a mutant estrogen receptor (Kohn, *et al.*, 1998), can control Akt signaling activation in both timing and duration. Myr-Akt is inactivated in the absence of 4-hydroxytamoxifen (4OHT), but is activated rapidly by the addition of 4OHT (Murayama, *et al.*, 2007). This constitutively membrane-bound active form of Akt provides a wide range of applications in studying the effect of membrane Akt.

The endogenously membrane-localized active Akt could also have important implications for other downstream effectors in the signaling pathways. In chemotaxing cells, Akt is found to transiently translocate to the plasma membrane in response to receptor stimulation, which may indicate some important function in chemotaxis (Meili, *et al.*, 1999). The isoform Akt2 is found to accumulate at the plasma membrane of insulin-stimulated adipocytes, and this accumulation correlates with Akt2-specific regulation of the trafficking of the GLUT4 glucose transporter (Gonzalez and McGraw, 2009). Although distinguishing between the recruitment hypothesis and retention hypothesis may seem like splitting hairs, they have different implications for the localization of active Akt. This selection of examples points to an enormous potential for

biological effects to be regulated by the localization of active Akt at the membrane versus cytosol.

Importance of studying the timings of Akt activity

As described in the previous section, the localization of Akt is important in various cellular functions. More subtly, the dynamics of the localized concentration of Akt and its phosphorylation have been found to have an important role biological in various cell types and contexts. Akt is one of the most consistently over-activated pathways in cancer (Stephens, et al., 2012) and mechanisms allowing normal cells to achieve a transient peak of extreme Akt activation could be mutated to provide a permanent state of extreme Akt activation in cancer.

The biological importance of Akt duration is strongly supported by recent literature evidence. “Hub” proteins (i.e., factors with many downstream targets and effectors) often achieve differential functions through the dynamics of activation, and not exclusively through the magnitude of activation (Ebisuya, et al., 2005; Longo, et al., 2008). A very recent report shows that the dynamics of p53 plays a crucial role in determining cell fate (Purvis, *et al.*, 2012), which underscores the importance of studying Akt activation dynamics given the amount of crosstalk occurring between the two pathways (Gottlieb, *et al.*, 2002; Wee and Aguda, 2006). The amplitude and duration of Akt are critical factors in determining cell cycle progression in various cell types (Longo, *et al.*, 2007; Longo, *et al.*, 2008). Sustained activation of ERK, a downstream effector of Akt activation, is required for proliferation of fibroblasts, whereas transient activation does not induce cell-cycle entry (Murphy, *et al.*, 2002; Pouysségur and Lenormand, 2003). Sustained activation of Akt is also required for the proliferation and survival of activated murine T and B cells (Costello, *et al.*, 2002), and for driving cell-cycle progression of CLL B cells stimulated with CpG oligonucleotides (Longo, *et al.*, 2007).

Duration of Akt is also critical to maintain latency in neurons, as the ability of different growth factors to maintain latency is directly proportional to the duration of PI3-K signaling (Camarena, *et al.*, 2010). In SUR1-tg and Kir6.2 KO mice, both the extent and duration of Akt signaling are important in regulating cardiac function (Hu, *et al.*, 2008). Finally in cytotoxic T cells, the strength and duration of Akt activity dictates the transcriptional program and determines cell fate (Macintyre, *et al.*, 2011).

Caveats and future work

This study dealt with models where the parameter values were unknown, thus necessitating the parameter estimation process. As a high-dimensional non-linear optimizer is never guaranteed to find globally optimal values, there is a risk of accepting a significantly worse model than the optimal model. If a good-fit model (H₀, phosphorylation model, dephosphorylation model) indeed exists and we have failed to find it, the rejection of these models will not be valid. To overcome this shortcoming, we performed multiple complementary methods of parameter estimation and used a large number of random restarts before accepting a “best-fit” model to the data, judged solely by our parameter estimation strategy. Besides, we adopted a conservative strategy for ruling out models, only rejecting the cases with gross violations of the experimental measurements.

In our reverse fitting pipeline, we make necessary assumptions to keep the models simple and thus manageable. Each hypothetical effect (linear spline) increases the number of unknown parameters in the system, which worsens the problem of overfitting. With excessive degrees of freedom any hypothesis can fit the data and none could be rejected. The alternative hypotheses were thus carefully designed to limit the additional degrees of freedom introduced to the H₀ model. At the other extreme, our model will be overly simplistic if we require the parameters to be identifiable from the data (Srinath and

Gunawan, 2010). Our modeling presents a case of under-determined models with 26 unknown parameters. We were able to proceed with under-determined models because overfitting does not interfere with correct rejection of a hypothesis, and we were still able to reject most of the hypotheses by interplay between modeling and experiments.

However, biological systems are frequently redundant, and more than one perturbation of the canonical pathway may actually occur. We assumed in Figure 5.3 that the unknown effect would occur at one of 5 possible steps in the canonical pathway of Akt activation, but this assumption could be incorrect if there are multiple simultaneous effects, if an effect straddles a boundary between hypotheses, or if there is an unknown effect that phosphorylates Akt without utilizing any other factors in the canonical pathway. We built a single “nominal” network formalization to represent each model family, based on literature evidence and our measurements. There are possible phenomena which do not fit the five formalized families of hypotheses (Figure 5.3B-F). For instance, this study assumes PIP3 was active, membrane-bound PDK1 was active, and phosphorylated Akt was active. However any of these species may be partially inactive, inactivated or sequestered by unknown effects, *e.g.* the plasma membrane or cytosol may have microenvironments that increase or decrease specific reactions of the pathway. Further, some environment factors such as pH (Bright, et al., 1989) are known to affect multiple reactions at once, making it possible that single non-canonical phenomena could affect more than one step of the model. Finally there could be violations of our simplifying assumptions. For instance, we interpreted the lack of PP2A in the membrane fraction (Luo, et al., 2012) to indicate that dephosphorylation is cytosolic in this cell type. For future work, it is desirable to increase the diversity in each model family where each individual model may not share the same network depiction. However it should also be noted that the number of possibilities is infinite and we can't

guarantee coverage of an infinite space. There should be a trade-off between the time resource and the potential of each network depiction to be biologically relevant. If a model is too complex, it will have too many free parameters, resulting in an overfitted model with diminished capacity to make new predictions.

Besides the risk of erroneously rejecting hypotheses based on poor-fit parameterization, there is also a risk of over-interpreting a good-fit model as describing how the alternative hypothesis would necessarily work. In the complex high-dimensional model space, there may be multiple minima equally capable of producing the good fit. For a hypothesis that fits data, we do not select a single minimum (such as the model parameterization we reached) and labeled other minima as inferior, but rather we simply conclude that there exists one parameter set that allows this hypothesis to fit the measurements. We also do not assign absolute score of fitness among alternative hypotheses, other than an acceptable/unacceptable decision for each hypothesis. In a near future, when more datapoints are available, we may adopt methods such as Bayesian scoring of multiple model parameterizations (Eydgahi, et al., 2013) to achieve better ranking for the alternative hypotheses by quality of fit. Note that this fitting would utilize the experimental error bars.

Experimental time-series measurements are subject to many sources of noise, which affect proper interpretation of biological meaning. For example, western blot experiments generally deviate farther from an ideal linear response when the protein has very low abundance or very high abundance. In time-series experiments, there is greater consistency in the timepoint-to-timepoint trends for each batch, than there is from batch to batch in replication. We instead plot the median (Figure 5.6) and also we also provide primary data from all replicates. We primarily assess the time-series qualitatively, by computing the curve-shape features (Figure 5.9). While these features are represented

using numbers, we call them qualitative because they have lower resolution than the original dataset, and the decision which alternative hypotheses to reject included human inspection (with no automated cut-off). For future work, we seek to improve the theoretical curve-shape features with maximal robustness to the underlying distribution of experimental noise.

The PIP3 inhibition experiment suggested by modeling in Figure 5.8 has several practical constraints, including the lack of specific PIP3-inhibitors. A follow-up experiment by Dr. Luo Le (Appendix A2) used LY294002 (inhibitor of PI3Kinase) together with 10%FBS treatment and measured the dynamics of membrane total using western blot. Comparing the measured time series (Appendix A2, right plot, dashed curve) to the simulated time course from each model (solid curves), the PIP3-independent recruitment model (red curve) displayed the least agreement with data. In other words, there may be a PI3K-dependent but PIP3-independent mechanism of Akt recruitment to the membrane, but further experiments ruled out the possibility of a PI3K-independent or LY290004-independent recruitment effect.

Conclusions

As demonstrated throughout this chapter, computational modeling is a powerful tool to study complex interactions between signal transduction species. While investigating each model, we observe non-obvious distinctions and similarities among the models that can be tested experimentally. The time-evolved simulations give insights to how the system changes with time, thus helping experimentalists focus more narrowly on certain time windows when novel effects are more likely to be observed. By utilizing model predictions, one can decrease the number of time-points to measure, or decrease the probability of missing an effect because of choosing the wrong timepoints. Meanwhile, modeling serves to visualize complex system-level effects in a signaling

network. As mathematic modeling has been previously shown to give insights that human intuition may fail to catch (Berro, *et al.*, 2010), modeling Akt activation dynamics can lead to more efficient experiments. The hypothesis management coupled with reverse-fitting approach in this study could be extended to similar biochemical pathway studies where data show non-trivial dynamics such as that of Aktp³⁰⁸ in MEF cells treated with 10% FBS. Even subtle or transient effects that increase Akt activation are important to elucidate because the existing pathways that can heighten Akt activation in normal cells may also be adopted by cancers to activate Akt further or longer.

In conclusion, efforts to improve or challenge the canonical signaling pathways are often met with great obstacles, both from the massive body of published literature and the unknowns (such as reaction rates) associated with each published discovery. Experiments to probe new frontiers for unknown pathway components often require enormous investment of time and resource. The relatively new computational systems biology paradigm can be a promising solution to the current bottlenecks. By performing the low-cost *in silico* experiments, computational modeling can predict more informative experiments and extract the stronger inferences from the analysis of existing data. With more advances to the hypothesis management in the future, it is hoped that every step of the scientific method can be integrated seamlessly: experiment designs, data acquisition using high-throughput assays, and hypothesis evaluation (more automated) work in conjunction to accelerate biological findings.

CHAPTER SIX: CONCLUSIONS AND FUTURE WORK

6.1 Summary of methodologies

This thesis research has been focused on two systems biology topics: (1) data-rich parameter estimation methodology and (2) modeling of Akt phosphorylation dynamics upon activation by growth factors. Parameter estimation is one of the main challenges in pathway modeling studies, and is currently still an active area of research. In the first topic, we developed the SPEDRE method to tackle this problem, but the method has special requirement of complete data for all species in the pathway. To perform benchmark comparison between SPEDRE and current state-of-the-art methods, we constructed a model of Akt activation, based on previously published data (Lim and Clément, 2007).

Further modeling of the Akt pathway led to the unexpected discovery of unresolved mismatch between the peak times of PIP3 and Aktp³⁰⁸ in the canonical Akt activation pathway, and in the second topic of the thesis, we developed a novel approach we call “hypothesis management” to reconcile this mismatch. Our approach includes the following novel approaches: constructing alternative hypotheses with linear spline representing the hypothetical effect over time, reverse fitting to determine the spline curve trend, treating time-dimensions as absolute and concentration-dimension as relative, and peak characteristics analysis of model families.

A common thread connecting the two research topics is the CHEGS approach, as introduced in Section 1.5. Below, we summarize how the elements of CHEGS were used in each research topic.

In the “data-rich parameter estimation” work (Chapter Three and Four), we employed *Computational methods* to estimate kinetic parameters in biochemical pathways, applied to cases with abundantly available data. The belief propagation

algorithm, which employs *Heuristics* extensively, played a critical role in finding the approximate MAP estimates. The ODE models and kinetic rate parameters were converted into a probability framework, and the best fits between simulated and estimated time courses were equivalent to the *MAP Estimates*. To achieve scalability to large problems, we chose coarse discretization instead introduce a post-processor was used in our method to refine the coarse-grained estimates to improve the *Generalizability* of method. The granularity of each rate parameters represented the trade-off between parameter accuracy and of computation time. Finally, using discretization, the parameter space was *Systematically* covered and evaluated using inferencing methods.

Similar to the “data-rich parameter estimation” work, the “modeling of Akt phosphorylation upon activation by growth factors” work (Chapters Four and Five) also utilized the CHEGS approach in many aspects. We constructed *Computational* models to apply to current state-of-the-art knowledge of the Akt activation pathway to prove the existence of unknown effects. *Heuristics* were used in this problem, since each model family was represented by one model formulated based on our best knowledge of the current literature and recent data. The merits of each model were evaluated based on goodness of fit, similar to a *MAP Estimate*, based on experimental data. To represent the hypothetical effect in each alternative model, we used a “spline curve” which introduced a set of free parameters as spline knots to the systems. By limiting the spline complexity, we sacrificed complex models in favor of more *Generalizable* models with lower degrees-of-freedom which might hold more predictive power. Finally, we *Systematically* introduced the modification to each reaction to produce hypothetical modifications of this canonical pathway that might reconcile the inconsistency between the canonical pathway and recent experimental data.

6.2 Summary of Contributions

This thesis produced two sets of deliverables: first it introduces a novel hypothesis management approach to the study of an important pathway of cell survival, and second it produces efficient algorithms, packaged in a freely available software format with a graphical interface, that enables biologists to harness the power of the server from any desktop computer. In addition, each individual research project also presents some unique contributions judged by its own merits.

The data-rich parameter estimation work (Chapters Three and Four) introduced a novel method of estimation for reaction rate parameters in ODE models of biochemical pathways. The methodology novelty is the partial decomposition of the parameter estimation problem, the systematic evaluation of fitness of the ODEs using coarse discretization, and the use of inferencing techniques in a probabilistic network to compute the maximum *a posteriori* estimates efficiently but approximately. Theoretical asymptotic analysis, which is not possible in most parameter estimation methods, points out the characteristics of the problems that yield high efficiency for SPEDRE methods. In the context of data-rich parameter estimation, this work is among the few methods to provide a general-purpose application with a web server graphical interface. The method was evaluated empirically in comparison with 14 state-of-the-art parameter estimation methods, and showed superior performance in the low-degree Akt model with low-noise data.

The “modeling of Akt phosphorylation upon activation by growth factors” work (Chapter Four and Five) contributed to the scientific community in three aspects. In the first aspect, we introduced novel methodologies. First, we identified 5 steps in the canonical pathway (one step was rejected, leaving 4). Next, representing the trend of each hypothetical effect over time by linear splines, we built candidate models for modifying

each step in the canonical pathway. The spline knots were optimized together with other model parameters (reaction rates, initial concentrations), and the spline shape was obtained by parameter estimation (in other words, we explored with automation the hypothesis space with different spline shapes). Finally, the analysis and prediction from modeling led to the execution of two biological experiments that yielded novel insights into the Akt activation pathway.

In the second aspect, the hypothesis management process achieved sufficient specificity to discriminate among the alternative hypothesis based on the biological measurements, which successfully narrowed five hypotheses (plus one null hypothesis) down to three remaining candidates. This serves as a “pruning” process from the extensive search space, which helps limit the number of possibilities for further experiments to pursue.

In the final aspect, this project introduces a potentially useful way to look at biological time-series data: qualitative analyses based on absolute-time and relative-concentration. This method accounts for the nature of western blots experiments where the most reliable information is the timings of events. To study multiple model ensembles comparatively, we also abstract the trajectories into sets of “peak characteristics”. An analysis of “peak characteristics” from a model ensemble from each model structure allows a different way to discriminate between alternative hypotheses.

6.3 Future work

For the “data-rich parameter estimation” work, it is essential to continue to characterize the types of problems that can be applied efficiently to the SPEDRE methods. The coming age of complete measurements for all species (Mann, et al., 2013), will provide many data-rich problems for SPEDRE to be applied to. Besides, the current

stringent requirements of sparse network must be relaxed (such as by incorporating pathway decomposition techniques) to allow a wider range of applications.

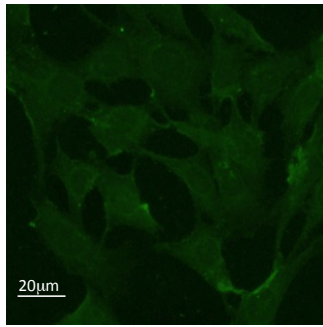
For the “modeling of Akt phosphorylation upon activation by growth factors” work, modeling has to continue to evolve to incorporate new findings, especially those that involve augmented membrane recruitment or prolonged membrane retention of Akt. Model parameters can be further refined from more powerful model calibration technologies, including high-throughput proteomics time-series data and advance parameter estimation methods.

While the thesis has addressed several gaps in the current scientific knowledge of systems biology, it also presents new challenges for future development. It is hoped that the research approaches that have been to some success in this thesis could be found useful and therefore adopted in other related venues in computational systems biology.

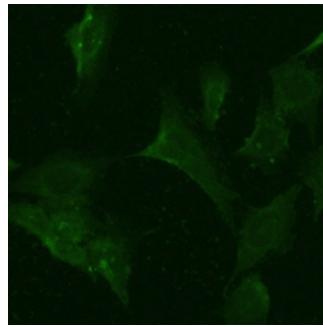
APPENDICES

This Appendices section describes the additional figures and data that were generated in the course of this thesis study. Figure A1 described two replicates of the PIP3 immunofluorescence experiments (in main text Figure 5.1), under the treatment of 10% FBS stimulation at time $t=0$. The cell culture was prepared by Dr. Luo Le, and subsequent immunofluorescence and confocal imaging experiments were performed by the author under supervision, following the protocols described in Chapter Three. These replicates (Figure A1) confirmed the early peak time of PIP3 (at 2min or 5min), incompatible with the 30min peak time of Aktp³⁰⁸ under the null hypothesis. Figure A2 describes the time-series membrane fractionation measurements of total Akt in MEFs treated with LY290004 at 2 hours before $t=0$, and then treated with 10%FBS at $t=0$ (performed by Dr. Luo Le). The “flat” dynamic of membrane total Akt (dashed line) suggests that a non-canonical Akt recruitment effect, if exists, is also inhibited under the treatment of LY290004.

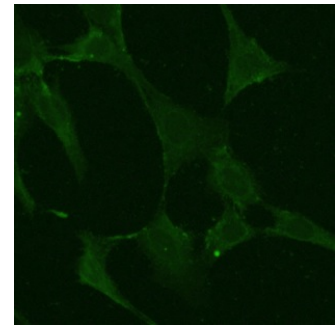
A



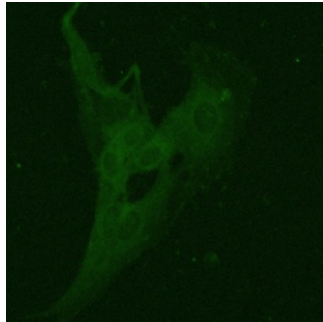
t=0



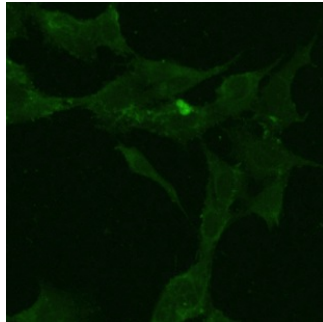
t=2



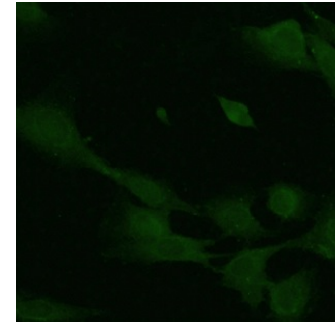
t=5



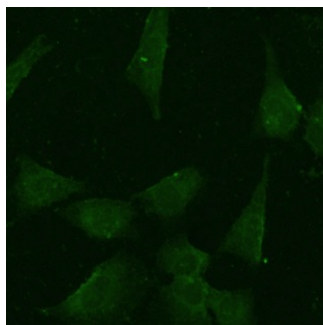
t=10



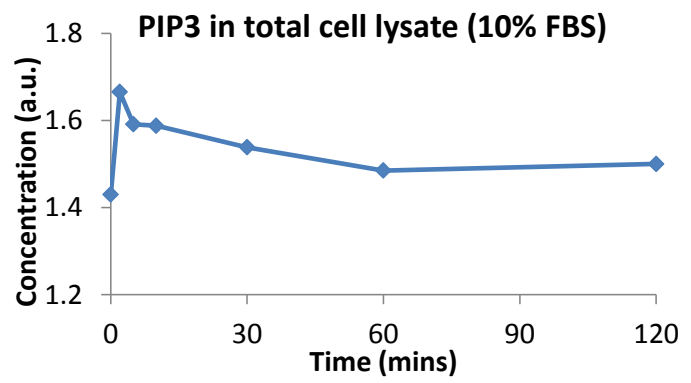
t=30



t=60



t=120



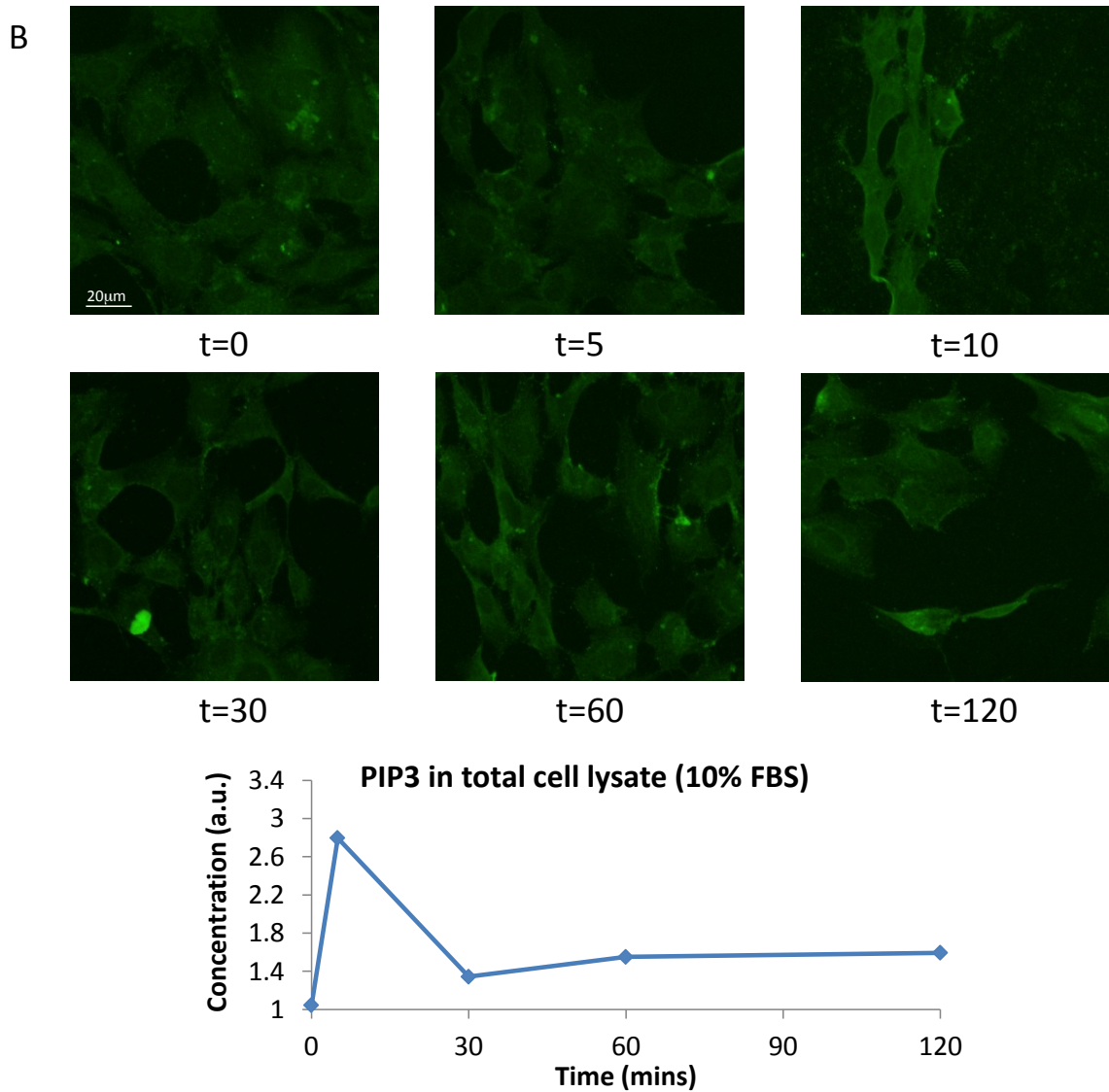


Figure A1 – Two replicates (A) and (B) of PIP3 immunofluorescence confocal imaging time series measurement in serum-stimulated wild type mouse embryonic fibroblasts (MEF). Experiments were performed by the author as “supervised experiments”. Cells were normally grown in culture containing 10% fetal bovine serum (FBS). At 24 hours before t=0, cells were starved in culture containing 0.5% FBS. At time t=0, cells were treated with 10%FBS and measurement was performed at different timepoints after t=0. Bottom right plot: quantified time-series (arbitrary scaling) of PIP3.

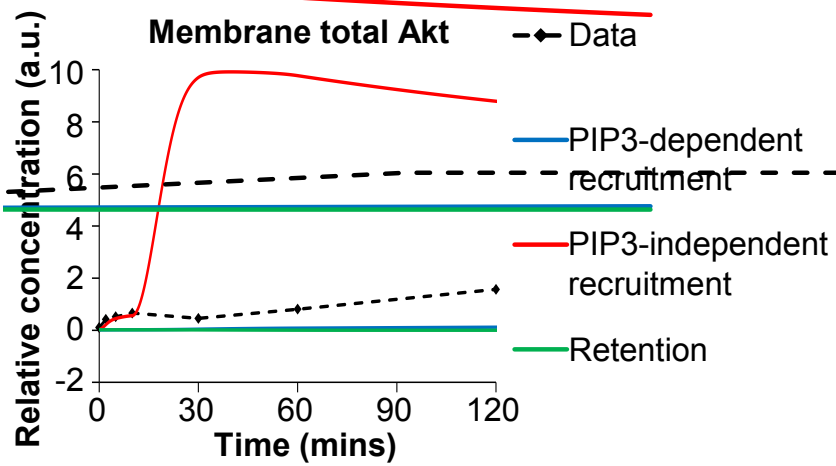


Figure A2 – Quantified time-series data of membrane total Akt fractions under LY290004 treatment compared with the simulated time course from three alternative models.

Data were obtained from western blot experiments performed by Dr. Luo Le (NUS Department of Biochemistry). Dashed line: observed time-series for membrane total Akt (n=3 replicates). Solid line: simulated time course of membrane total Akt from each model.

PAPERS AND PRESENTATIONS

Papers

Nim, T.H., Luo, L., Clément, M.-V., White, J.K., Tucker-Kellogg, L., “Systematic Parameter Estimation in Data-Rich Environments (SPEDRE) for Cell Signaling Dynamics”, 2012. *Bioinformatics*. Accepted.

Nim, T.H., Luo, L., Clément, M.-V., White, J.K., Tucker-Kellogg, L., “Computational Modeling of Serum-induced Activation of Akt Threonine-308 Phosphorylation”, 2012. To be submitted to *PLoS Computational Biology*.

Nim, T.H., Clément, M.-V., White, J.K., Tucker-Kellogg, L. “Parameter Estimation Web Service Tailored for Data-Rich Biochemical Pathways”, 2012. Submitted to *Nucleic Acids Research*, web server issue.

Nim, T.H., Luo, L., Clément, M.-V., White, J.K., Tucker-Kellogg, L., “Estimating Reaction Rate Parameters in Cell Signaling Pathways Using Extreme Decomposition and Belief Propagation Tailored for Data-Rich Cases”, *arXiv:1103.0907v1* 2011.

Conference oral presentations

Nim, T.H., Luo, L., Clément, M.-V., White, J.K., Tucker-Kellogg, L., “Mathematical modeling of Akt phosphorylation in mouse embryonic fibroblast upon serum induction”, Singapore-MIT Alliance Symposium, 2012, National University of Singapore. Won an award for best presentation.

Nim, T.H., Clément, M.-V., White, J.K., Tucker-Kellogg, L. “Parameter Estimation Web Service Tailored for Data-Rich Biochemical Pathways”, in *The International Conference on Bioinformatics (InCoB)*, 2011, Kuala Lumpur, Malaysia. Poster selected for oral presentation.

Nim, T.H., Tucker-Kellogg, L., White, J.K. “Fast and Deterministic Parameter Estimation of Biological Pathway using Belief Propagation”, in *Systems Biology: Integrative Comparative & Multi-Scale Modeling*, 2009, Iowa, USA.

Conference poster presentations

Nim, T.H., Luo, L., Clément, M.-V., White, J.K., Tucker-Kellogg, L., “Mathematical modeling of Akt phosphorylation dynamics in serum-stimulated fibroblasts”, in *Integrative Network Biology: Network Medicine*, 2012, Helsingor, Denmark. Won a travel fellowship award.

Nim, T.H., Margadant, F., Tucker-Kellogg, L. "Simulated Observability of Molecular Lengths in Single Molecule Localization Microscopy", in *Focus on Microscopy (FOM2012)*, 2012, Singapore. Presented a poster and a demo session.

REFERENCES

- AAAS and Stanford (2012) Database of Cell Signaling.
- Acharya, A., *et al.* (2010) Redox regulation in cancer: a double-edged sword with therapeutic potential, *Oxidative medicine and cellular longevity*, **3**, 23-34.
- Aderem, A. (2005) Systems biology: its practice and challenges, *Cell*, **121**, 511-513.
- Albeck, J.G., *et al.* (2008) Quantitative analysis of pathways controlling extrinsic apoptosis in single cells, *Mol Cell*, **30**, 11-25.
- Alberts, B., *et al.* (2007) *Molecular Biology of the Cell*. Garland Science.
- Aldridge, B.B., *et al.* (2006) Physicochemical modelling of cell signalling pathways, *Nature cell biology*, **8**, 1195-1203.
- Alessi, D.R., *et al.* (1996) Mechanism of activation of protein kinase B by insulin and IGF-1, *The EMBO journal*, **15**, 6541-6551.
- Ananthanarayanan, B., *et al.* (2007) Live-cell molecular analysis of Akt activation reveals roles for activation loop phosphorylation, *The Journal of biological chemistry*, **282**, 36634-36641.
- Apgar, J.F., *et al.* (2008) Stimulus design for model selection and validation in cell signaling, *PLoS computational biology*, **4**.
- Ashyraliyev, M., *et al.* (2009) Systems biology: parameter estimation for biochemical models, *The FEBS journal*, **276**, 886-902.
- Basak, S., *et al.* (2007) A fourth IkappaB protein within the NF-kappaB signaling module, *Cell*, **128**, 369-381.
- Bentele, M., *et al.* (2004) Mathematical modeling reveals threshold mechanism in CD95-induced apoptosis, *J Cell Biol*, **166**, 839-851.
- Berro, J., Sirotkin, V. and Pollard, T.D. (2010) Mathematical modeling of endocytic actin patch kinetics in fission yeast: disassembly requires release of actin filament fragments, *Molecular biology of the cell*, **21**, 2905-2915.
- Biondi, R.M., *et al.* (2000) Identification of a pocket in the PDK1 kinase domain that interacts with PIF and the C-terminal residues of PKA, *The EMBO journal*, **19**, 979-988.
- Birtwistle, M.R., *et al.* (2007) Ligand-dependent responses of the ErbB signaling network: experimental and modeling analyses, *Mol Syst Biol*, **3**, 144.
- Brewer, D., *et al.* (2008) Fitting ordinary differential equations to short time course data, *Philosophical Transactions of the Royal Society A: Mathematical, Physical and Engineering Sciences*, **366**, 519-544.
- Bright, G.R., *et al.* (1989) Heterogeneity of the changes in cytoplasmic pH upon serum stimulation of quiescent fibroblasts, *Journal of cellular physiology*, **141**, 410-419.
- Brognard, J. and Newton, A.C. (2008) PHLiPPing the switch on Akt and protein kinase C signaling, *Trends in endocrinology and metabolism: TEM*, **19**, 223-230.

- Brognard, J., *et al.* (2009) Common polymorphism in the phosphatase PHLPP2 results in reduced regulation of Akt and protein kinase C, *The Journal of biological chemistry*, **284**, 15215-15223.
- Burelout, C., Naccache, P.H. and Bourgoin, S.G. (2007) Dissociation between the translocation and the activation of Akt in fMLP-stimulated human neutrophils--effect of prostaglandin E2, *Journal of leukocyte biology*, **81**, 1523-1534.
- Cairns, R.A., Harris, I.S. and Mak, T.W. (2011) Regulation of cancer cell metabolism, *Nature reviews Cancer.*, **11**, 85-95.
- Camarena, V., *et al.* (2010) Nature and duration of growth factor signaling through receptor tyrosine kinases regulates HSV-1 latency in neurons, *Cell host & microbe*, **8**, 320-330.
- Cannito, S., *et al.* (2010) Epithelial-mesenchymal transition: from molecular mechanisms, redox regulation to implications in human health and disease, *Antioxidants & redox signaling*, **12**, 1383-1430.
- Carnero, A. (2010) The PKB/AKT pathway in cancer, *Current pharmaceutical design*, **16**, 34-44.
- Carnero, A., *et al.* (2008) The PTEN/PI3K/AKT Signalling Pathway in Cancer, Therapeutic Implications, *Current Cancer Drug Targets*, **8**, 187-198.
- Chen, W.W., *et al.* (2009) Input-output behavior of ErbB signaling pathways as revealed by a mass action model trained against dynamic data, *Mol Syst Biol*, **5**, 239.
- Cho, H., *et al.* (2001) Insulin resistance and a diabetes mellitus-like syndrome in mice lacking the protein kinase Akt2 (PKB beta), *Science (New York, NY.)*, **292**, 1728-1731.
- Chou, I.C., Martens, H. and Voit, E.O. (2006) Parameter estimation in biochemical systems models with alternating regression, *Theor Biol Med Model.*, **3**, 25.
- Chou, I.C. and Voit, E.O. (2009) Recent developments in parameter estimation and structure identification of biochemical and genomic systems, *Math Biosci*, **219**, 57-83.
- Chu, Y. and Hahn, J. (2008) Integrating parameter selection with experimental design under uncertainty for nonlinear dynamic systems, *AIChE Journal*, **54**, 2310-2320.
- Cicenas, J., *et al.* (2005) Increased level of phosphorylated akt measured by chemiluminescence-linked immunosorbent assay is a predictor of poor prognosis in primary breast cancer overexpressing ErbB-2, *Breast cancer research : BCR*, **7**, R394-401.
- Clément, M.V. and Pervaiz, S. (2001) Intracellular superoxide and hydrogen peroxide concentrations: a critical balance that determines survival or death, *Redox report : communications in free radical research*, **6**, 211-214.
- Costello, P.S., Gallagher, M. and Cantrell, D.A. (2002) Sustained and dynamic inositol lipid metabolism inside and outside the immunological synapse, *Nature immunology*, **3**, 1082-1089.
- Dada, J. and Mendes, P. (2009) Design and Architecture of Web Services for Simulation of Biochemical Systems. In Paton, N., Missier, P. and Hedeler, C. (eds), *Lecture Notes in Computer Science*. Springer Berlin / Heidelberg, pp. 182-195.
- de Jong, H. (2002) Modeling and simulation of genetic regulatory systems: a literature review, *Journal of computational biology : a journal of computational molecular cell biology*, **9**, 67-103.
- Degroot, M.H. (1970) *Optimal Statistical Decisions*. McGraw-Hill Book Company.

- Descamps, G., *et al.* (2004) The magnitude of Akt/phosphatidylinositol 3'-kinase proliferating signaling is related to CD45 expression in human myeloma cells, *Journal of immunology (Baltimore, Md: 1950)*, **173**, 4953-4959.
- Donahue, A.C. and Fruman, D.A. (2003) Proliferation and survival of activated B cells requires sustained antigen receptor engagement and phosphoinositide 3-kinase activation, *Journal of immunology (Baltimore, Md: 1950)*, **170**, 5851-5860.
- Ebisuya, M., Kondoh, K. and Nishida, E. (2005) The duration, magnitude and compartmentalization of ERK MAP kinase activity: mechanisms for providing signaling specificity, *Journal of cell science*, **118**, 2997-3002.
- Eungdamrong, N.J. and Iyengar, R. (2004) Modeling cell signaling networks, *Biology of the cell / under the auspices of the European Cell Biology Organization*, **96**, 355-362.
- Eydgahi, H., *et al.* (2013) Properties of cell death models calibrated and compared using Bayesian approaches, *Molecular systems biology*, **9**, 644.
- Fall, C., *et al.* (2002) *Computational cell biology*. Springer.
- Farkas, I.J., *et al.* (2011) Network-based tools for the identification of novel drug targets, *Science signaling*, **4**.
- Flohé, L. (2010) Changing paradigms in thiology from antioxidant defense toward redox regulation, *Methods in enzymology*, **473**, 1-39.
- Fogel, D.B., Fogel, L.J. and Atmar, J.W. (1991) Meta-Evolutionary Programming, *Conference Record of the Twenty-Fifth Asilomar Conference on Signals, Systems & Computers, Vols 1 and 2*, 540-545, 1274.
- Foley, T.D., *et al.* (2007) Oxidative inhibition of protein phosphatase 2A activity: role of catalytic subunit disulfides, *Neurochemical research*, **32**, 1957-1964.
- Fomekong-Nanfack, Y., Kaandorp, J.A. and Blom, J. (2007) Efficient parameter estimation for spatio-temporal models of pattern formation: case study of *Drosophila melanogaster*, *Bioinformatics*, **23**, 3356-3363.
- Friedberg, E.C. (2008) Sydney Brenner, *Nat Rev Mol Cell Biol*, **9**, 8-9.
- Funahashi, A., *et al.* (2003) CellDesigner: a process diagram editor for gene-regulatory and biochemical networks, *Drug Discovery Today: BIOSILICO*, **1**, 159-162.
- Gao, X., *et al.* (2011) PI3K/Akt signaling requires spatial compartmentalization in plasma membrane microdomains, *Proceedings of the National Academy of Sciences of the United States of America*, **108**, 14509-14514.
- Gewinner, C., *et al.* (2009) Evidence that Inositol Polyphosphate 4-Phosphatase Type II Is a Tumor Suppressor that Inhibits PI3K Signaling.
- Gonzalez, E. and McGraw, T.E. (2009) Insulin-modulated Akt subcellular localization determines Akt isoform-specific signaling, *Proceedings of the National Academy of Sciences of the United States of America*, **106**, 7004-7009.
- Gottlieb, T.M., *et al.* (2002) Cross-talk between Akt, p53 and Mdm2: possible implications for the regulation of apoptosis, *Oncogene*, **21**, 1299-1303.

- Gough, N.R. and Yaffe, M.B. (2011) Focus issue: conquering the data mountain, *Science signaling*, **4**.
- Habib, T., *et al.* (1998) Growth factors and insulin stimulate tyrosine phosphorylation of the 51C/SHIP2 protein, *The Journal of biological chemistry*, **273**, 18605-18609.
- Hanada, M., Feng, J. and Hemmings, B.A. (2004) Structure, regulation and function of PKB/AKT--a major therapeutic target, *Biochimica et biophysica acta*, **1697**, 3-16.
- Hancock, J.T. (2005) *Cell Signalling*. Oxford University Press, USA.
- Hatakeyama, M., *et al.* (2003) A computational model on the modulation of mitogen-activated protein kinase (MAPK) and Akt pathways in heregulin-induced ErbB signalling, *The Biochemical journal*, **373**, 451-463.
- Heit, B., *et al.* (2002) An intracellular signaling hierarchy determines direction of migration in opposing chemotactic gradients, *The Journal of cell biology*, **159**, 91-102.
- Higuchi, M., *et al.* (2008) Scaffolding function of PAK in the PDK1-Akt pathway, *Nature cell biology*, **10**, 1356-1364.
- Hoffmann, A., *et al.* (2002) The IkappaB-NF-kappaB signaling module: temporal control and selective gene activation, *Science*, **298**, 1241-1245.
- Hoops, S., *et al.* (2006) COPASI--a COMplex PATHway Simulator, *Bioinformatics*, **22**, 3067-3074.
- Hu, X., *et al.* (2008) Disruption of sarcolemmal ATP-sensitive potassium channel activity impairs the cardiac response to systolic overload, *Circulation research*, **103**, 1009-1017.
- Hua, F., *et al.* (2005) Effects of Bcl-2 levels on Fas signaling-induced caspase-3 activation: molecular genetic tests of computational model predictions, *Journal of immunology (Baltimore, Md. : 1950)*, **175**, 985-995.
- Huang, C.Y. and Ferrell, J.E. (1996) Ultrasensitivity in the mitogen-activated protein kinase cascade, *Proceedings of the National Academy of Sciences of the United States of America*, **93**, 10078-10083.
- Huang, C.Y. and Ferrell, J.E. (1996) Ultrasensitivity in the mitogen-activated protein kinase cascade, *Proceedings of the National Academy of Sciences*, **93**, 10078-10083.
- Hucka, M., *et al.* (2002) Systems Biology Workbench Java TM programmer's manual.
- Hughey, J.J., Lee, T.K. and Covert, M.W. (2010) Computational modeling of mammalian signaling networks, *Wiley interdisciplinary reviews: Systems biology and medicine*, **2**, 194-209.
- Janes, K.A. and Yaffe, M.B. (2006) Data-driven modelling of signal-transduction networks, *Nature reviews: Molecular cell biology*, **7**, 820-828.
- Kanehisa, M., *et al.* (2012) KEGG for integration and interpretation of large-scale molecular data sets, *Nucleic acids research*, **40**, D109-114.
- Katara, S., Aditya Bhan, James M. Caruthers, W. Nicholas Delgass and Venkat Venkatasubramanian (2004) A hybrid genetic algorithm for efficient parameter estimation of large kinetic models, *Computers & Chemical Engineering*, **28**, 2569-2581

Kennedy, J. and Eberhart, R. (1942) Particle Swarm Optimization. Perth, Australia, pp. 1942-1948.

Kennedy, J. and Eberhart, R. (1942) Particle Swarm Optimization. *Proceedings of the Fourth IEEE International Conference on Neural Networks*. Perth, Australia, pp. 1942 - 1948.

Kholodenko, B.N., Bruggeman, F.J. and Sauro, H.M. (2005) Mechanistic and modular approaches to modeling and inference of cellular regulatory networks. In, *Topics in Current Genetics*. pp. 357-451.

Kleinstein, S.H., *et al.* (2006) Nonuniform sampling for global optimization of kinetic rate constants in biological pathways, *Proceedings of the 2006 Winter Simulation Conference, Vols 1-5*, 1611-1616, 2307.

Klipp, E. and Krause, F. (2011) Computational Tools for Systems Biology, *Cancer Systems Biology, Bioinformatics and Medicine*, 213-243.

Koh, G., *et al.* (2006) A decompositional approach to parameter estimation in pathway modeling: a case study of the Akt and MAPK pathways and their crosstalk, *Bioinformatics (Oxford, England)*, **22**, e271-280.

Koh, G., *et al.* (2007) Composing Globally Consistent Pathway Parameter Estimates Through Belief Propagation *Algorithms in Bioinformatics, 7th International Workshop, WABI 2007*. Philadelphia, PA, USA.

Kohn, A.D., *et al.* (1998) Construction and characterization of a conditionally active version of the serine/threonine kinase Akt, *The Journal of biological chemistry*, **273**, 11937-11943.

Komorowski, M., *et al.* (2011) Sensitivity, robustness, and identifiability in stochastic chemical kinetics models, *Proceedings of the National Academy of Sciences of the United States of America*, **108**, 8645-8650.

Koseoglu, S., *et al.* (2007) AKT1, AKT2 and AKT3-dependent cell survival is cell line-specific and knockdown of all three isoforms selectively induces apoptosis in 20 human tumor cell lines, *Cancer biology & therapy*, **6**, 755-762.

Lafon-Cazal, M., *et al.* (2002) Akt mediates the anti-apoptotic effect of NMDA but not that induced by potassium depolarization in cultured cerebellar granule cells, *The European journal of neuroscience*, **16**, 575-583.

Lasserre, R., *et al.* (2008) Raft nanodomains contribute to Akt/PKB plasma membrane recruitment and activation, *Nature chemical biology*, **4**, 538-547.

Leander, R., *et al.* (2012) A mathematical model of CR3/TLR2 crosstalk in the context of Francisella tularensis infection, *PLoS computational biology*, **8**, 10.

Lee, T., *et al.* (2008) Sensing and integration of Erk and PI3K signals by Myc, *PLoS computational biology*, **4**.

Leslie, N.R. (2006) The redox regulation of PI 3-kinase-dependent signaling, *Antioxidants & redox signaling*, **8**, 1765-1774.

Leslie, N.R. and Downes, C.P. (2004) PTEN function: how normal cells control it and tumour cells lose it, *The Biochemical journal*, **382**, 1-11.

- Levenberg, K. (1944) A method for the solution of certain nonlinear problems in least squares, *Quart. Appl. Math.*, **2**, 164--168.
- Li, C., *et al.* (2010) BioModels Database: An enhanced, curated and annotated resource for published quantitative kinetic models, *BMC Systems Biology*, **4**, 92.
- Li, M. and Fukagawa, N.K. (2010) Age-related changes in redox signaling and VSMC function, *Antioxidants & redox signaling*, **12**, 641-655.
- Liao, J.K. (2008) Fine-tuning the angiogenic response to vascular endothelial growth factor, *Circulation research*, **103**, 229-230.
- Liao, Y. and Hung, M.-C. (2010) Physiological regulation of Akt activity and stability, *Am J Transl Res.*, **2**, 19-42.
- Lim, S. and Clément, M.-V. (2007) Phosphorylation of the survival kinase Akt by superoxide is dependent on an ascorbate-reversible oxidation of PTEN, *Free Radical Biology and Medicine*, **42**, 1178-1192.
- Liu, H., *et al.* (2006) Involvement of protein kinase Cepsilon in the negative regulation of Akt activation stimulated by granulocyte colony-stimulating factor, *Journal of immunology (Baltimore, Md: 1950)*. **176**, 2407-2413.
- Liu, Y., *et al.* (1998) Expression of the insulin-like growth factor I receptor C terminus as a myristylated protein leads to induction of apoptosis in tumor cells, *Cancer research*, **58**, 570-576.
- Loewenstein, W.R. (1999) *The Touchstone of Life: Molecular Information, Cell Communication, and the Foundations of Life*. Oxford University Press, USA.
- Longo, P.G., *et al.* (2007) The Akt signaling pathway determines the different proliferative capacity of chronic lymphocytic leukemia B-cells from patients with progressive and stable disease, *Leukemia*, **21**, 110-120.
- Longo, P.G., *et al.* (2008) The Akt/Mcl-1 pathway plays a prominent role in mediating antiapoptotic signals downstream of the B-cell receptor in chronic lymphocytic leukemia B cells, *Blood*, **111**, 846-855.
- Luo, L. (2011) Redox Regulation of Akt Phosphorylation in PTEN^{-/-} Mouse Embryonic Fibroblasts. *NUS Graduate School for Integrative Sciences and Engineering*. National University of Singapore.
- Luo, L., Kaur, K. and Clément, M.V. (2012) Redox control of cytosolic Akt phosphorylation in PTEN null cells, *Free radical biology & medicine*, **53**, 1697-1707.
- Macintyre, A.N., *et al.* (2011) Protein Kinase B Controls Transcriptional Programs that Direct Cytotoxic T Cell Fate but Is Dispensable for T Cell Metabolism.
- Mann, M., *et al.* (2013) The Coming Age of Complete, Accurate, and Ubiquitous Proteomes, *Molecular cell*, **49**, 583-590.
- Mann, M., *et al.* (2013) The coming age of complete, accurate, and ubiquitous proteomes, *Mol Cell*, **49**, 583-590.
- Marquardt, D. (1963) An Algorithm for Least-Squares Estimation of Nonlinear Parameters, *SIAM Journal on Applied Mathematics*, **11**, 431.

- Marquardt, D.W. (1963) An algorithm for least squares estimation of nonlinear parameters, *SIAM Journal*, **11**, 431 - 441.
- Matthews, J.A., *et al.* (2007) Glucosamine-induced increase in Akt phosphorylation corresponds to increased endoplasmic reticulum stress in astroglial cells, *Molecular and Cellular Biochemistry*, **298**, 109-123.
- McEliece, R.J., MacKay, D.J.C. and Cheng, J.-F. (1998) Turbo decoding as an instance of Pearl's "beliefpropagation" algorithm, *Selected Areas in Communications, IEEE Journal on*, 140-152.
- Meili, R., *et al.* (1999) Chemoattractant-mediated transient activation and membrane localization of Akt/PKB is required for efficient chemotaxis to cAMP in Dictyostelium, *The EMBO journal*, **18**, 2092-2105.
- Meltzer, T., Globerson, A. and Weiss, Y. (2009) Convergent message passing algorithms - a unifying view. *Conference on Uncertainty in Artificial Intelligence (UAI '09)*.
- Michalewicz, Z. (1994) *Genetic algorithms + data structures = evolution programs*. Springer-Verlag, Berlin.
- Moles, C.G., Mendes, P. and Banga, J.R. (2003) Parameter estimation in biochemical pathways: a comparison of global optimization methods, *Genome Res*, **13**, 2467-2474.
- Montero, A.J. and Jassem, J. (2011) Cellular redox pathways as a therapeutic target in the treatment of cancer, *Drugs*, **71**, 1385-1396.
- Morino, S., *et al.* (2008) Mild Electrical Stimulation with Heat Shock Ameliorates Insulin Resistance via Enhanced Insulin Signaling, *PLoS One*, **3**, e4068.
- Murata, H., *et al.* (2003) Glutaredoxin exerts an antiapoptotic effect by regulating the redox state of Akt, *The Journal of biological chemistry*, **278**, 50226-50233.
- Murayama, K., *et al.* (2007) Akt activation induces epidermal hyperplasia and proliferation of epidermal progenitors, *Oncogene*, **26**, 4882-4888.
- Murphy, K., Weiss, Y. and Jordan, M. (1999) Loopy Belief Propagation for Approximate Inference: An Empirical Study. In, *Proceedings of Uncertainty in AI*. pp. 467.
- Murphy, K., Weiss, Y. and Jordan, M. (1999) Loopy Belief Propagation for Approximate Inference: An Empirical Study. *Proceedings of Uncertainty in AI*. pp. 467.
- Murphy, L.O., *et al.* (2002) Molecular interpretation of ERK signal duration by immediate early gene products, *Nature cell biology*, **4**, 556-564.
- Nägele, T., *et al.* (2010) Mathematical modeling of the central carbohydrate metabolism in Arabidopsis reveals a substantial regulatory influence of vacuolar invertase on whole plant carbon metabolism, *Plant physiology*, **153**, 260-272.
- Nakamura, A., *et al.* (2008) Freud-1/Aki1, a novel PDK1-interacting protein, functions as a scaffold to activate the PDK1/Akt pathway in epidermal growth factor signaling, *Molecular and cellular biology*, **28**, 5996-6009.
- Nakatani, K., *et al.* (1999) Up-regulation of Akt3 in estrogen receptor-deficient breast cancers and androgen-independent prostate cancer lines, *The Journal of biological chemistry*, **274**, 21528-21532.

- Nelder, J.A. and Mead, R. (1965) A Simplex Method for Function Minimization, *The Computer Journal*, **7**, 308-313.
- Newton, A.C. (2009) Lipid activation of protein kinases, *Journal of lipid research*, S266-271.
- Nim, T.H., *et al.* (2010) Estimating Reaction Rate Parameters in Cell Signaling Pathways Using Extreme Decomposition and Belief Propagation Tailored for Data-Rich Cases, *arXiv:1103.0907v1 [q-bio.MN]*.
- Osaki, M., Oshimura, M. and Ito, H. (2004) PI3K-Akt pathway: its functions and alterations in human cancer, *Apoptosis : an international journal on programmed cell death*, **9**, 667-676.
- Palsson, B. (2011) *Systems Biology: Simulation of Dynamic Network States*. Cambridge University Press.
- Palsson, B.O. (2006) *Systems Biology: Properties of Reconstructed Networks*. Cambridge University Press.
- Pearl, J. (1988) *Probabilistic Reasoning in Intelligent Systems: Networks of Plausible Inference (2nd ed.)*. Morgan Kaufmann, San Francisco, CA.
- Pervaiz, S. and Clement, M.-V. (2007) Superoxide anion: Oncogenic reactive oxygen species?, *The International Journal of Biochemistry & Cell Biology*, **39**, 1297-1304.
- Plas, D.R. and Thompson, C.B. (2005) Akt-dependent transformation: there is more to growth than just surviving, *Oncogene*, **24**, 7435-7442.
- Pouysségur, J. and Lenormand, P. (2003) Fidelity and spatio-temporal control in MAP kinase (ERKs) signalling, *European journal of biochemistry / FEBS*, **270**, 3291-3299.
- Purvis, J.E., *et al.* (2008) A molecular signaling model of platelet phosphoinositide and calcium regulation during homeostasis and P2Y1 activation, *Blood*, **112**, 4069-4079.
- Purvis, J.E., *et al.* (2012) p53 dynamics control cell fate, *Science (New York, NY.)*, **336**, 1440-1444.
- Qiu, M.S. and Green, S.H. (1992) PC12 cell neuronal differentiation is associated with prolonged p21ras activity and consequent prolonged ERK activity, *Neuron*, **9**, 705-717.
- Quaiser, T. and Mönnigmann, M. (2009) Systematic identifiability testing for unambiguous mechanistic modeling--application to JAK-STAT, MAP kinase, and NF-kappaB signaling pathway models, *BMC Systems Biology*, **3**, 50.
- Raimondi, C. and Falasca, M. (2011) Targeting PDK1 in cancer, *Current medicinal chemistry*, **18**, 2763-2769.
- Ramsay, J.O., *et al.* (2007) Parameter estimation for differential equations a generalized smoothing approach, *Journal of the Royal Statistical Society Series B Statistical Methodology*, **69**, 741-796.
- Reed, R., *et al.* (2009) Redox-sensitive Akt and Src regulate coronary collateral growth in metabolic syndrome, *American journal of physiology Heart and circulatory physiology.*, **296**, H1811-1821.

- Reeves, E.K.M., *et al.* (2009) Proteomic profiling of glucocorticoid-exposed myogenic cells: Time series assessment of protein translocation and transcription of inactive mRNAs, *Proteome Sci.*, **7**, 26.
- Reeves, M.A. and Hoffmann, P.R. (2009) The human selenoproteome: recent insights into functions and regulation, *Cellular and molecular life sciences*, **66**, 2457-2478.
- Ren, J., *et al.* (2010) Opal web services for biomedical applications, *Nucleic acids research*, **38**, W724-W731.
- Rocher, G., *et al.* (2007) Inhibition of B56-containing protein phosphatase 2As by the early response gene IEX-1 leads to control of Akt activity, *The Journal of biological chemistry*, **282**, 5468-5477.
- Rodriguez-Fernandez, M., Mendes, P. and Banga, J.R. (2006) A hybrid approach for efficient and robust parameter estimation in biochemical pathways, *Biosystems*, **83**, 248-265.
- Rodriguez-Fernandez, M., Mendes, P. and Banga, J.R. (2006) A hybrid approach for efficient and robust parameter estimation in biochemical pathways, *Bio Systems*, **83**, 248-265.
- Runarsson, T. and Yao, X. (2000) Stochastic ranking for constrained evolutionary optimization, *EEE Transactions on Evolutionary Computation*, **4**, 284 - 294.
- Sanghera, K.P., *et al.* (2011) The PI3K/Akt/mTOR pathway mediates retinal progenitor cell survival under hypoxic and superoxide stress *Molecular and Cellular Neuroscience*, **47**, 145-153.
- Schmidt, H. and Jirstrand, M. (2006) Systems Biology Toolbox for MATLAB: a computational platform for research in systems biology, *Bioinformatics*, **22**, 514-515.
- Scott, J.D. and Pawson, T. (2009) Cell signaling in space and time: where proteins come together and when they're apart, *Science (New York, NY.)*, **326**, 1220-1224.
- Shi, Y., *et al.* (2009) Computational modeling of pathway dynamics for detecting drug effects: paradoxical effects of LYS303511 on TRAIL-induced apoptosis. pp. 213-224.
- Shih, A.J., Purvis, J. and Radhakrishnan, R. (2008) Molecular systems biology of ErbB1 signaling: bridging the gap through multiscale modeling and high-performance computing, *Molecular bioSystems*, **4**, 1151-1159.
- Song, G., Ouyang, G. and Bao, S. (2005) The activation of Akt/PKB signaling pathway and cell survival, *Journal of cellular and molecular medicine*, **9**, 59-71.
- Srinath, S. and Gunawan, R. (2010) Parameter identifiability of power-law biochemical system models, *Journal of biotechnology*, **149**, 132-140.
- Stamler, J.S. and Hess, D.T. (2010) Nascent nitrosylases, *Nature cell biology*, **12**, 1024-1026.
- Stolovitzky, G., Monroe, D. and Califano, A. (2007) Dialogue on reverse-engineering assessment and methods: the DREAM of high-throughput pathway inference, *Annals of the New York Academy of Sciences*, **1115**, 1-22.
- Suresh Babu, C.V., *et al.* (2008) Kinetic analysis of the MAPK and PI3K/Akt signaling pathways, *Molecules and cells*, **25**, 397-406.
- Tan, C.S. and Linding, R. (2009) Experimental and computational tools useful for (re)construction of dynamic kinase-substrate networks, *Proteomics*, **9**, 5233-5242.

- Tasaki, S., *et al.* (2010) Phosphoproteomics-based modeling defines the regulatory mechanism underlying aberrant EGFR signaling, *PLoS One*, **5**, e13926.
- Taylor, V., *et al.* (2000) 5' phospholipid phosphatase SHIP-2 causes protein kinase B inactivation and cell cycle arrest in glioblastoma cells, *Molecular and cellular biology*, **20**, 6860-6871.
- Tetko, I.V., Livingstone, D.J. and Luik, A.I. (1995) Neural network studies. 1. Comparison of overfitting and overtraining, *Journal of Chemical Information and Computer Sciences*, **35**, 826-833.
- Tewarson, R.P. (1980) On the use of splines for the numerical solution of nonlinear two-point boundary value problems, *BIT Numerical Mathematics*, **20**, 223-232.
- Thomaseth, K., *et al.* (1996) Integrated mathematical model to assess beta-cell activity during the oral glucose test, *The American journal of physiology*, **270**, E522-531.
- Tokunaga, E., *et al.* (2008) Deregulation of the Akt pathway in human cancer, *Current Cancer Drug Targets*, **8**, 27-36.
- Toni, T., *et al.* (2012) Elucidating the in vivo phosphorylation dynamics of the ERK MAP kinase using quantitative proteomics data and Bayesian model selection, *Molecular bioSystems*.
- Trunnell, N.B., *et al.* (2011) Ultrasensitivity in the Regulation of Cdc25C by Cdk1, *Molecular cell*, **41**, 263-274.
- Ufer, C. and Wang, C.C. (2011) The Roles of Glutathione Peroxidases during Embryo Development, *Frontiers in molecular neuroscience*, **4**, 12.
- Vazquez, F. and Devreotes, P. (2006) Regulation of PTEN function as a PIP3 gatekeeper through membrane interaction, *Cell cycle (Georgetown, Tex)*, **5**, 1523-1527.
- Venkatraman, L., *et al.* (2011) Steady states and dynamics of urokinase-mediated plasmin activation in silico and in vitro, *Biophysical journal*, **101**, 1825-1834.
- Vincent, E.E., *et al.* (2011) Akt phosphorylation on Thr308 but not on Ser473 correlates with Akt protein kinase activity in human non-small cell lung cancer, *British Journal of Cancer*, **104**, 1755-1761.
- Voit, E.O. (2000) *Computational Analysis of Biochemical Systems: A Practical Guide for Biochemists and Molecular Biologists*. Cambridge University Press.
- Wang, C.-C., Cirit, M. and Haugh, J.M. (2009) PI3K-dependent cross-talk interactions converge with Ras as quantifiable inputs integrated by Erk, *Molecular systems biology*, **5**, 246.
- Wee, K.B. and Aguda, B.D. (2006) Akt versus p53 in a Network of Oncogenes and Tumor Suppressor Genes Regulating Cell Survival and Death, *Biophysical journal*, **91**, 857-865.
- Weinberg, R.A. (2006) *The Biology of Cancer*. Garland Science.
- Wu, K.L., *et al.* (2004) The NHE1 Na⁺/H⁺ exchanger recruits ezrin/radixin/moesin proteins to regulate Akt-dependent cell survival, *The Journal of biological chemistry*, **279**, 26280-26286.
- Yaffé, M.B. (2008) Signaling networks and mathematics, *Science signaling*, **1**.
- Yang, H.W., *et al.* (2012) Cooperative Activation of PI3K by Ras and Rho Family Small GTPases, *Molecular cell*.

- Yang, W.L., *et al.* (2009) The E3 ligase TRAF6 regulates Akt ubiquitination and activation, *Science (New York, NY.)*, **325**, 1134-1138.
- Yedidia, J., Freeman, W. and Weiss, Y. (2003) Understanding belief propagation and its generalizations. In, *Exploring artificial intelligence in the new millennium*. pp. 239-269.
- Yoon, S.O., *et al.* (2002) Selenite suppresses hydrogen peroxide-induced cell apoptosis through inhibition of ASK1/JNK and activation of PI3-K/Akt pathways, *FASEB journal : official publication of the Federation of American Societies for Experimental Biology*, **16**, 111-113.
- Yuan, Z.Q., *et al.* (2000) Frequent activation of AKT2 and induction of apoptosis by inhibition of phosphoinositide-3-OH kinase/Akt pathway in human ovarian cancer, *Oncogene*, **19**, 2324-2330.
- Zhan, C. and Yeung, L.F. (2011) Parameter estimation in systems biology models using spline approximation, *BMC Systems Biology*.
- Zhang, G. and Neubert, T.A. (2009) Use of stable isotope labeling by amino acids in cell culture (SILAC) for phosphotyrosine protein identification and quantitation, *Methods in molecular biology (Clifton, NJ.)*. 79-92.
- Zhang, G.L., DeLuca, D.S. and Brusica, V. (2011) Database resources for proteomics-based analysis of cancer, *Methods in molecular biology (Clifton, NJ.)*. **723**, 349-364.
- Zhang, M. and Riedel, H. (2009) Insulin receptor kinase-independent signaling via tyrosine phosphorylation of phosphatase PHLPP1, *Journal of cellular biochemistry*, **107**, 65-75.
- Zhang, X., *et al.* (2011) Akt, FoxO and regulation of apoptosis ☆, *Biochimica et Biophysica Acta (BBA) - Molecular Cell Research*, **1813**, 1978-1986.
- Zhu, P., *et al.* (2011) Angiopoietin-like 4 protein elevates the prosurvival intracellular O₂(-):H₂O₂ ratio and confers anoikis resistance to tumors, *Cancer cell*, **19**, 401-415.
- Zi, Z., Chapnick, D.A. and Liu, X. (2012) Dynamics of TGF-β/Smad signaling, *FEBS letters*, **586**, 1921-1928.
- Zi, Z., *et al.* (2011) Quantitative analysis of transient and sustained transforming growth factor-β signaling dynamics, *Molecular systems biology*, **7**, 492.
- Zuluaga, S., *et al.* (2007) Negative regulation of Akt activity by p38alpha MAP kinase in cardiomyocytes involves membrane localization of PP2A through interaction with caveolin-1, *Cellular signalling*, **19**, 62-74.
- Zwolak, J.W., Tyson, J.J. and Watson, L.T. (2005) Globally optimised parameters for a model of mitotic control in frog egg extracts, *Syst Biol (Stevenage)*, **152**, 81-92.